Development of a Vehicle Static and Dynamic Load Estimation Method from Bridge Acceleration Response Measurement

橋梁加速度応答計測を利用した走行車両の静的および動的荷重推定法の開発

王浩祺

Haoqi Wang

Department of Civil Engineering

The University of Tokyo

A Dissertation Submitted to The University of Tokyo in Partial Fulfillment of the Requirements for the Degree of Doctor of Philosophy

2018.8

Acknowledgement

First, I would like to express my sincere gratitude to my supervisor, Prof. Nagayama, for providing advices, comments, and suggestions during the past three years, without whom this dissertation would not have been possible.

Besides my supervisor, I would like to thank the rest of my committee members, Prof. Eiichi Sasaki, Prof. Hiromichi Nagao, Prof. Atsushi Yamaguchi, and Prof. Di Su, for their kind comments during my mid-term, pre-final, and final defense. Special thanks to Prof. Di Su for his kind support during my entire study.

I am also thankful for those who helped me with my experiments, including Dr. Makoto Suzuki, Mr. Kyoichi Jinno, Mr. Sotaro Ohara from Sonas Corporation, for their supports on wireless sensors, Mr. Atsushi Kamoshida from National Instruments Japan, for providing valuable comments on time synchronization among sensors, Mr. Takatsugi Nakanishi from Tokyo Sokki Kenkyujo, for his supports on wheel-load transducer.

Next, I would like to thank my lab members, Dr. Boyu Zhao, for being a source of academic discussions, from whom many wonderful ideas were inspired, Dr. Muge Kuleli, for encouraging me to pursuit academia with her enthusiasm and attitude towards research, Dr. Jothi Saravanan, for sharing many valuable experiences in summer school, Mr. Chunbo Zhang, Mr. Junki Nakasuka, Mr. Waqas Ahmed, Mr. Sou Kato, and Mr. Sanggun Lee, for helping me conduct field measurements. Also, I sincerely appreciate the work from our lab secretary, Ms. Yoko Takahashi, for her efforts to make my academic life in

the lab go smoothly.

Finally, special thanks go to my family, for their support and understanding, not only during these three years, but throughout my life.

Abstract

Overloaded vehicles have negative impacts on bridges including pavement degradation, fatigue of bridge structural members, and in some extreme cases, the collapse of bridges. Understanding the real loading condition of bridges, e.g., vehicle gross and axle weights, axle number, dynamic load, and the lane in which the vehicle is passing, is thus important.

Traditional methods to estimate the weight of a vehicle using bridge response measurement typically measure the strain responses of the bridge induced by the passing vehicle. By minimizing the difference between the measured strain and one predicted by the bridge influence line and vehicle weight, the vehicle weight is estimated. The solution is usually obtained as a least-square solution. However, there are some drawbacks of this method: The installation of strain gauges is usually labor-intensive and time-consuming; the influence line needs to be calibrated in advance usually using a heavy truck of known-weight; while the vehicle weight is estimated, the dynamic load remains unknown.

In this study, a new method to estimate both static and dynamic vehicle load from bridge acceleration response measurement is proposed. The load estimation process is an inverse problem to identify the input load using the output response measurement; two difficulties exist in the inverse problem. The first difficulty is that the system properties, i.e., the bridge properties, are unknown. Bridge modal mass and bridge pavement roughness are representative bridge properties, which are not known in advance. Chapter 3 and Chapter 4 proposes techniques to easily estimate the modal mass and the pavement, respectively. These bridge properties are then used in the identification of vehicle static load in Chapter

5, and in the identification of dynamic load in Chapter 6. The second difficulty is that the inverse problem to be solved is a nonlinear problem due to the vehicle-bridge-interaction and the drive path uncertainty. A particle filter method, which can track both the time varying states and parameters, is employed to solve the inverse problem.

Chapter 3 explains a two-step method to estimate bridge modal mass. For this estimation, both the input which is large enough to excite bridge vibration and the output which is accurate enough to capture the bridge motion are needed. A vehicle is a convenient tool to excite the bridge while the tire force input to the bridge is difficult to measure. The tire force estimation method based on vehicle response measurement is first established by including the tire forces as augmented state variables of a Kalman filter. The force is then used together with the synchronously measured bridge acceleration responses to determine bridge modal mass. A genetic algorithm finds optimum bridge modal masses which reproduce the bridge responses well under the input force.

In Chapter 4, bridge pavement roughness is estimated from vehicle responses. To eliminate the influence of the bridge vibration on the pavement roughness estimation results, vehicle-bridge-interaction is considered. When the vehicle and bridge is considered as a coupled system, the equation of motion of the system becomes nonlinear. Therefore, the particle filter is adopted to estimate bridge pavement roughness as state variables, which serves as the only excitation source of the vehicle-bridge coupling system in the vertical direction and is used in the next chapter.

Chapter 5 gives vehicle static load estimation from bridge acceleration measurement. The

vehicle half-car model parameters, including the vehicle mass, are included in the state vector of the particle filter. The bridge pavement roughness estimated in Chapter 4 is used as the known input to the vehicle-bridge coupling system. The bridge displacement responses, which are double integration of acceleration, are used to improve the accuracy and to increase the speed of convergence. Experimental validation shows that the algorithm gives static weight estimation with the largest error of 11.9 %.

In Chapter 6, the problem of vehicle dynamic load identification is addressed. The bridge properties based on a plate model are extracted from acceleration measurement. The dynamic tire forces are included in the state vector and are evolved following a random walk model. Estimation of vehicle dynamic tire forces is given at each time step. The entire time history of the force is compared with the value from the method of Chapter 3 for the purpose of validation.

The four chapters described above constitute the bridge static and dynamic load estimation technique proposed in this study. All these chapters are verified by numerical simulation and validated by field measurement.

This doctoral thesis is based upon the studies conducted during October 2015 to July 2018 at the Bridge and Structure Laboratory, Department of Civil Engineering, The University of Tokyo, Japan.

Tokyo, August 2018

Wang Haoqi

Table of Contents

List of Figures

List of Tables

Chapter 1 - Introduction

1.1 Research Background

It is a common knowledge among researchers, engineers, city managers, and urban planners that overweight vehicles passing over a bridge will shorten the working life of the bridge (Fujino and Siringorino, 2011; Zhu and Law, 2016). The bridges, as a part of the crucial transportation infrastructure, are not designed to serve those vehicles that give larger load effects than the bridges can suffer. The bridge overloading effect has become a common and worldwide problem (Fu and Hag-Elsafi, 2000). It is well-known that overweight vehicles bring many harms to bridges. The most direct one is the degradation of the bridge pavement. From the structure point of view, the traffic-induced bridge deformation may cause fatigue problems, if the response is large and/or if the fatigue design is not appropriately performed (Biezma and Schanack, 2007; Wardhana and Hadipriono, 2003). Moreover, in some extreme cases, the overload vehicles may even lead to the collapse of the bridge. On the other hand, overloaded vehicles have a higher risk for traffic accidents (Jacob and Beaumelle, 2010). These concerns strengthen the necessity for monitoring the vehicle load condition of the bridge structures. The monitoring system helps to evaluate the real load on existing bridges, providing information for future designs (Yang et al, 2004). Also, the information of passing vehicles' load enables the transportation network to take corresponding actions (Cebon, 1988).

The most accurate way to obtain the vehicles' weight is the static weighing technique. In

a real case, static weighing is not convenient because the vehicles need to stop for the test, which is both cost- and time-consuming. Another technique, known as weigh-in-motion (WIM), uses load cells installed under the pavement (Richardson et al, 2014). The vehicle weight is weighed during the passage of the vehicle on the load cell. However, drawbacks of this method are obvious. The load-cell is usually directly exposed to the environment, making it less durable. The installation and the renewal process require to stop the traffic. Moreover, the estimated weight by load cells is less accurate, because the time for the passage over the load cell is usually short, which is not sufficient to average out the dynamic component of the tire force, making the result larger or smaller than the real load, depending on the recorded period of the tire force cycle.

To overcome the drawbacks of static weighing and load cell-based WIM, bridge weigh-in-motion (BWIM) was proposed (Moses, 1979). The BWIM technique uses the bridge responses to inversely deduce the vehicle load. When a vehicle passes across a bridge, bridge vibration occurs as a function of the load generated by the vehicle. This vehicle-induced bridge vibration is highly correlated with the vehicle weight, vehicle mechanical properties, driving speed, bridge pavement condition, and bridge dynamic properties. Therefore, the vehicle information will be reflected in the bridge vibration, making it theoretically possible for the estimation of vehicle load from the measured bridge responses.

However, the determination of vehicle load in motion from bridge responses is not usually easy because the load created by a passing vehicle depends on both time and space. Even when a bridge is well equipped with sensors, the dynamic response of the structure is only

obtained at a limited number of points. Therefore, the problem of obtaining vehicle load information from bridge response data presents an important and challenging issue for researchers.

This thesis studies two aspects of the vehicle load, including (a) vehicle static weight, a constant value which leads to pseudo-dynamic bridge responses during vehicle passage, and (b) vehicle dynamic load caused by bridge pavement roughness and vehicle mechanical properties. Some of the bridge properties, e.g., bridge modal mass and bridge pavement roughness, need to be known in advance. Reasons of choosing these two bridge properties are that the modal mass provides a link of excitation on the bridge and the bridge responses (Brownjohn et al, 2016), while the bridge pavement roughness acts as the only excitation source to the passing vehicles in the vertical direction (Law and Zhu, 2011). In the following sections, previous research on bridge static weight estimation, moving dynamic load identification, bridge modal mass estimation, and bridge pavement roughness estimation is reviewed.

1.2 Literature Review: Bridge Static Weigh-in-Motion

Traditional BWIM techniques are based on the proposal of static algorithm of Moses (Moses, 1979). In Moses' method, the vehicle static load is related with the bridge strain induced by the passing vehicle. A strain gauge is used at the mid-span of the bridge for most cases. The measured strain is compared with the calculated strain, which is obtained from multiplying the bridge influence-line by the vehicle weight. The vehicle weight, which minimizes this difference, is chosen as the estimated value.

Many commercial BWIM systems were established following the framework of Moses' method (Yu et al, 2016). The AXWAY system (Peters, 1984) and the CULWAY system (Peters, 1986) were developed in Australia. Later, the COST 323 (COST, 2002) and the WAVE project (O'Brien et al, 2001) were proposed in Europe, leading to an improved accuracy of the BWIM system. Based on these efforts to improve the accuracy, the well-known SiWIM system was developed (Znidaric, 2011).

However, there are some drawbacks when the Moses' method is applied. The first one is that the accuracy is affected by the dynamic effects of the vehicle load, because dynamic effects lead to the deviation of the measured strain from the influence-line based calculation, causing inaccuracy. Due to this drawback, the Moses' method can obtain satisfactory results only when the bridge pavement is in a good condition (Yu et al, 2016). Also, the influence line method is reported to have lower accuracy when the transverse position of the vehicle (i.e., the vehicle's passing lane) is not known (Dempsey et al, 1998). This drawback can be partially solved by extending the idea of influence-line to the influence-surface (Quilligan, 2003). Another drawback is that the calibration of the relation between the vehicle's weight and bridge strain in advance is needed by using a known-weight vehicle (Zhao et al, 2015). The error in the calibrated influence line will proportionally affect the estimated vehicle weight. Sekiya (2016) also adopted the idea of influence-line but the method is based on the bridge acceleration data, which is then integrated to bridge displacements. However, in the influence-line based BWIM methods, the calibration process or some assumptions need to be adopted.

The influence line method proposed by Moses treats the passing vehicle as one moving

constant load (or one group of constant loads depending on the necessity of distinguishing axles). On the other hand, some researchers adopt the optimization technique to estimate the vehicle weight or even all the vehicle parameters from the bridge responses. Genetic algorithm (Jiang et al, 2004; Au et al, 2004; Deng and Cai, 2009), response sensitivity method (Law et al, 2006), firefly algorithm (Pan et al, 2014), artificial neural network (Kim et al, 2009), and particle filter (Lalthlamuana, 2015) are used by researchers to give estimation on the vehicle parameters including vehicle weight.

The influence-line method and the parameter identification method are the most frequently adopted techniques. Moreover, researchers also proposed other methods for the purpose of BWIM. Ojio and Yamada (2002) calculated the vehicle weight based on the idea of the influence-area, in which the area under the responses curve equals to the product of the vehicle weight and the area under the influence-line. The same researchers also proposed a reaction force method, where reaction force measured at the bridge girder-end stiffener is used to give the axle weights (Ojio and Yamada, 2005).

1.3 Literature Review: Moving Dynamic Load Identification

The force from the passing vehicle to the bridge can be divided into two aspects: moving static load and moving dynamic load. The moving static load is caused by the static weight of the vehicle. This type of load leads to bridge pseudo-dynamic response because of the spatial difference of mode shapes of the bridge. On the other hand, due to the random pavement roughness of the bridge and the mechanical system of the vehicle, the tire forces on the bridge is also time-variant; the tire force is moving dynamic load. The time-dependent property of the vehicle force on the bridge is also important. The

5

identification of this moving dynamic load has attracted many researchers to propose different methods, which are briefly reviewed herein.

Law et al proposed the first time-domain method for the moving load identification problem (Law et al, 1997), where the moving axle load as well as the bridge modal responses are included in a convolution integral. The bridge moment and acceleration induced by the passing vehicle are then used to identify the time history of moving dynamic load by a least-square method. This method was then applied for a multi-span continuous bridge (Zhu and Law, 2001).

Chan et al. (1999) proposed an interpretive method to identify the time history of a single force moving on top of a beam. The bridge responses are transformed into modal coordinates. The axle load at each time step is also identified by least-square method. This paper defines an index showing the ratio between the vehicle wheelbase and bridge length, known as ASR (Axle-spacing-to-span ratio), and found that the axle force can be estimated with more accuracy if ASR is larger. This method is shown to be suitable for a beam with non-uniform cross section (Zhu and Law, 1999).

The least-square method is also conducted in the frequency domain for the spectrum of moving dynamic force, followed by an inverse Fourier transform to give time history (Law et al, 1999). This method is further improved by using regularization and SVD technique (Yu and Chan, 2003). The frequency-domain method is found to be more computationally efficient while the accuracy is reduced when compared with time-domain method.

State space methods are also widely adopted by researchers. The force identification is performed with regularization after obtaining the system differential equations in the state space (Zhu et al, 2006). An adaptive algorithm based on the Kalman filter with a recursive least-square estimator to identify the moving forces in state space is proposed by Chen and Lee (2008) and Chen et al. (2012).

The methods reviewed above try to identify the force value at each time step from the bridge responses. There are some other methods that model the force by base-functions, such as the orthogonal Legendre or the Fourier series. Instead of identifying the force at each time step, these methods identify the coefficients of the corresponding base-functions. Chan (2008) and Yu et al. (2008) developed this method in their corresponding research.

The above review introduces the methods that use the analytical model of the bridge, where the equation of motion of the bridge-vehicle system is decoupled following the modal superposition technique. The moving dynamic loads are identified by different optimization methods. On the other hand, the bridge structure can also be modelled by discretizing the bridge deck into finite element or lumped mass system. In this type of method, a location matrix is needed to transform the forces on the bridge into nodal forces. The optimization methods reviewed above (e.g., time and frequency domain methods, state space methods) can be adopted in a similar manner (Ouyang, 2011; Law and Fang, 2001; Las Nordstroom, 2006; Gonzalez et al, 2008; Law et al, 2004; Wu and Shi, 2006).

1.4 Literature Review: Bridge Modal Mass Identification

As reviewed in the previous sections, most BWIM methods and moving load identification methods require the bridge properties to be known. While the bridge natural frequencies, damping ratios, mode shapes, and bridge size may be easily obtained through existing structural health monitoring techniques, the bridge model mass, which requires the simultaneous measurement of bridge excitation and bridge responses, remains challenging. In this section, the existing techniques for bridge modal mass identification are reviewed, followed by the review of vehicle tire force estimation. The tire force is used as the bridge excitation in the method of bridge modal mass identification used in this study.

1.4.1 Traditional Techniques for Bridge Modal Mass Identification

Theoretically speaking, without knowing the excitation force and the corresponding bridge responses, it is not possible to extract the modal mass value (Brownjohn and Pavic, 2007). While the bridge responses can be easily measured by various types of sensors or accelerometers, the measurement of the controllable excitation on the bridge is still not easy. Instrumented hammer (Reynders et al, 2007), drop-weight (Reynders et al, 2007), and electronic shaker (Brownjohn et al, 2016) are the most frequently used excitation source, although with many apparent limitations. The instrumented hammer gives an impulse input, which cannot easily provide sufficient energy to excite all of the necessary vibration modes of a large structure. Also, there is a risk of locally damaging the structure at the impact point. The drop-weight may solve the problem of the instrumented hammer but is heavy, thus not portable for convenient use. The electronic shaker can provide

desirable excitation with reasonable amplitude and frequency, but electrical supplies are needed on site, which limits its practical applications. Furthermore, all of these three methods require closure of the bridge.

<div align="center">(a) Instrumented hammer   (b) Drop-weight</div>

<div align="center">Fig. 1-1. Instrumented hammer and drop-weight for modal mass identification</div>

<div align="center">(Reynders et al, 2007)</div>

On the other hand, the vehicle-induced load has long been widely acknowledged as a desirable source of excitation on the bridge for its wide load frequency range, the convenience in practice, and sufficient impact energy. Therefore, in recent decades, many researchers focus on the possibility of using a sensor-instrumented vehicle as both exciter and receiver of the bridge vibration, usually known as drive-by monitoring, for the purpose of bridge dynamic property extractions (Lin and Yang, 2005; Gomez et al, 2011; Yang and Chang, 2009a; Yang and Chang, 2009b; Nagayama et al, 2017) and bridge damage detection (Bu et al, 2006; McGetrick et al, 2009; Nguyen and Tran, 2010; Xiang

et al, 2010; Yin and Tang, 2011). One difficulty that may hinder the development of drive-by monitoring is that the vehicle-induced dynamic load, dependent on the vehicle-bridge interaction, is usually not easy to measure. In the next section, a review for possible methods for vehicle tire force estimation from vehicle responses is given.

1.4.2 Vehicle Dynamic Tire Force Identification from Vehicle Responses

In recent decades, many efforts have been made for the tire force identification problem. In the research field of vehicle dynamic system, the vehicle tire forces in all the three directions, i.e., longitudinal, lateral, and vertical, are investigated. However, for the purpose of bridge monitoring using a moving sensory system, the vertical tire forces on the bridge are of interests. Therefore, only research on the vertical tire force estimation is reviewed herein, which can be roughly categorized to two types of methods: from measurement on the vehicle body responses or on the vehicle tire responses.

To estimate tire force from vehicle responses, a good knowledge about vehicle models and vehicle dynamics is necessary. Shim and Ghike (2007) studied a 14-degree-of-freedom vehicle model for vertical tire force estimation and discussed its limitations. Dakhlallah et al. (2008) used an extended Kalman filter on a four-wheel vehicle model. Longitudinal and lateral acceleration, driving speed, and rotational velocity of each tire are needed. A roll plane vehicle model is used by Doumiati et al (2010) to propose a two-step method to estimate vertical tire forces by measuring vehicle accelerations, angular velocity, and the relative deflections of the suspension system. This method was extended

to deal with the case of inclined road and uneven road roughness (Jiang et al, 2014). Hamann et al. (2014) used the unscented Kalman filter to estimate vertical tire forces, which requires angular wheel velocity measurement apart from vehicle accelerations and speed. Cordeiro et al. (2016) used a four-wheel vehicle model and a cascade observer in the extended Kalman filter to eliminate the use of a random walk model describing the tire force. However, a laser distance sensor needs to be used to measure the deflection of the suspension system.

Some vehicle models adopted by these researchers are shown in Fig. 1-2. Most of these models are quite complicated. For the purpose of vehicle control and vehicle safety, complicated vehicle models are necessary. However, more complex vehicle model means that more observation is needed for the tire force estimation, while the sensors for some of the observations, such as rotational velocity of each tire and relative deflection of the suspension system, are either too expensive or difficult to install; complex models are therefore not practical for ordinary commercial vehicles.
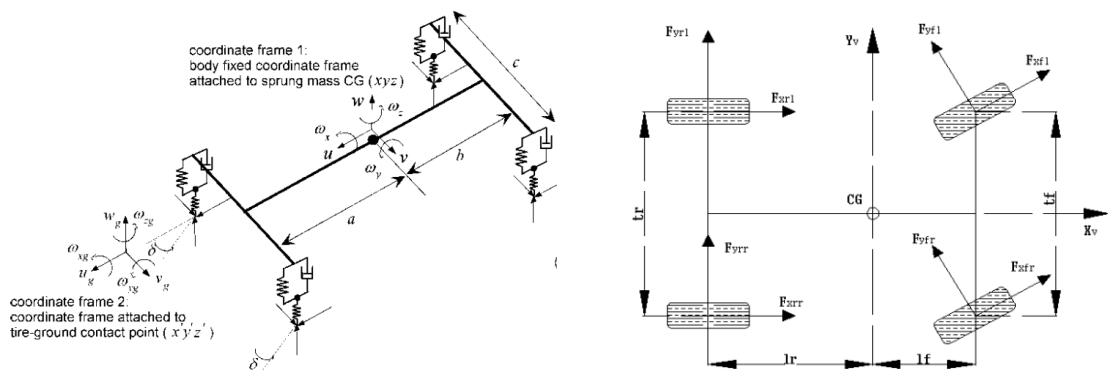
(a) 14-DOF model (Shim and Ghike, 2007) (b) Four-wheel model (Dakhlallah et al, 2008)
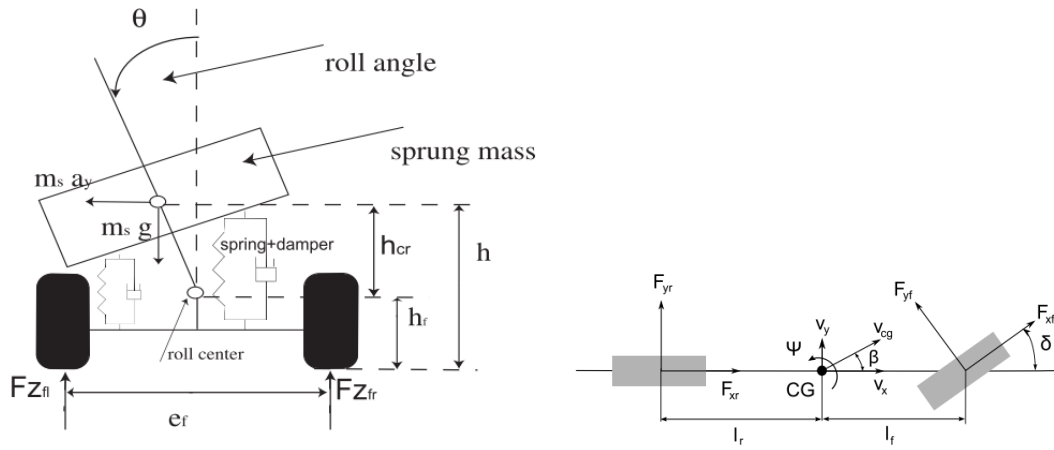
(c) Roll plane model (Doumiati et al, 2010)   (d) Bicycle model (Hamann et al, 2014)

Fig. 1-2. Various vehicle models

There are some other researchers who tried to estimate tire forces from the measurement on the vehicle tires. Accelerometers (Braghin et al, 2006), optical sensors (Tuononen, 2009), and strain gauges (Cheli et al, 2011) are installed directly on the vehicle tires. However, only one force value can be obtained in one rotational cycle of the tire due to the eccentric installation position of the sensors, leading to a very low sampling rate of tire forces. Chen et al. (2018) developed the relation between the vertical tire force and the dynamic tire pressure from the ideal gas law and obtained the vertical tire force from the change of tire pressure after a calibration process (Chen et al, 2018). However, this method is not yet validated by real test, where the air temperature and the driving speed may affect the estimation results.

Based on the review of existing research on tire force estimation, most methods suffer from one or more of the following drawbacks: difficult sensor installation, low accuracy on rough pavement, and low sampling frequency. A method without these drawbacks for

the bridge monitoring purpose is needed.

1.5 Literature Review: Bridge Pavement Roughness Estimation

Besides bridge modal mass discussed in Section 1.4, the bridge pavement roughness is another important factor of the vehicle-bridge coupling system, because the roughness is the only excitation source in the vertical direction of the vehicle passing across the bridge. It is reasonable to say that the vehicle vibration and the bridge vibration are both caused by the uneven pavement roughness input. Therefore, in some situation, the bridge pavement roughness information needs to be obtained, not only for pavement maintenance, but also for the purpose of the prediction of vehicle and bridge vibration, which is deeply related with BWIM and moving dynamic force identification.

For practical pavement condition assessment, there are three types of methods, including manual measurement, test vehicle with laser equipment, and vehicle response-based methods. There three categories are briefly reviewed in this section.

1.5.1 Manual Pavement Measurement

In the manual measurement of pavement roughness, the most frequently used devices include the rod and level system and the total station. For the rod and level measurements, the relative pavement height compared with the height of the instrument is read from the rod. The relative pavement height of all points along the measuring route is obtained in this manner. The total station shares the same principle as the rod and level system while utilizing electronic device to obtain data. Lalthlamuana (2015) used the total station

method to give pavement roughness information, which served as the input of the vehicle-bridge coupling system.

Although the manual pavement measurement is a simple way to give pavement roughness data with a satisfactory accuracy, this method requires heavy labor work to obtain satisfactory sampling rate. Moreover, it is not possible to use this method for bridges with large traffic because the bridge needs to be closed for this measurement.

Fig. 1-3. Measurement using a total station (Lalthlamuana, 2015)

1.5.2 Inertial Laser Profiler

The inertial laser profiler serves as an accurate method for pavement roughness estimation, which consists of accelerometer, non-contact laser transducer, and a distance recorder, as shown in Fig. 1-4.

In the inertial laser profiler, the relative displacement between the ground and the inertial reference is provided by the non-contact laser. The movement of the inertial reference is compensated by the accelerometer. The profiler provides a convenient tool for pavement

roughness estimation at a high speed without influencing other activities; the profiler is thus beneficial for highway condition evaluation.

However, the inertial profiler system is usually costly and requires professional trainings of the operator. The work for post-processing is also time consuming. Most importantly, when this system is used for the pavement roughness estimation on a bridge, the moving profiler itself will lead to bridge vibration, which cannot be compensated by the simple measurement acceleration on the inertial reference.

Fig. 1-4. Inertial laser profiler (Nichireki Corporation)

1.5.3 Response-base road evaluation

Attracted by the low cost and the high efficiency, many researchers developed some

response-based method, in which an ordinary vehicle is used as the receiver of the vibration induced from pavement roughness. Most of these methods give estimation on the power-spectral-density (PSD) or international roughness index (IRI) of the road (Zhao and Nagayama, 2017). Although PSD and IRI can be good pavement condition evaluation index, they cannot predict the vibration of the vehicle-bridge coupling system. The time history of the roughness input is needed.

Among other methods that directly obtain the pavement roughness history, iDRIMS (Makihata et al, 2016; Zhao et al, 2015b) has a good performance due to its low cost, high accuracy, and easy-to-use convenience. In this method, half-car vehicle model parameters of a test vehicle are first calibrated by a hump test using a genetic algorithm. Augmented Kalman filter is then adopted to estimate the pavement roughness in the time domain. Vehicle driving speed information is used to transfer the input in the time domain to the spatial domain. The method is tested to have good accuracy and robustness against different types of noises as well as the vehicle modelling error.

However, similar to the inertial laser profiler, one drawback of the iDRIMS is that it is not suitable for pavement roughness estimation on a bridge, because it cannot consider the influence from the bridge vibration induced by the vehicle. Therefore, a method that can take the bridge deflection into consideration and eliminate the influence from the bridge vibration needs to be developed.

1.6 Inverse Analysis Techniques

As reviewed from Section 1.2 to Section 1.5, these problems are known as the inverse

problem. Some of them are in the field of parameter identification (Section 1.2 and 1.4) while others are categorized as state tracking problem (Section 1.3 and Section 1.5). To deal with such problems, the proper inverse techniques are essential. In this study, three types of inverse techniques, namely Kalman filter, particle filter, and genetic algorithm, are adopted. The Kalman filter and the genetic algorithm are used in bridge modal mass identification in Chapter 3 while the particle filter is used in Chapter 4, Chapter 5, and Chapter 6 for bridge pavement estimation, vehicle static load identification, and moving dynamic load identification, respectively. These three inverse techniques are briefly reviewed in this section.

The reasons of adopting these three techniques are discussed based their corresponding target. For the tire force estimation problem discussed in the first part of Chapter 3, both the system equation and the observation equation are linear. In this case, the linear Kalman filter is a suitable and convenience tool to trace the unknown input, and is thus adopted. In the second part of Chapter 3, the problem is to estimate the bridge modal mass, which is a typical parameter identification problem. As a traditional method, the genetic algorithm has the advantages of simple implementation and the capacity to avoid local optimization. For Chapter 4, a framework of vehicle-bridge coupling system is established to estimate bridge pavement roughness. When the vehicle-bridge interaction is considered, the equation of motion of the system also becomes coupled, making it difficult to write the system matrix. Therefore, particle filter is adopted, in which the system matrix does not need to be explicitly expressed but represented by a large number of particles in a Monte Carlo way. In the vehicle parameter identification problem in Chapter 5, the system transition function is non-linear while the observation function is

linear, which is most suitable for the implementation of the ensemble Kalman filter. However, due to the same reason as Chapter 4, the observation equation becomes also non-linear, which makes the ensemble Kalman filter unfeasible. Therefore, the particle filter is again adopted. In Chapter 6, the target is to estimate a fixed parameter and to trace the unknown input simultaneously, where particle filter is again used for its capacity of dealing with nonlinearity.

1.6.1 Kalman Filter

Kalman filter is a common method for real-time state tracing problems, in which the governing equations of the system are written in state-space form to describe the time evolution of the system state (Kalman, 1960). The general form of the system equation in the state-space is described as:

$$\mathbf{X}_{k+1} = \mathbf{A}_d \mathbf{X}_k + \mathbf{w}_k \qquad (1\text{-}1)$$

where $\mathbf{X}_k$ is the system state vector at time step k, $\mathbf{A}_d$ is the system transition matrix that linearly describes the relation between the system state at time step k and $k+1$, and $\mathbf{w}_k$ is the system error term following a zero-mean Gaussian distribution.

In the time evolution process, measurements on some state quantities are made at each time step, formulating the observation vector. The observation vector is linked with the system state vector through the observation equation, as:

$$\mathbf{Y}_k = \mathbf{C}_d \mathbf{X}_k + \mathbf{v}_k \qquad (1\text{-}2)$$

where $\mathbf{Y}_k$ is the observation vector at time step k, $\mathbf{C}_d$ is the observation matrix, and $\mathbf{v}_k$ is the observation error term following a zero-mean Gaussian distribution independent of

18

the system error term $\mathbf{w}_k$.

With the system and the observation matrices defined for each specific problem, the Kalman filter is processed through a two-step procedure, known as prediction and update, corresponding to Eqs. (1-3) – (1-4) and Eqs. (1-5) – (1.7), respectively.

$$\mathbf{X}_{k+1}^{-} = \mathbf{A}_d \hat{\mathbf{X}}_k \qquad (1\text{-}3)$$

$$\mathbf{P}_{k+1}^{-} = \mathbf{A}_d \hat{\mathbf{P}}_k \mathbf{A}_d^{\mathrm{T}} + \mathbf{Q}_k \qquad (1\text{-}4)$$

$$\mathbf{G}_{k+1} = \mathbf{P}_{k+1}^{-} \mathbf{C}_d^{\mathrm{T}} \left[\mathbf{C}_d \mathbf{P}_{k+1}^{-} \mathbf{C}_d^{\mathrm{T}} + \mathbf{R}_{k+1} \right]^{-1} \qquad (1\text{-}5)$$

$$\hat{\mathbf{X}}_{k+1} = \mathbf{X}_{k+1}^{-} + \mathbf{G}_{k+1} \left(\mathbf{Y}_{k+1} - \mathbf{C}_d \mathbf{X}_{k+1}^{-} \right) \qquad (1\text{-}6)$$

$$\hat{\mathbf{P}}_{k+1} = \left(\mathbf{I} - \mathbf{G}_{k+1} \mathbf{C}_d \right) \mathbf{P}_{k+1}^{-} \qquad (1\text{-}7)$$

where $\mathbf{Q}$, $\mathbf{R}$ are the system error matrix and observation error matrix, related with $\mathbf{w}$ and $\mathbf{v}$, respectively, $\mathbf{P}$ is the error covariance matrix, $\mathbf{G}$ is known as Kalman gain matrix, and superscript '‑' indicates that the value is the priori estimation, and a '^' stands for the posteriori estimation.

The above process is iterated for each time step and terminates at the end of the signal, giving the estimation of the entire system state. The implementation of the Kalman filter to the vertical tire force estimation is discussed in Chapter 3.

1.6.2 Particle Filter

In the particle filter method, the state of the system is estimated by introducing measured data step by step to the dynamic equation (Gordon et al, 1993). A state-space form of the

system dynamic equation is needed for estimating the state, as expressed in

$$\mathbf{X}_{k+1} = f_k\left(\mathbf{X}_k\right) + \mathbf{w}_k \qquad (1\text{-}8)$$

where $\mathbf{X}_k$ is the state vector representing the state of the system at each time step k. f_k represents the state transition function of the system, and $\mathbf{w}_k$ is the system error with a known distribution.

The observation vector $\mathbf{Y}_k$ is formed by measurements made at each time step and is related to the state vector through the following observation equation

$$\mathbf{Y}_k = h_k\left(\mathbf{X}_k\right) + \mathbf{v}_k \qquad (1\text{-}9)$$

where $\mathbf{v}_k$ is the observation error with known distribution and independent with the system $\mathbf{w}_k$. h_k is the transition function from system state vector to observation vector.

The main process of particle filter method is to construct the posterior probability density function of the state vector through Bayesian state estimation (Arulampalam et al, 2002; Carpenter et al, 1999). The prediction and update steps are shown in Eq. (1-10) and Eq. (1-11), respectively.

$$p\left(\mathbf{X}_k \mid \mathbf{Y}_{1:k-1}\right) = \int p\left(\mathbf{X}_k \mid \mathbf{X}_{k-1}\right) p\left(\mathbf{X}_{k-1} \mid \mathbf{Y}_{1:k-1}\right) \mathrm{d}\mathbf{X}_{k-1} \qquad (1\text{-}10)$$

$$p\left(\mathbf{X}_k \mid \mathbf{Y}_{1:k}\right) = \frac{p\left(\mathbf{Y}_k \mid \mathbf{X}_k\right) p\left(\mathbf{X}_k \mid \mathbf{Y}_{1:k-1}\right)}{p\left(\mathbf{Y}_k \mid \mathbf{Y}_{1:k-1}\right)} \qquad (1\text{-}11)$$

Eqs. (1-10) and (1-11) show the procedure to obtain the posterior PDF of time step k. The posterior PDF of time step k-1, $p(\mathbf{X}_{k-1}|\mathbf{Y}_{1:k-1})$, with the measurement data up to time k-1, is passed through the system equation to obtain the prior PDF of time step k expressed as $p(\mathbf{X}_k|\mathbf{Y}_{1:k-1})$. Measurement data at time step k is then introduced to calculate the posterior

PDF of time step k, $p(\mathbf{X}_k|\mathbf{Y}_{1:k})$, based on the Bayesian formula.

After a number of iteration steps, the system state will converge to the real value. If the transition function f_k and h_k are linear, and the Gaussian distribution assumption applies to both the prior and posterior PDF, only the mean value and the covariance of the state need to be estimated at each step. This method becomes the same as Kalman filter. However, when the parameter identification problem is considered, the transition function f_k is always nonlinear against unknown parameters. Therefore, the assumption of the Kalman filter cannot be applied here. Alternatives to the Kalman filter include the extended Kalman filter (EKF), the unscented Kalman filter (UKF), and the particle filter (PF), each of which has its own assumptions.

The prior and posterior PDF of the state is represented by a large number of particles. When the number of particles becomes large enough, they can equivalently represent the exact PDF in a Monte Carlo way. The Gaussian assumption in EKF and UKF becomes unnecessary because the particles can represent any form of PDF. At each time step k, each particle is passed through the system equation to form a prior PDF. The likelihood of each particle is normalized through Eq. (1-12), in a process called resampling, where q_i is the normalized likelihood for the ith particle, and N is the number of particles. A new series of particles is generated based on the normalized likelihood and the iteration process continues to the next step until the system state converges to its real value.

$$q_i = \frac{p\left(\mathbf{Y}_k | \mathbf{X}_k(i)\right)}{\sum_{i=1}^{N} p\left(\mathbf{Y}_k | \mathbf{X}_k(i)\right)} \tag{1-12}$$

Note that in the particle filtering process, one phenomenon known as particle

degeneration may occur, which will significantly decrease the particle diversity. After some iteration steps, all the particles will have only a few values, leading to the convergence to a wrong value before getting close to the real one. To deal with such phenomenon, one simple way is to significantly increase the initial number of particles. However, the computational cost will thus be increased to an unacceptable level due to the large number of particles.

On the other hand, to save the particle diversity, a technique is developed by Nakano (2007), where each of the total N particles is updated after the resampling process by replacing the value of this particle as the weighted summation of l other particles. This process is described as

$$x^{(i)} = \sum_{j=1}^{l} \gamma_j x^{(j)} \tag{1-13}$$

To make the newly updated particle values consistent with other particles, the criteria of choosing the weight γ_j is

$$\sum_{j=1}^{l} \gamma_j = 1, \ \sum_{j=1}^{l} \gamma_j^2 = 1 \tag{1-14}$$

The particle filtering technique is used in Chapter 4, Chapter 5, and Chapter 6 for the corresponding problem, i.e., bridge pavement roughness estimation, vehicle parameter identification, and moving dynamic load identification problem.

1.6.3 Genetic Algorithm

The genetic algorithm is a traditional and common inverse technique, which is widely used in the parameter identification problem when both the input and the output of the system are known. This method is characterized by some terms in biology, including

evaluation, selection, crossover, and mutation (Davis, 1991). The parameter value is expressed in binary code with many zeros and ones known as 'genes'. Different combinations of parameters give different individual, each of which consists of a series of parameter values expressed in binary code.

A target function is first determined according to the specific problem. In the parameter identification problem in structural dynamics, the target function is usually expressed as to minimize the difference between the predicted system responses and the measured responses. A fitness value is defined for each individual based on its performance in the target function. Those individuals with higher fitness will have higher chances to survive and to give offspring. The chance for each individual of being selected to give offspring is estimated by Eq. (1-15), where the probability to be chosen is defined as proportional to their fitness values.

$$p_i = \frac{g(x_i)}{\sum_{j=1}^{N} g(x_j)} \tag{1-15}$$

Crossover is defined as the process of two parent individuals giving offspring individuals. In this process, some genes in one parent will be replaced by the corresponding genes of the other parent.

In the individual evolving process, mutation is introduced as an arbitrary modification that changes a gene of 'zero' to 'one' or from 'one' to 'zero'. This process aims to prevent premature convergence.

The genetic algorithm will terminate when it gives reasonable target function that is

defined in advance, or when a preset number of generations is met. The flow chart of the genetic algorithm is shown in Fig. 1-5. In this study, the genetic algorithm is used in the second part of Chapter 3, where the bridge modal mass values are identified through estimated vehicle dynamic load input and measured bridge acceleration response output.
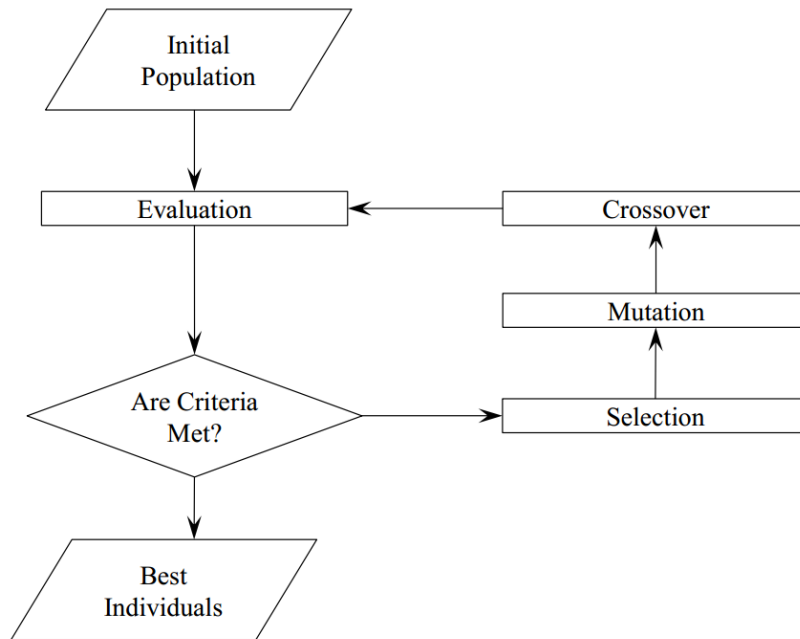
Fig. 1-5. Flowchart of genetic algorithm

1.7 Organization of Thesis

The thesis is organized as follows.

Chapter 1 introduces the background of this research and a detailed literature review for each of the main contents in this thesis, i.e., vehicle tire force estimation from vehicle responses, bridge modal mass identification, pavement roughness estimation, vehicle static load and moving dynamic load identification from bridge responses. The introduction of the inverse analysis technique used in this study is also given, including

Kalman filter, particle filter, and genetic algorithm.

Chapter 2 gives some description in vehicle-bridge dynamics. The rigid body motion models of half-car and full-car models are introduced. Basic equations of motion of bridge beam and slab models are shown with modal analysis techniques. The methods to consider vehicle-bridge coupling interaction is also reviewed.

Chapter 3 develops a two-step method to identify bridge modal mass. The first step is to estimate vehicle dynamic tire forces by an augmented Kalman filter from simple measurement of vehicle responses. The estimated forces are used in the second step where bridge acceleration is simultaneously measured. The bridge modal mass values are then optimized by genetic algorithm.

Chapter 4 estimates the bridge pavement roughness from vehicle responses through particle filter. The nonlinearity induced by vehicle-bridge coupling effect is compensated by considering vehicle-bridge interaction using the iteration method in particle filter.

Chapter 5 develops a method to identify parameters of the passing vehicle from the vehicle-induced responses by using particle filter. The bridge modal mass value estimated in Chapter 3 and the bridge pavement roughness estimated in Chapter 4 can be used in this algorithm.

Chapter 6 gives the algorithm to directly estimate the passing vehicle's dynamic load from bridge acceleration responses by particle filter. A parameter representing the passing

route of the vehicle is included in the state vector to consider lane detection.

Chapter 7 summarizes the conclusions of this study and possible future work.

Appendix A shows the performance of the wireless sensors used in the bridge acceleration measurement in this study. Static test as well as shake-table test is described to show the behavior of the wireless sensors in the frequency range of interests.

Appendix B develops a bridge fundamental frequency estimation method based on the contents of Chapter 4. While the vehicle-bridge interaction needs to be included in Chapter 4 to give estimation on the bridge pavement roughness, this interaction is ignored in this appendix, making the bridge vibration reflected in the estimated pavement excitation. The bridge fundamental frequency is thus estimated by subtracting the common part, i.e., pavement roughness excitation, in the front and rear estimation.

Chapter 2 Vehicle-Bridge Dynamics and Bridge Modal Analysis of Two Bridges

2.1 Vehicle Model

As mentioned in Chapter 1, there exist many vehicle models in the field of vehicle dynamics. Each model has its own features and suitable applications. Usually, models with large degrees of freedom can represent complicated motions while such models require measurement of many physical quantities and identification of many parameters, which is practically difficult; such models with insufficient measurement or poorly estimated parameters may lead to inaccuracy or even total failure of the estimation. Therefore, the choice of an adequate vehicle model meeting the objective is crucial.

2.1.1 Half-car Model

A typical half-car model is shown in Fig. 2-1, whose vehicle parameters include vehicle body mass m_b, moment of inertia I_y, tire mass m_f and m_r, vehicle suspension stiffness k_f and k_r, tire stiffness k_{tf} and k_{tr}, and suspension damping c_f and c_r (Jazar, 2017). The road roughness at the point under the front and rear tire are represented by h_f and h_r. L_f and L_r are the distance from the vehicle's center of gravity (COG) to the suspension systems. The subscripts f and r indicate the front and rear part of the vehicle, respectively.
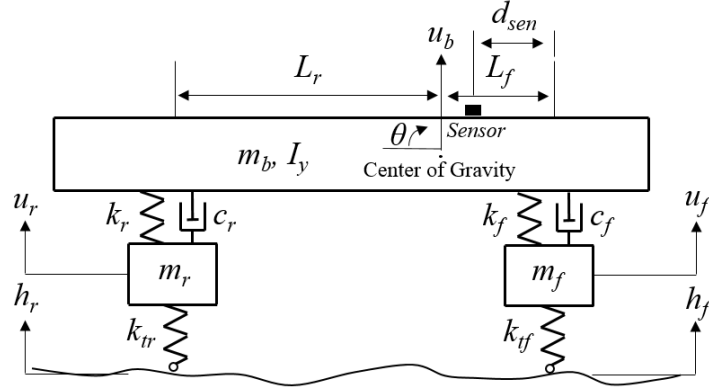
Fig. 2-1. Half-car model

The half-car model has 4 degrees-of-freedom, including vehicle body vertical movement u_b, vehicle body pitching motion θ_b, and front and rear tire vertical movement u_f and u_r. The equation of motion of the half-car model is:

$$m_b\ddot{u} + c_f\left(\dot{u} - \dot{u}_f - L_f\dot{\theta}\right) + c_r\left(\dot{u} - \dot{u}_r + L_r\dot{\theta}\right) + k_f\left(u - u_f - L_f\theta\right) + k_r\left(u - u_r + L_r\theta\right) = 0$$

$$I_y\ddot{\theta} - L_fc_f\left(\dot{u} - \dot{u}_f - L_f\dot{\theta}\right) + L_rc_r\left(\dot{u} - \dot{u}_r + L_r\dot{\theta}\right) - L_fk_f\left(u - u_f - L_f\theta\right) + L_rk_r\left(u - u_r + L_r\theta\right) = 0$$

$$m_f\ddot{u}_f - c_f\left(\dot{u} - \dot{u}_f - L_f\dot{\theta}\right) + k_{tf}\left(u_f - h_f\right) - k_f\left(u - u_f - L_f\theta\right) = 0$$

$$m_r\ddot{u}_r - c_r\left(\dot{u} - \dot{u}_r + L_r\dot{\theta}\right) + k_{tr}\left(u_r - h_r\right) - k_r\left(u - u_r + L_r\theta\right) = 0$$

$$(2\text{-}1)$$

The above equations can be written in a dense form using matrix:

$$\mathbf{M}_v\ddot{\mathbf{U}}(t) + \mathbf{C}_v\dot{\mathbf{U}}(t) + \mathbf{K}_v\mathbf{U}(t) = \mathbf{P}(t) \tag{2-2}$$

where

$$\mathbf{M}_v = \begin{bmatrix} m_b & 0 & 0 & 0 \\ 0 & \theta_b & 0 & 0 \\ 0 & 0 & m_f & 0 \\ 0 & 0 & 0 & m_r \end{bmatrix} \tag{2-3}$$

$$\mathbf{C}_v = \begin{bmatrix} c_f + c_r & L_r c_r - L_f c_f & -c_f & -c_r \\ L_r c_r - L_f c_f & L_f^2 c_f + L_r^2 c_r & L_f c_f & -L_r c_r \\ -c_f & L_f c_f & c_f & 0 \\ -c_r & -L_r c_r & 0 & c_r \end{bmatrix} \tag{2-4}$$

$$\mathbf{K}_v = \begin{bmatrix} k_f + k_r & L_r k_r - L_f k_f & -k_f & -k_r \\ L_r k_r - L_f k_f & L_f^2 k_f + L_r^2 k_r & L_f k_f & -L_r k_r \\ -k_f & L_f k_f & k_f + k_{tf} & 0 \\ -k_r & -L_r k_r & 0 & k_r + k_{tr} \end{bmatrix} \tag{2-5}$$

$$\mathbf{U} = \begin{bmatrix} u_b & \theta_b & u_f & u_r \end{bmatrix}^{\mathrm{T}} \tag{2-6}$$

$$\mathbf{P} = \begin{bmatrix} 0 & 0 & k_{tf} h_f & k_{tr} h_r \end{bmatrix}^{\mathrm{T}} \tag{2-7}$$

Note that the input vector $\mathbf{P}$ in Eq. (2-7) is only suitable for the case in which the vehicle is moving on a road. If the vehicle is on a bridge, the bridge deflection due to vehicle-bridge interaction needs to be included as

$$\mathbf{P} = \begin{bmatrix} 0 & 0 & k_{tf}\left(h_f + y_f\right) & k_{tr}\left(h_r + y_r\right) \end{bmatrix}^{\mathrm{T}} \tag{2-8}$$

where y_f and y_r are the bridge deflections under the front and rear tires.

The parameters of the half-car model and the corresponding physical meanings are shown in Table 2-1.

Table 2-1. Physical meanings of half-car model parameters

m_b	m_f	m_r	c_f	c_r	k_f
Vehicle body mass	Front tire mass	Rear tire mass	Front suspension damping	Rear suspension damping	Front suspension stiffness

k_r	k_{tf}	k_{tr}	I_y	L_f	L_r
Rear suspension stiffness	Front tire stiffness	Rear tire stiffness	Pitching moment of inertia	Distance of COG and front axle	Distance of COG and rear axle

2.1.2 Full-car Model

If vehicle rolling motion is to be accounted in the vehicle model, the half-car model described in the last section is not sufficient. A full-car model, which has in total 7 degrees-of-freedom, is considered in this section, as shown in Fig. 2-2.
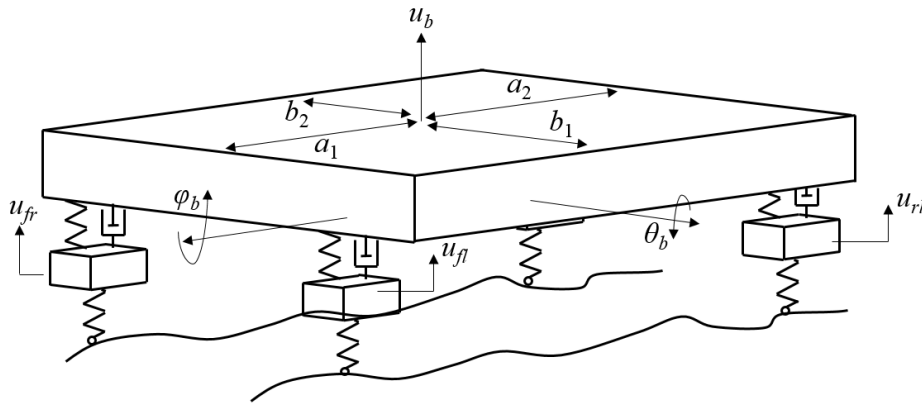
Fig. 2-2. Full-car model

To reduce the complexity of the full-car model, some assumptions are adopted to simplify the full-car model parameters, including: (a) left suspension stiffness, damping, and tire mass are equal to those of the right side, and (b) front rolling stiffness k_{Rf} is equal to rear torsion stiffness k_{Rr}, and is denoted as k_{Rf}.

Based on these assumptions, the equations of motion of the full-car model is written as:

$$m\ddot{u} + c_f\left(\dot{u} - \dot{u}_{fl} + b_1\dot{\varphi} - a_1\dot{\theta}\right) + c_f\left(\dot{u} - \dot{u}_{fr} - b_2\dot{\varphi} - a_1\dot{\theta}\right) + c_r\left(\dot{u} - \dot{u}_{rr} - b_1\dot{\varphi} + a_2\dot{\theta}\right)$$
$$+c_r\left(\dot{u} - \dot{u}_{rl} + b_2\dot{\varphi} + a_2\dot{\theta}\right) + k_f\left(u - u_{fl} + b_1\varphi - a_1\theta\right) + k_f\left(u - u_{fr} - b_2\varphi - a_1\theta\right) \qquad (2\text{-}9)$$
$$+k_r\left(u - u_{rr} - b_1\varphi + a_2\theta\right) + k_r\left(u - u_{rl} + b_2\varphi + a_2\theta\right) = 0$$

$$I_x\ddot{\varphi} + b_1c_f\left(\dot{u} - \dot{u}_{fl} + b_1\dot{\varphi} - a_1\dot{\theta}\right) - b_2c_f\left(\dot{u} - \dot{u}_{fr} - b_2\dot{\varphi} - a_1\dot{\theta}\right) - b_1c_r\left(\dot{u} - \dot{u}_{rr} - b_1\dot{\varphi} + a_2\dot{\theta}\right)$$
$$+b_2c_r\left(\dot{u} - \dot{u}_{rl} + b_2\dot{\varphi} + a_2\dot{\theta}\right) + b_1k_f\left(u - u_{fl} + b_1\varphi - a_1\theta\right) - b_2k_f\left(u - u_{fr} - b_2\varphi - a_1\theta\right)$$
$$-b_1k_r\left(u - u_{rr} - b_1\varphi + a_2\theta\right) + b_2k_r\left(u - u_{rl} + b_2\varphi + a_2\theta\right) + k_R\left(\varphi - \frac{u_{fl} - u_{fr}}{w}\right) = 0$$

$$(2\text{-}10)$$

$$I_y\ddot{\theta} - a_1c_f\left(\dot{u} - \dot{u}_{fl} + b_1\dot{\varphi} - a_1\dot{\theta}\right) - a_1c_f\left(\dot{u} - \dot{u}_{fr} - b_2\dot{\varphi} - a_1\dot{\theta}\right) + a_2c_r\left(\dot{u} - \dot{u}_{rr} - b_1\dot{\varphi} + a_2\dot{\theta}\right)$$
$$+a_2c_r\left(\dot{u} - \dot{u}_{rl} + b_2\dot{\varphi} + a_2\dot{\theta}\right) - a_1k_f\left(u - u_{fl} + b_1\varphi - a_1\theta\right) - a_1k_f\left(u - u_{fr} - b_2\varphi - a_1\theta\right)$$
$$+a_2k_r\left(u - u_{rr} - b_1\varphi + a_2\theta\right) + a_2k_r\left(u - u_{rl} + b_2\varphi + a_2\theta\right) = 0$$

$$(2\text{-}11)$$

$$m_f\ddot{u}_{fl} - c_f\left(\dot{u} - \dot{u}_{fl} + b_1\dot{\varphi} - a_1\dot{\theta}\right) - k_f\left(u - u_{fl} + b_1\varphi - a_1\theta\right)$$
$$-k_R\frac{1}{w}\left(\varphi - \frac{u_{fl} - u_{fr}}{w}\right) + k_{tf}\left(u_{fl} - h_{fl}\right) = 0 \qquad (2\text{-}12)$$

$$m_r\ddot{u}_{fr} - c_f\left(\dot{u} - \dot{u}_{fr} - b_2\dot{\varphi} - a_1\dot{\theta}\right) - k_f\left(u - u_{fr} - b_2\varphi - a_1\theta\right)$$
$$+k_R\frac{1}{w}\left(\varphi - \frac{u_{fl} - u_{fr}}{w}\right) + k_{tr}\left(u_{fr} - h_{fr}\right) = 0 \qquad (2\text{-}13)$$

$$m_r\ddot{u}_{rr} - c_r\left(\dot{u} - \dot{u}_{rr} - b_1\dot{\varphi} + a_2\dot{\theta}\right) - k_r\left(u - u_{rr} - b_1\varphi + a_2\theta\right) + k_{tr}\left(u_{rr} - h_{rr}\right) = 0 \qquad (2\text{-}14)$$

$$m_r\ddot{u}_{rl} - c_r\left(\dot{u} - \dot{u}_{rr} + b_2\dot{\varphi} + a_2\dot{\theta}\right) - k_r\left(u - u_{rl} + b_2\varphi + a_2\theta\right) + k_{tr}\left(u_{rl} - h_{rl}\right) = 0 \qquad (2\text{-}15)$$

The equations above can be written in a matrix form as Eq. (2-2), with the definition of mass, damping, and stiffness matrix as:

31

$$\mathbf{M}_v = \begin{bmatrix} m_b & 0 & 0 & 0 & 0 & 0 & 0 \\ 0 & I_x & 0 & 0 & 0 & 0 & 0 \\ 0 & 0 & I_y & 0 & 0 & 0 & 0 \\ 0 & 0 & 0 & m_f & 0 & 0 & 0 \\ 0 & 0 & 0 & 0 & m_f & 0 & 0 \\ 0 & 0 & 0 & 0 & 0 & m_r & 0 \\ 0 & 0 & 0 & 0 & 0 & 0 & m_r \end{bmatrix} \tag{2-16}$$

$$\mathbf{C}_v = \begin{bmatrix} c_{11} & c_{12} & c_{13} & -c_f & -c_f & -c_r & -c_r \\ c_{21} & c_{22} & c_{23} & -b_1 c_f & b_2 c_f & b_1 c_r & -b_2 c_r \\ c_{31} & c_{32} & c_{33} & a_1 c_f & a_1 c_f & -a_2 c_r & -a_2 c_r \\ -c_f & -b_1 c_f & a_1 c_f & c_f & 0 & 0 & 0 \\ -c_f & b_2 c_f & a_1 c_f & 0 & c_f & 0 & 0 \\ -c_f & b_1 c_r & -a_2 c_r & 0 & 0 & c_r & 0 \\ -c_f & -b_2 c_r & -a_2 c_r & 0 & 0 & 0 & c_r \end{bmatrix} \tag{2-17}$$

$$\mathbf{K}_v = \begin{bmatrix} k_{11} & k_{12} & k_{13} & -k_f & -k_f & -k_r & -k_r \\ k_{21} & k_{22} & k_{23} & -b_1 k_f & b_2 k_f & b_1 k_r & -b_2 k_r \\ k_{31} & k_{32} & k_{33} & a_1 k_f & a_1 k_f & -a_2 k_r & -a_2 k_r \\ -k_f & -b_1 k_f & a_1 k_f & k_{44} & -k_R/(b_1+b_2)^2 & 0 & 0 \\ -k_f & b_2 k_f & a_1 k_f & -k_R/(b_1+b_2)^2 & k_{55} & 0 & 0 \\ -k_f & b_1 k_r & -a_2 k_r & 0 & 0 & k_r + k_{tr} & 0 \\ -k_f & -b_2 k_r & -a_2 k_r & 0 & 0 & 0 & k_r + k_{tr} \end{bmatrix}$$

$$\tag{2-18}$$

$$\mathbf{U} = \begin{bmatrix} u & \varphi & \theta & u_{fl} & u_{fr} & u_{rr} & u_{rl} \end{bmatrix}^{\mathrm{T}} \tag{2-19}$$

$$\mathbf{P} = \begin{bmatrix} 0 & 0 & 0 & k_{tf} h_{fl} & k_{tf} h_{fr} & k_{tr} h_{rr} & k_{tr} h_{rl} \end{bmatrix}^{\mathrm{T}} \tag{2-20}$$

where the definitions of c_{ij} and k_{ij} are found in the work of Jazar (2017).

2.2 Bridge Model and Vehicle-Bridge Interaction

2.2.1 Beam Model and Slab Model

For most one-lane bridges, usually a beam model is sufficient to give bridge response prediction if the torsional effects of the bridge are negligible. An Euler–Bernoulli simply-supported beam model can be adopted as the bridge model for its simplicity. When the bridge is excited by the vehicle load, the dynamic equation of the bridge is expressed as Eq. (2-21).

$$\bar{m}\frac{\partial^2 y(x,t)}{\partial t^2} + c_b\frac{\partial y(x,t)}{\partial t} + EI\frac{\partial^4 y(x,t)}{\partial x^4} = L(x,t) \tag{2-21}$$

in which $\bar{m}$ is the mass per length, c_b is the viscous damping parameter, EI is the flexural stiffness, $y(x, t)$ is the time- and space-dependent displacement response, and $L(x, t)$ is the moving dynamic load on the bridge.

To solve this equation numerically, modal decomposition analysis is used, yielding

$$\mathbf{M}_b\ddot{\mathbf{q}} + \mathbf{C}_b\dot{\mathbf{q}} + \mathbf{K}_b\mathbf{q} = F_b \tag{2-22}$$

where $\mathbf{M}_b$, $\mathbf{C}_b$, and $\mathbf{K}_b$ are the diagonal modal mass, damping, and stiffness matrices, respectively, $\mathbf{q}$ contains the bridge displacement responses of each mode, and F_b is the column vector containing the input force of each mode with the form of

$$F_{b,i} = F_f\phi_i(x_f) + F_r\phi_i(x_r) \tag{2-23}$$

where ϕ_i is the ith mode of the bridge and x_f and x_r are the location of the front and rear tire, respectively, while F_f and F_r are the time- and space-dependent forces at the front and rear tire, respectively.

For the multiple-lane bridges, the bridge is modelled as a plate, with the governing equation as:

$$D_x \frac{\partial^4 w}{\partial x^4} + 2D_{xy} \frac{\partial^4 w}{\partial x^2 y^2} + D_y \frac{\partial^4 w}{\partial y^4} + c_b \frac{\partial w}{\partial t} + \bar{m}_p \frac{\partial^2 w}{\partial t^2} = L(x,t) \qquad (2\text{-}24)$$

where D_x, D_y are the flexural rigidities in x- and y- directions, respectively, and D_{xy} is the torsional rigidity of the orthotropic plate. $\bar{m}_p$ is mass per area of the plate model.

This equation can also be decomposed to the form shown in Eq. (2-22).

2.2.2 Vehicle-Bridge Interaction

In general, the vehicle-bridge interaction refers to the dynamic coupling phenomenon that occurs between a vehicle and a bridge. As shown in Eq. (2-2) and Eq. (2-22), the vehicle system and the bridge system are coupled with each other by the contact force terms. The difficulty to solve the coupling equations is due to the fact that the contact force changes its position at each time step (Liu et al, 2014). To deal with the vehicle-bridge interaction problem, some approaches are proposed. Lagrange multipliers are adopted to solve the equations of motion with an increase of the number of unknowns (Blejwas et al, 1979). A Guyan reduction scheme is used to condense the degrees-of-freedom of the vehicle system to the bridge system (Garg et al, 1984). The dynamic condensation method is adopted to eliminate the degrees-of-freedom in the vehicle system corresponding to the parts in direct contact with the bridge, making the contact force terms disappear in the coupling equation (Yang and Lin, 1995).

In this study, an iterative method, first proposed by Green and Cebon (1997) to consider

interaction between heavy vehicles and bridges, is used to solve the vehicle-bridge interaction problem. The process of this iteration is shown in Fig. 2-3.
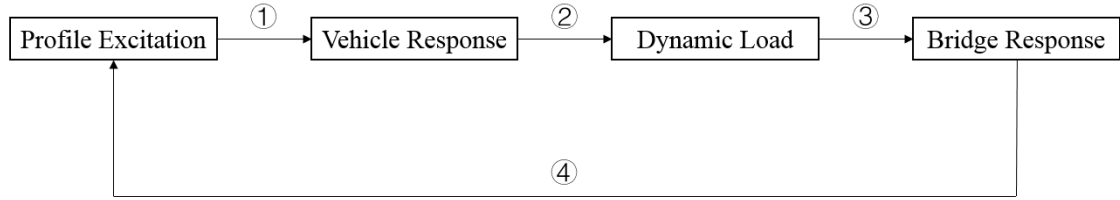
Fig. 2-3. Iterative solution process for vehicle-bridge interaction problem

In the first step, the vehicle response is calculated using the initial roughness input. The dynamic forces of the front and rear wheels on the bridge at each time step are expressed as Eq. (2-7). The bridge response under this dynamic force is calculated by the modal superposition method. The bridge displacement at each point at each subsequent time is then added to the initial roughness to form a new set of vehicle inputs and the front and rear tire forces are recalculated as follows:

$$F_f = k_{tf}[u_f - (h_f + y_f)], \quad F_r = k_{tr}[u_r - (h_r + y_r)] \tag{2-25}$$

This iteration process continues until the difference between the bridge displacements given by two consecutive iterations becomes smaller than an initially determined threshold value. In this process, the vehicle speed must be known in order to obtain the displacement of different points at their corresponding times.

The iterative process described in Fig. 2-3 can be processed in two different ways. The more direct processing method first calculates the time history of the vehicle response for the entire bridge crossing. The corresponding bridge response is then obtained and added

to the pavement roughness estimation; the entire roughness is thus updated in one step. This process, however, cannot be directly implemented in particle filters because the step-by-step data assimilation process requires the vehicle-bridge interaction analysis to be conducted at each time step. As a result of this limitation, the second processing method, which is employed in the particle filter, calculates the vehicle response and corresponding bridge response one step at a time. The estimated pavement roughness for the current step is then updated. This process is repeated until the convergence condition is met. This processing method is further explained in Chapter 4 and Chapter 5, in which vehicle-bridge interaction is considered in both the pavement roughness estimation problem and the vehicle parameter identification problem.

2.3 Bridge Modal Analysis of Two Bridges

As stated in the organization of the thesis described in Section 1.7, this study consists of four main chapters, from Chapter 3 to Chapter 6, corresponding to bridge modal mass identification, bridge pavement roughness estimation, vehicle parameter identification, and moving dynamic vehicle load identification. In each chapter, a field measurement was conducted at a real bridge to experimentally validate the corresponding algorithm. The bridges used for the validation include Tsukige Bridge and Yokohama Bridge. For the convenience of description, the brief introduction and some basic bridge modal analysis results for these two bridges are shown in this section.

2.3.1 Tsukige Bridge

Tsukige Bridge is located in Kimitsu City, Chiba Prefecture, Japan. This is a 59-m long,

simply supported box girder bridge with a width of 4.7 m. The width can allow only one vehicle to pass at one time. An overview of this bridge is shown in Fig. 2-4.

Fig. 2-4. Overview of Tsukige Bridge

This bridge has a physical mass of around 300 tons, according a technical report. To obtain the bridge dynamic properties, i.e., natural frequencies, damping ratios, and mode shapes, accelerometers were attached along the bridge, following the sensor arrangement in Fig. 2-5. Duration of the measurement of ambient vibration last around 6 hours.
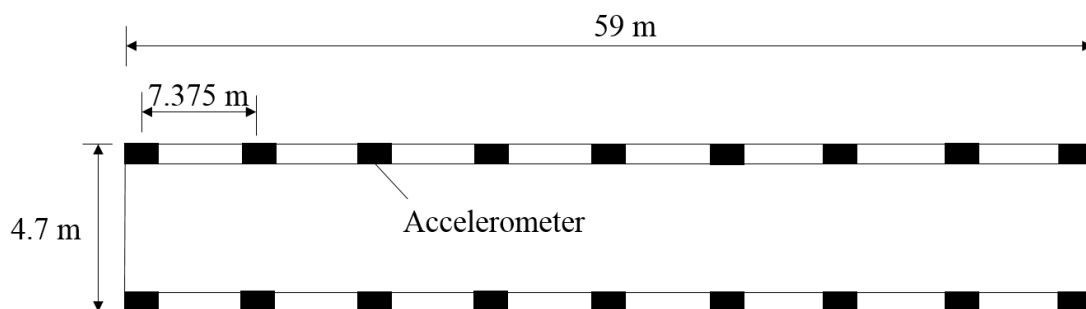
Fig. 2-5. Sensor arrangement for modal analysis of Tsukige Bridge

Due to the width limitation of the bridge, there is only one lane. Therefore, the bridge

vibration will be mostly governed by the bending modes. The torsional effects are thus ignored for this bridge.

The bridge natural frequencies are directly determined by picking the peaks on the PSD of the mid-span and 1/4-span responses. For this bridge, the frequencies of the first three bending modes are 2.15 Hz, 5.42 Hz, and 11.94 Hz, respectively. Mode shapes are extracted through the traditional methods of calculating the ratio of cross-spectrum amplitude over auto-spectrum of one reference node, at the corresponding frequency. The first three bending modes are shown in Fig. 2-6.
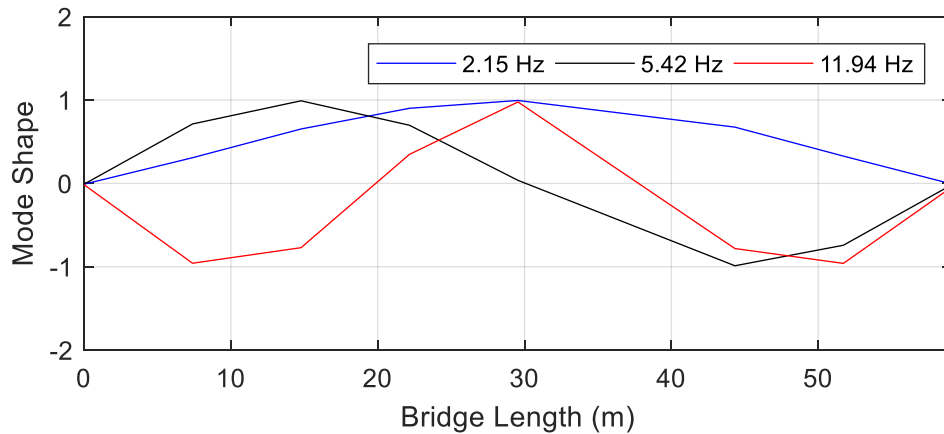
Fig. 2-6. Mode shapes of Tsukige Bridge

The damping ratio of the bridge is determined by counting the number of cycles and the decrease of acceleration amplitudes after an impulse excitation within a time period (Chopra, 2017). The formula of calculating damping ratio using this method is shown in Eq. (2-26).

$$\zeta = \frac{1}{2\pi j} \ln \frac{\ddot{y}_i}{\ddot{y}_{i+j}} \tag{2-26}$$

where i is the cycle index at which the counting starts and j is the number of cycles

counted in this period. Ideally, this method is suitable for the case of free vibration response. In the real measurement, the bridge transient vibration after a vehicle left the bridge is used. The damping ratio is estimated to be 0.39 % and is assumed to be equal to all of the three modes.

The bridge modal mass can be calculated through the following formula (Chopra, 2017).

$$M_n = \int_0^L m(x) \left[\phi_n(x) \right]^2 dx \qquad (2\text{-}27)$$

where M_n is the nth mode shape, $m(x)$ is the mass distribution function in the longitudinal direction of the bridge, and $\phi_n(x)$ is the nth mode shape.

Assuming the bridge physical mass is uniformly distributed along the bridge, the bridge modal mass of the first three modes are calculated to be 134.4, 139.9, and 154.9 ton, respectively. Note that the modal mass usually varies according to different normalization assumption on the mode shapes. In this thesis, all the modal mass values are based on the normalized mode shapes whose largest value is set to one, as those shown in Fig. 2-6.

2.3.2 Yokohama Bridge

A two-span continuous steel-box girder bridge in Yokohama is also used as the test bridge. This is a 40.15-meter long, two-span girder bridge. This bridge has a width of 10 m with two lanes, for two opposite directions, respectively. In the middle of the bridge, there is a support, making a two-span continuous bridge.

A 6-hour ambient vibration measurement was conducted to obtain basic dynamic properties of this bridge. Thirty-four wireless accelerometers were installed on the bridge with a distance of around 2.6-m between each other to obtain the mode shapes of the bridge. Although this bridge mode shape extraction technique requires the input of the bridge to be white-noise, this assumption is made due to the randomness of time and position of the passing vehicles, the bridge pavement roughness, passing pedestrians, and other environment ambient input signals.
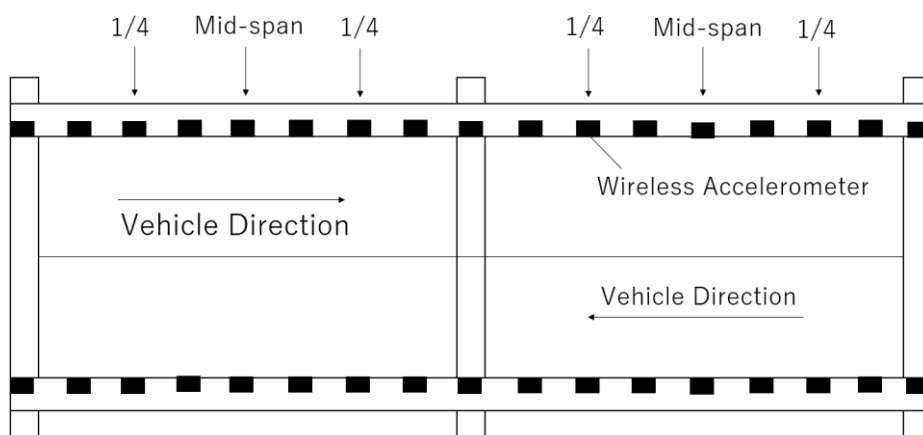
Fig. 2-7. Sensor arrangement for modal analysis of Yokohama Bridge

Using the same method as in Tsukige Bridge, the mode shapes of the first four modes and the corresponding natural frequencies were extracted and are shown in Fig. 2-8 and Table 2-2, respectively. The modes with higher frequencies have much smaller peak values according to the PSD of the measurement data and are thus not shown in these figures.

(a) First mode

(b) Second mode

(c) Third mode

41
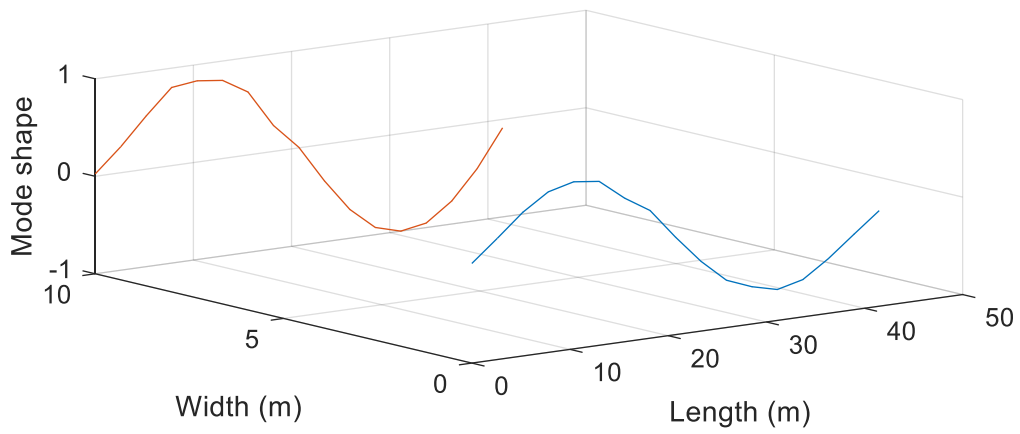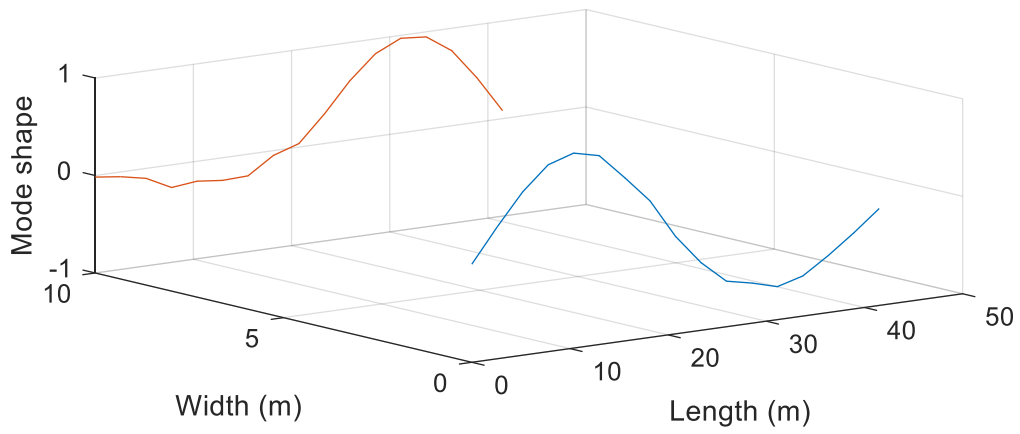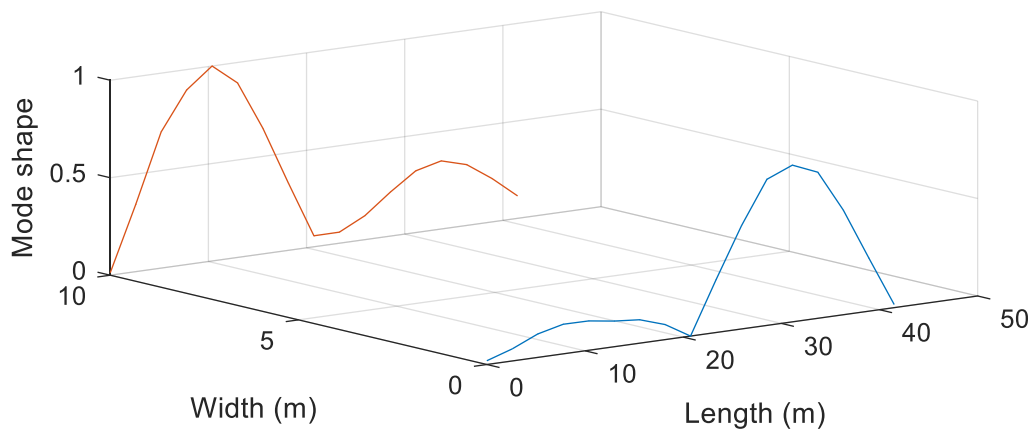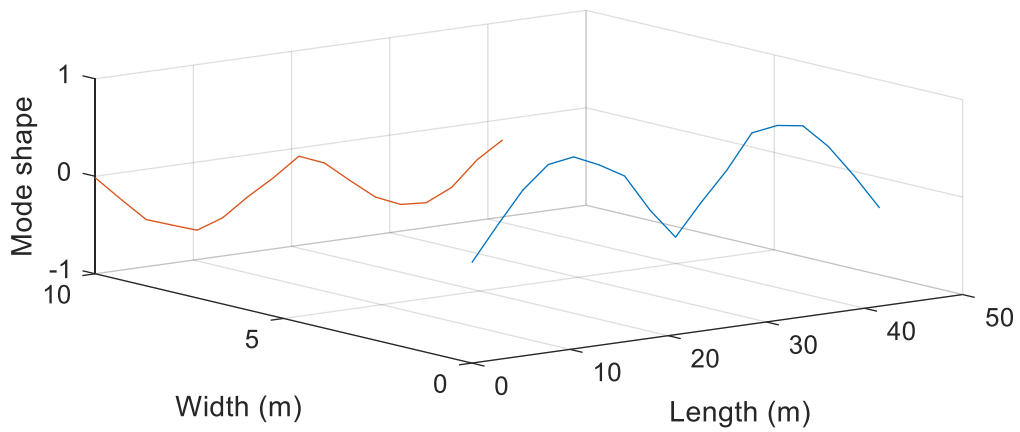
(d) Fourth mode

Fig. 2-8. Mode shapes of Yokohama Bridge

Table 2-2. Mode shape descriptions of Yokohama Bridge

No.	Frequency	Description
1	3.76 Hz	First bending mode
2	5.00 Hz	First torsional mode
3	5.62 Hz	Second bending mode
4	6.71 Hz	Second torsional mode

Eq. (2-26) is also applied to Yokohama Bridge and a damping ratio of 0.65 % is adopted

for each mode of this bridge.

Chapter 3 Bridge Modal Mass Identification Based on Vehicle Dynamic Tire Force Estimation from Vehicle Body Response Measurement

3.1 Overview

Bridge modal parameters, including modal mass, are important factors that directly affect the bridge responses under various excitations. To identify these parameters, simultaneous measurement of the bridge excitation and its corresponding bridge responses is usually necessary. However, as stated in Section 1.4, traditional methods of exciting a bridge by an instrumented hammer, a drop-weight, or an electronic shaker have many limitations including small impact energy, narrow frequency range, requirement of power supply, as well as other site-specific difficulties. On the other hand, the vehicle-induced load, which excites the bridge through vehicle-bridge interaction, can be used in the bridge parameter identification if the vehicle-bridge contact force is well estimated.

In this chapter, a two-step method to estimate bridge modal mass is proposed. The first step corresponds to an algorithm for estimating the dynamic components of the vertical tire contact forces through the measurement of the vehicle body acceleration and angular velocity at selected locations on an ordinary vehicle. A Kalman filter with the tire forces augmented in the system state vector is employed. An observability analysis and a sensitivity analysis provide theoretical foundation of the method. Numerical examples

43

with different road roughness conditions show that the proposed algorithm has good accuracy and robustness against noises and modelling errors. A commercial van-type vehicle was used in a field measurement to validate the proposed method. The estimated dynamic tire forces show a good agreement with reference measurements.

After obtaining the dynamic tire forces, the forces are used for bridge modal mass identification together with the simultaneously measured bridge acceleration responses. As will be discussed in later sections, modal mass values are the only unknown variables for the bridge system. A genetic algorithm is then adopted to optimize the modal mass values.

The flow chart of this chapter is shown in Fig. 3-1.

Output	System	Input		Input	System	Output
Vehicle Response (Measured)	Half-car system (Known)	Tire Force (To vehicle) (Target)		Tire Force (To bridge) (Known)	Bridge modal mass (Target)	Bridge Response (Measured)

(Kalman filter)

(State tracking problem)

(Genetic Algorithm)

(Parameter identification problem)
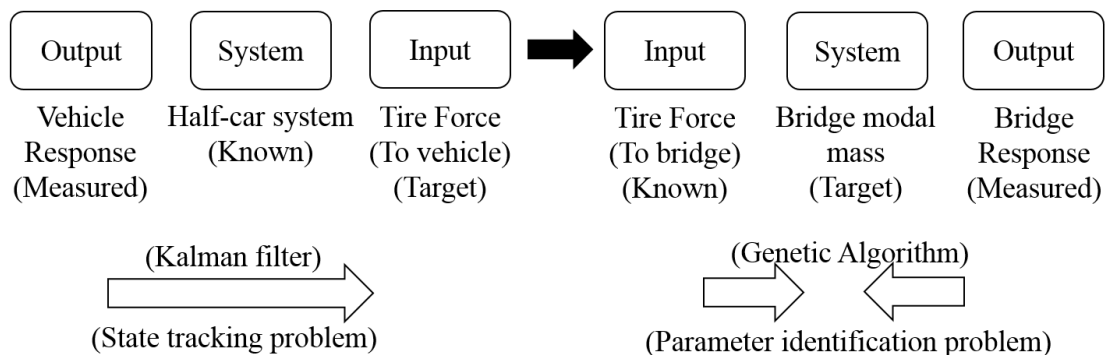
Fig. 3-1. Flow chart of a two-step modal mass identification method

3.2 Dynamic Tire Force Estimation from Vehicle Responses by Augmented Kalman Filter

As discussed in previous sections, for the purpose of bridge modal mass identification, both the excitation and the responses of the bridge are necessary. For the case where a

sensor-equipped vehicle is used for bridge modal mass identification, the force between the vehicle tire and the bridge deck will be the excitation, which needs to be correctly obtained.

In this section, the process of tire force estimation from vehicle responses is introduced. This estimation process is first described in state space, where the system equation, observation equation, state vector, and the observation vector are discussed. The observability analysis provides the reason of choosing the vehicle body acceleration and angular velocity as the measurement. The algorithm is verified by a numerical example, which is then followed by an error analysis. Sensitivity analysis is conducted to give the principles to choose the sensor placement on the vehicle body.

As the bridge length is usually much larger than the sizes of other two dimensions, most bridge parameters of interests are those governing the bridge bending motion as a beam model. Accordingly, the forces at vehicle front tires (front left and front right) are considered as one force acting on the bridge in the vertical direction. In the same manner, the forces at the rear tires are considered as one force, too. Therefore, there is no need to distinguish the left tire force from the right tire force. From this perspective, a half-car model, in which the two front tires are represented by only one degree-of-freedom as shown in Fig. 2-1, is adopted, while a four-wheel full-car model shown in Fig. 2-2 is used in the numerical examples to generate vehicle responses considering the effect of vehicle rolling motion.

3.2.1 Implementation of Augmented Kalman Filter

Theoretically, the tire contact forces are induced by the relative deflection between the vehicle tires and the pavement roughness. For the half-car model, the front tire force F_f and rear tire force F_r are expressed as Eq. (3-1).

$$
\begin{aligned}
F_f &= k_{tf}\left(u_f - h_f\right) \\
F_r &= k_{tr}\left(u_r - h_r\right)
\end{aligned}
\tag{3-1}
$$

Note that these two equations correspond to the case in which the vehicle is moving on a rigid road. For the cases that is more related to this study, the vehicle runs on the bridge to give bridge modal mass identification values. In this case, the bridge deflection induced will also affect the tire forces and is considered by Eq. (3-2).

$$
\begin{aligned}
F_f &= k_{tf}\left(u_f - \left(h_f + y_f\right)\right) \\
F_r &= k_{tr}\left(u_r - \left(h_r + y_r\right)\right)
\end{aligned}
\tag{3-2}
$$

To estimate the dynamic tire forces from vehicle responses, the force terms should be included in the state vector of Kalman filter, known as an augmented Kalman filter. To achieve this, the equation of motion of the vehicle half-car model shown in Eq. (2-2) is modified by moving the terms with tire stiffness to the right-hand side of the equations, giving:

$$
\mathbf{M}_v \ddot{\mathbf{U}}(t) + \mathbf{C}_v \dot{\mathbf{U}}(t) + \mathbf{K}_v' \mathbf{U}(t) = \mathbf{P}'(t)
\tag{3-3}
$$

where $\mathbf{M}_v$, $\mathbf{C}_v$, and $\mathbf{U}$ are the same with Eq. (2-3), Eq. (2-4), and Eq. (2-6), and

$$
\mathbf{K}_v' =
\begin{bmatrix}
k_f + k_r & L_r k_r - L_f k_f & -k_f & -k_r \\
L_r k_r - L_f k_f & L_f^2 k_f + L_r^2 k_r & L_f k_f & -L_r k_r \\
-k_f & L_f k_f & k_f & 0 \\
-k_r & -L_r k_r & 0 & k_r
\end{bmatrix}
\tag{3-4}
$$

$$\mathbf{P}^{'} = \begin{bmatrix} 0 & 0 & -F_f & -F_r \end{bmatrix}^{\mathrm{T}} \tag{3-5}$$

In this manner, the tire force terms are explicitly expressed in the input vector of the equation of motion, making it possible to implement the augmented Kalman filter to estimate the system input. Moreover, by comparing Eq. (3-4) and Eq. (2-5), it is observed that the tire stiffness terms k_{tf} and k_{tr} disappear in the newly developed equations. This will reduce the influence from the estimation error of the tire stiffness.

In addition to the tire forces, the vehicle responses and their corresponding first-order derivatives are also included in the state vector $\mathbf{X}$:

$$\mathbf{X} = \begin{bmatrix} u_b & \theta_b & u_f & u_r & \dot{u}_b & \dot{\theta}_b & \dot{u}_f & \dot{u}_r & F_f & F_r \end{bmatrix}^{\mathrm{T}} \tag{3-6}$$

As expressed in Eq. (3-2), the tire forces are affected by many factors, including vehicle parameters, tire movements, bridge deck roughness, and the vehicle-bridge interaction properties. Furthermore, the roughness is random and the vehicle front and rear properties are different. Analytical description of the relation between the tire forces at time step k and $k+1$ is thus difficult. Instead, a random walk model (Doumiati et al, 2012) based on Markov process is adopted to describe the time evolution of the tire forces.

$$\begin{aligned} F_{f,k+1} &= F_{f,k} + \eta_{f,k} \\ F_{r,k+1} &= F_{r,k} + \eta_{r,k} \end{aligned} \tag{3-7}$$

where η_f and η_r are independent zero-mean Gaussian processes governing the time evolution of the front and rear tire forces, respectively.

From the equation of motion shown in Eq. (3-3), the continuous system state equation is written as

$$\dot{\mathbf{X}} = \mathbf{A}\mathbf{X} + \varsigma \qquad (3\text{-}8)$$

where ς is the system model error and $\mathbf{A}$ is the continuous system transition matrix with the following form.

$$\mathbf{A} = \begin{bmatrix} \mathbf{O}_{4\times4} & \mathbf{I}_{4\times4} & \mathbf{O}_{4\times2} \\ -\mathbf{M}_v^{-1}\mathbf{K}_v^{'} & -\mathbf{M}_v^{-1}\mathbf{C}_v & \mathbf{Z}_{4\times2} \\ \mathbf{O}_{4\times4} & \mathbf{O}_{4\times4} & \mathbf{O}_{2\times2} \end{bmatrix} \qquad (3\text{-}9)$$

in which $\mathbf{O}$ is zero-matrix, $\mathbf{I}$ is unit matrix, and

$$\mathbf{Z} = \begin{bmatrix} 0 & 0 & 1/m_f & 0 \\ 0 & 0 & 0 & 1/m_r \end{bmatrix}^{\mathrm{T}} \qquad (3\text{-}10)$$

The continuous system state equation is discretized to the general form of Eq. (1-1) using the Euler discretization method, where

$$\mathbf{A}_d = e^{\mathbf{A}\mathrm{d}t} \approx \mathbf{I} + \mathbf{A}\mathrm{d}t \qquad (3\text{-}11)$$

The discretized system transition equation, which connects the state vector of the current time step and the next step, is expressed as

$$\mathbf{X}_{k+1} = \mathbf{A}_d\mathbf{X}_k + \varsigma_k \qquad (3\text{-}12)$$

The vehicle body vertical acceleration and angular velocity are measured to estimate the tire forces. The sensor is located on the vehicle body at a distance d_{sen} from the front axle, as shown in Fig. 2-1. The observation vector is expressed as

$$\mathbf{Y}_k = \begin{bmatrix} \ddot{u}_{b,sen} & \dot{\theta}_{b,sen} \end{bmatrix}^{\mathrm{T}} \qquad (3\text{-}13)$$

where the subscript 'sen' indicates the vehicle responses at the sensor location. Based on the rigid vehicle body assumption, the responses at the sensor location is related with the responses at the vehicle center of gravity through Eq. (3-14).

$$\ddot{u}_{b,sen} = \ddot{u}_b - \left(L_f - d_{sen}\right)\ddot{\theta}_b$$
$$\ddot{\theta}_{b,sen} = \ddot{\theta}_b \tag{3-14}$$

The observation matrix $\mathbf{C}_d$ becomes

$$\mathbf{C}_d = \begin{bmatrix} \mathbf{T}_1 + \mathbf{T}_2 & 0 & 0 \\ \mathbf{T}_3 & 0 & 0 \end{bmatrix}_{2\times10} \tag{3-15}$$

where

$$\mathbf{T}_1 = -\frac{1}{m_b}\begin{bmatrix} k_f + k_r & L_r k_r - L_f k_f & -k_f & -k_r & c_f + c_r & L_r c_r - L_f c_f & -c_f & -c_r \end{bmatrix} \tag{3-16}$$

$$\mathbf{T}_2 = \frac{L_f - d_{sen}}{I_y}\begin{bmatrix} L_r k_r - L_f k_f & L_f^2 k_f + L_r^2 k_r & L_f k_f & -L_r k_r & L_r c_r - L_f c_f & L_f^2 c_f + L_r^2 c_r & L_f c_f & -L_r c_r \end{bmatrix}$$

$$\tag{3-17}$$

$$\mathbf{T}_3 = \begin{bmatrix} 0 & 0 & 0 & 0 & 0 & 1 & 0 & 0 \end{bmatrix} \tag{3-18}$$

With the system equation and the observation equation deduced, the Kalman filter procedure can be conducted following the process described in Section 1.6.1.

Due to the vehicle pitching and rolling motion, the acceleration at front left, front right, rear left, and rear right of the vehicle body are different. Each of them is used as the vehicle body acceleration in Eq. (3-14) to give tire force estimation, i.e., the augmented Kalman filter is conducted four times from the measurement at four sensor locations. Although each measurement gives force estimation at both front and rear tire, only the

estimation close to the sensor location is adopted, i.e., the front tire force is estimated using the front sensors while the rear tire force from rear sensors. The reason is discussed in the sensitivity analysis in Section 3.2.4. The whole process of tire force estimation is shown in the flowchart in Fig. 3-2.
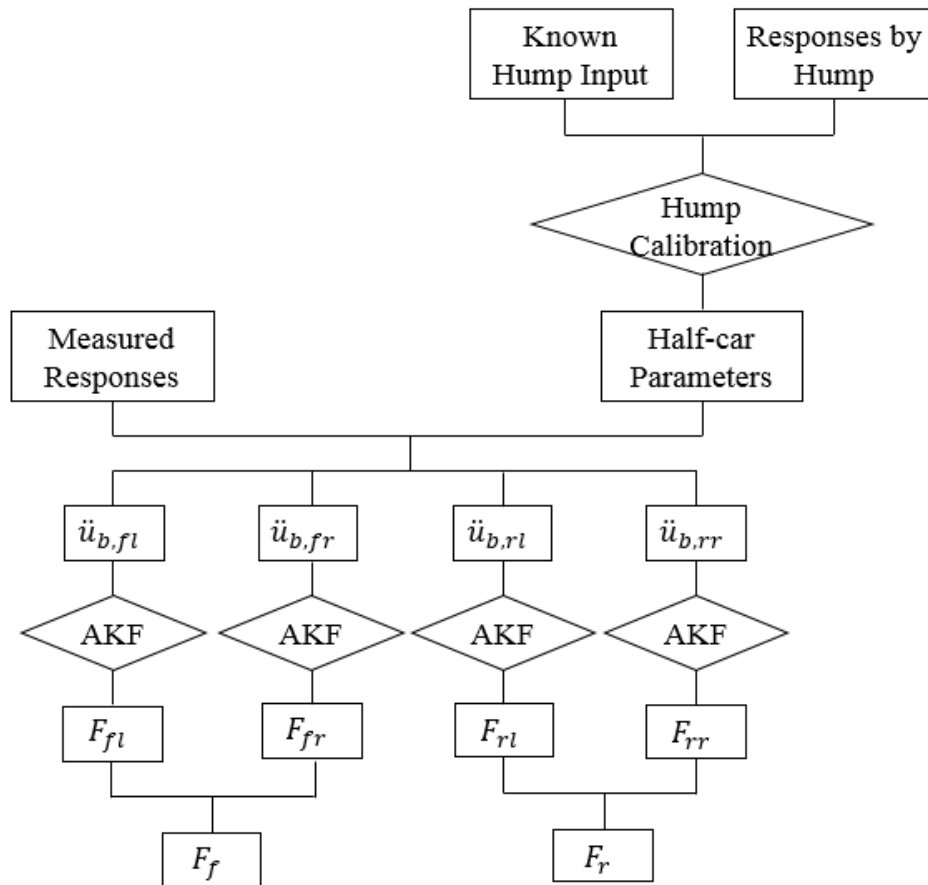
Fig. 3-2. Flow chart of tire force estimation from vehicle responses

3.2.2 Observability Analysis

As described in last section, a random walk model is adopted to describe the evolution process of the front and rear tire forces. Because this model does not reflect the physical relation between two consecutive steps, an observability check is conducted. A system

state can be identified only when this state is observable.

A system is defined as completely observable if the observation matrix $\mathbf{O}$ has full rank (Chatzis et al, 2015; Hermann et al, 1977):

$$\mathbf{O} = \begin{bmatrix} \mathbf{C}_d & \mathbf{C}_d\mathbf{A}_d & \mathbf{C}_d\mathbf{A}_d^2 & \cdots & \mathbf{C}_d\mathbf{A}_d^{M-1} \end{bmatrix} \tag{3-19}$$

where M is the length of the state vector. From the state vector used for tire force estimation in Eq. (3-6), the value of M is 10, including 8 vehicle response terms and 2 tire force terms.

By substituting the system transition matrix $\mathbf{A}_d$ and the observation matrix $\mathbf{C}_d$ of Eq. (3-11) and Eq. (3-15) with those of the half-car formulation, the rank of the observation matrix is calculated. However, in many cases, only the target states need to be observable even if the system is not completely observable. The observability of each state variable is determined by examining the rank of the matrix after removing the corresponding row of the matrix. If the rank is reduced by removing this row, the corresponding state is observable. The observable states for different measurement combinations for half-car model is listed in Table 3-1.

Table 3-1. Observability for different measurement combinations on half-car model

Vehicle model	Case	Measurement	Observable quantities
Half-car	1	$\ddot{u}_b, \dot{\theta}_b$	$\dot{\theta}_b, F_f, F_r$
	2	$\ddot{u}_b, \dot{\theta}_b, u_b, \theta_b$	All

As shown in Table 3-1, for the half-car model, the combination of vehicle body vertical

acceleration and angular velocity measurement leads to observable front and rear tire forces. Although other terms in the state vector are not observable under this combination of measurement, the target dynamic tire forces are observable, which is sufficient for the tire force estimation problem.

On the other hand, if the vehicle body displacement and angle are included in the observation vector, all the system states can be observable. However, as the vehicle deflection and angle are usually not easily measured, only vehicle body acceleration and angular velocity are used. Considering that the vehicle tire force terms are already observable, excluding displacement and angle does not significantly affect the results.

The observability check is also conducted for the full-car model. Because the full-car model is more complicated than the half-car model, more measurement is needed to make the system observable. The cases for different combination of measurement for full-car model are listed in Table 3-2. From this check, in the full car model, in order to make the tire force terms to be observable, acceleration data on one vehicle tire must be included. However, measurement on tire is usually labor-consuming and not convenient. This provides another reason for choosing the half-car model for the following tire force estimation procedure described in next section.

Table 3-2. Observability for different measurement combinations on full-car model

Vehicle model	Case	Measurement	Observable quantities
Full-car	1	$\ddot{u}_b, \dot{\theta}_b, \dot{\varphi}_b$	$\dot{\theta}_b, \dot{\varphi}_b$

	2	$\ddot{u}_b, \dot{\varphi}_b, \dot{\theta}_b, u_b, \varphi_b, \theta_b$	$u_b, \varphi_b, \theta_b, \dot{u}_b, \dot{\varphi}_b, \dot{\theta}_b, \dot{u}_{fl}, \dot{u}_{rl}, \dot{u}_{fr}, \dot{u}_{rr}$
	3	$\ddot{u}_b, \dot{\varphi}_b, \dot{\theta}_b, \ddot{u}_{fl}$	$\dot{\varphi}_b, \dot{\theta}_b, F_{fl}, F_{rl}, F_{fr}, F_{rr}$
	4	$\ddot{u}_b, \dot{\varphi}_b, \dot{\theta}_b, u_b, \varphi_b, \theta_b, \ddot{u}_{fl}$	All

3.2.3 Numerical Verification and Error Analysis

3.2.3.1 Verification without Noise and Error

In this section, a numerical example is given to verify the algorithm of tire force identification from vehicle body acceleration and angular velocity measurement. To make this example more closed to the real case, a full-car model is used for the simulation of the vehicle responses from the road roughness excitation. Vehicle body acceleration and angular velocity above each of the four tires are calculated through Newmark-beta method. The estimation process is then conducted following the flow chart shown in Fig. 3-2.

A 60-meter pavement roughness of class A is generated following ISO 8608 (1995), where the PSD of the roughness is expressed in terms of the summation of a series of harmonics (Agostinacchio et al, 2014). Details of the generation process will be explained in Chapter 4, where the pavement roughness becomes the target of the estimation. The roughness used in this chapter is shown in Fig. 3-3.
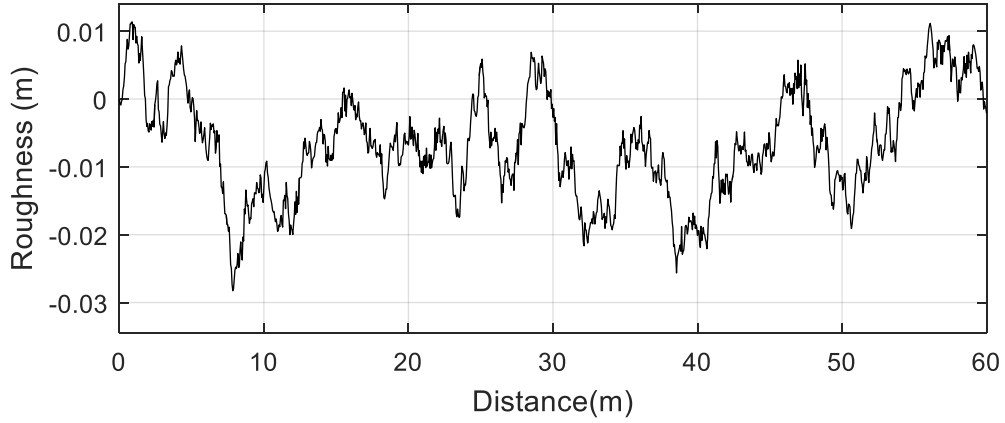
Fig. 3-3. A 60-meter road roughness of class A

To consider the effect from pavement roughness on the rolling motion of the full-car model and its further influence on the tire force estimation, different combination cases of the pavement roughness along the left and right path of the full-car model are studied. These cases are shown in Eq. (3-20).

$$\text{case 1: } R_{right}(x) = R_{left}(x) = R(x)$$
$$\text{case 2: } R_{right}(x) = 5R_{left}(x) = 5R(x) \qquad (3\text{-}20)$$
$$\text{case 3: } R_{right}(x) = -5R_{left}(x) = -5R(x)$$

where $R(x)$ is the roughness shown in Fig. 3-3, $R_{left}(x)$ and $R_{right}(x)$ are the roughness of the left and right paths, respectively, and x is the distance along the road. From this definition, Case 1 indicates that the left and right tires share the identical roughness input. In case 2, the two paths have different roughness amplitudes but with the same phases. In case 3, both amplitudes and phases are different.

A vehicle represented by the full-car model is simulated to pass across the roughness of these three cases. The model parameters are listed in Table 3-3.

54

Table 3-3. Full-car model parameters used in simulation

m_b(kg)	m_f(kg)	m_r(kg)	I_x(kg/m^2)	I_y(kg/m^2)	k_f(N/m)	k_r(N/m)	k_R(Nm/rad)
840	53	76	820	1100	10000	13000	10000
c_f(Ns/m)	c_r(Ns/m)	k_{tf}(N/m)	k_{tr}(N/m)	a_1(m)	a_2(m)	b_1(m)	b_2(m)
2500	2500	200000	200000	1.4	1.45	0.7	0.75

The vehicle responses, including vehicle body accelerations above the four tires (front left, front right, rear left, and rear right) and the vehicle pitching and rolling angular velocities, are calculated through a Newmark-beta simulation. The simulated vehicle body responses are shown in Fig. 3-4.

(a) Body acceleration (front left)   (b) Angular velocity
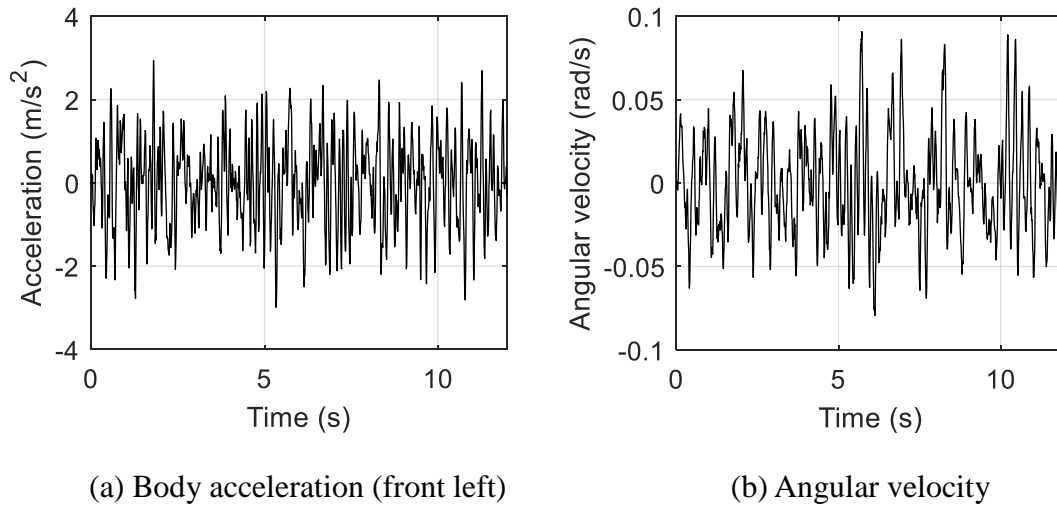
Fig. 3-4. Simulated vehicle responses

The estimation results of vehicle front tire force are given in Fig. 3-5 to Fig. 3-7 for cases 1 – 3, respectively. For each case, the front tire force is estimated twice, i.e., from the front left response (denoted as FL in legends) and the front right response (denoted as FR in legends), respectively. For clear observation, the time history is zoomed into a one-

55

second section. The results for the rear tire forces are not shown here but similar with the

front figures.
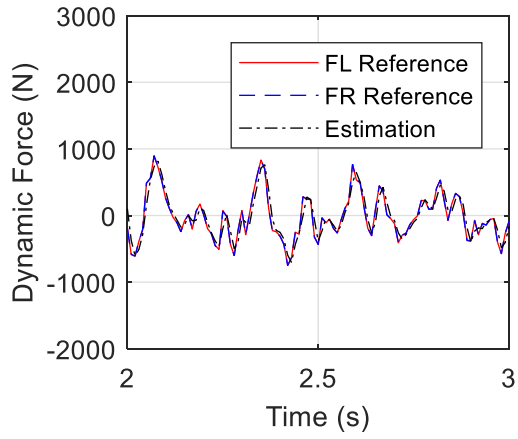
(a) Estimation from FL measurement
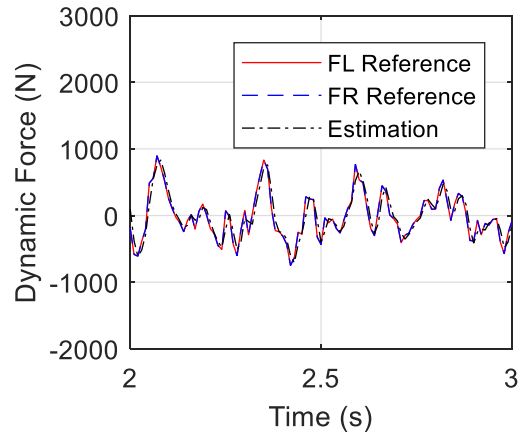
(b) Estimation from FR measurement
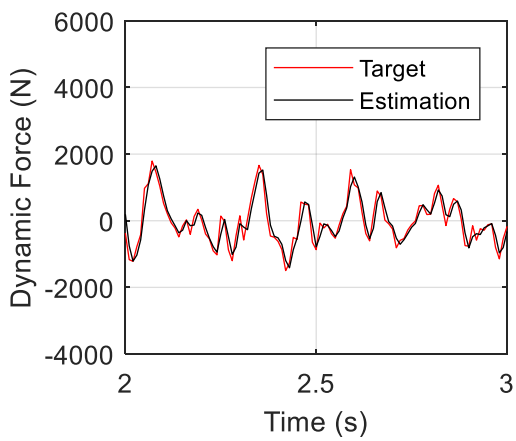
(c) Estimation of front total force
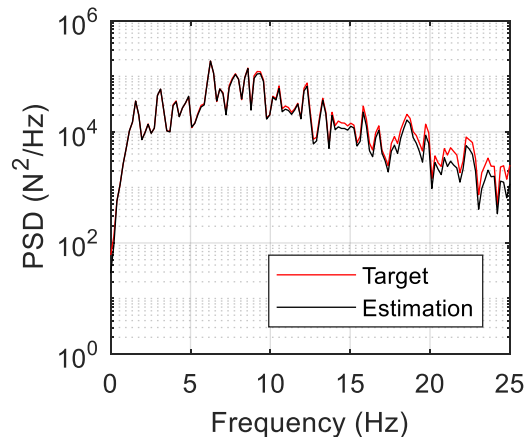
(d) PSD of front total force

Fig. 3-5. Front force estimation of case 1
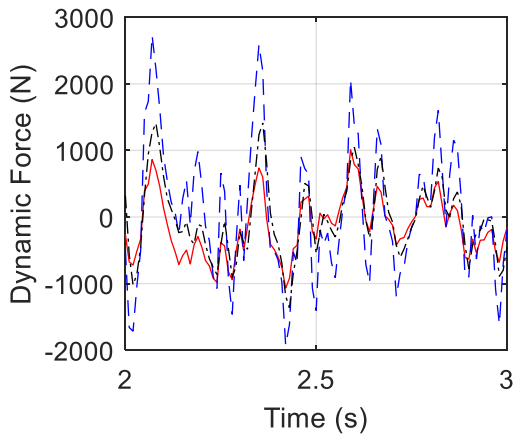
(a) Estimation from FL measurement   (b) Estimation from FR measurement
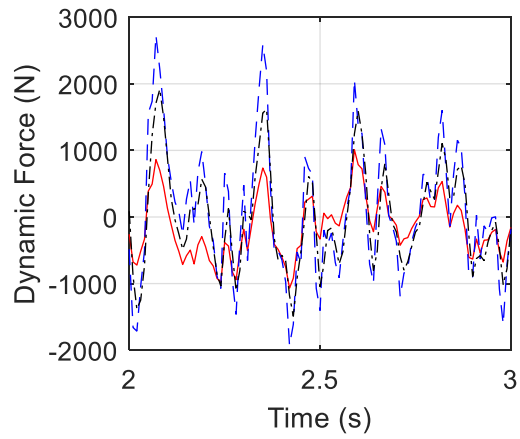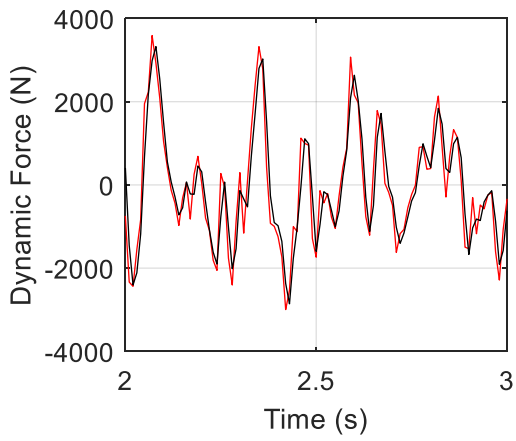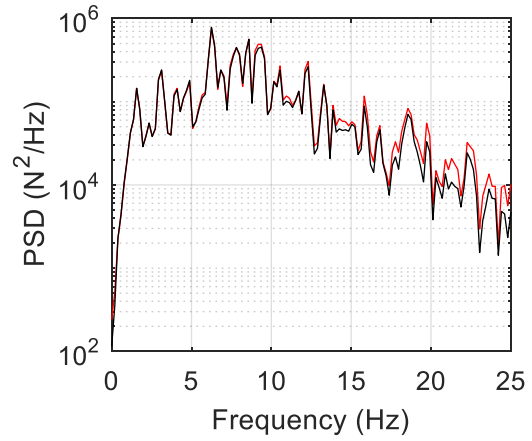
(c) Estimation of front total force   (d) PSD of front total force

Fig. 3-6. Front force estimation of case 2
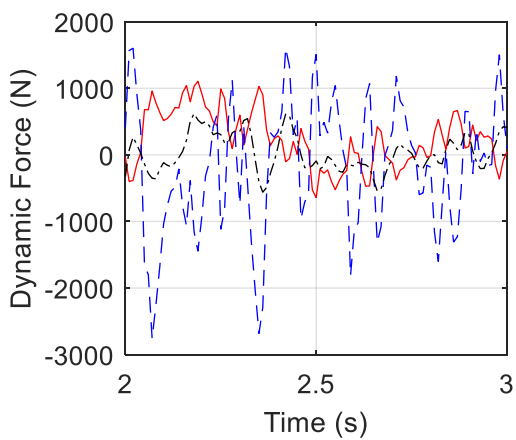
(a) Estimation from FL measurement   (b) Estimation from FR measurement
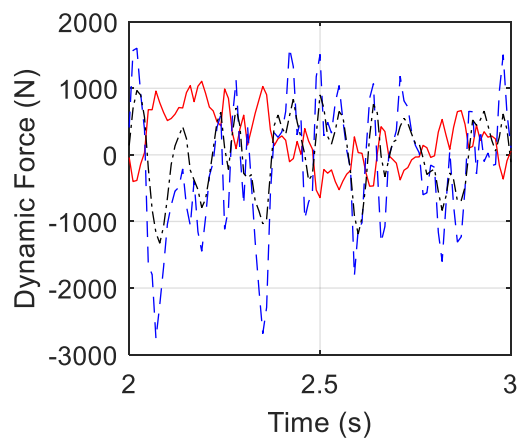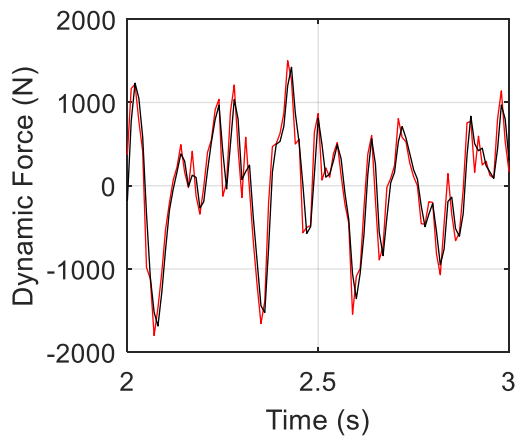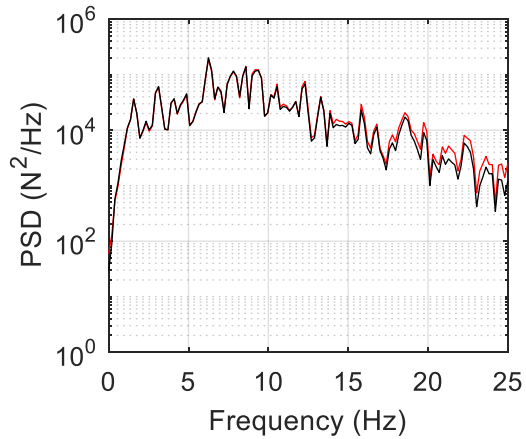
(c) Estimation of front total force   (d) PSD of front total force

Fig. 3-7. Front force estimation of case 3

In case 1, where the left and right paths share the identical roughness, the values of the front left and front right tire forces are close to each other, indicating that the rolling effect is negligible. The measurement at both left and right sides give estimation close to the references.

In case 2, the amplitudes of the left and right path are different while the paths still have the same phases. Accordingly, the left and right forces show clearly different amplitudes in the time history. The estimated forces are in between the real forces at the left and rear tires, as shown in Fig. 3-6 (a) and (b). The force estimation is not accurate when compared to the references. However, when the estimations from the left and right measurement are added and compared with the total front force, the estimation agrees well with the reference in both the time and the frequency domain.

In case 3, where the left and right paths have different amplitudes and opposite phases,

the force estimation of each tire force seems different from the references. However, the total force is estimated with a good accuracy.

3.2.3.2 Influence from Sensor Noise and Vehicle Modelling Errors

In the real case, the measurement of vehicle body responses will be affected by sensor noise. To account for this influence, artificial white noises with a zero-mean Gaussian distribution with a standard deviation of 10 % of the corresponding RMS value are added to the vehicle accelerations and angular velocities, to check the robustness of this algorithm against sensor noise, as expressed by Eq. (3-21).

$$
\begin{aligned}
\ddot{u}_{sen,m} &= \ddot{u}_{sen} + E_P N_{noise} \sigma\left(\ddot{u}_{sen}\right) \\
\dot{\theta}_{sen,m} &= \dot{\theta}_{sen} + E_P N_{noise} \sigma\left(\dot{\theta}_{sen}\right)
\end{aligned}
\tag{3-21}
$$

where E_P is the noise level, N_{noise} is a noise with a standard normal distribution, $\sigma(\cdot)$ is the standard deviation of the 'measured' response, and the subscript 'm' indicates 'measured'.

On the other hand, to conduct tire force estimation, the half-car parameters shown in Fig. 2-1 need to be known in advance. In the real case, these parameters are identified through a process called hump calibration, where a portable hump with a known size is used to excite the vehicle passing over it while the vehicle body responses are measured. As the input and output are both available, the vehicle parameters can be identified through parameter identification methods. In this hump calibration, the genetic algorithm is used, in which a target function is set to minimize the difference between measured vehicle responses and predicted responses from the half-car model parameters in the frequency domain. Details of the hump calibration process is described in the work from Zhao (2017).

In this numerical example, the hump calibration is conducted for the full-car model to obtain its corresponding half-car model parameters as listed in Table 3-4. Note that these parameters are different from those shown in Table 3-3 because the adopted vehicle model is different

Table 3-4. Calibrated half-car parameters

m_b(kg)	m_f(kg)	I_y(kg/m^2)	k_f(N/m)	k_r(N/m)
833	114	1168	21900	21660
c_f(Ns/m)	c_r(Ns/m)	k_{tf}(N/m)	k_{tr}(N/m)	L_f(m)
2703	2445	346800	416000	1.48

The estimation process was conducted again with 10 % noise-polluted responses and the calibrated half-car parameter with errors. Only the summation of front left and front right force is given because the rolling effect has been shown in the last section.

(a) Time domain   (b) Frequency domain
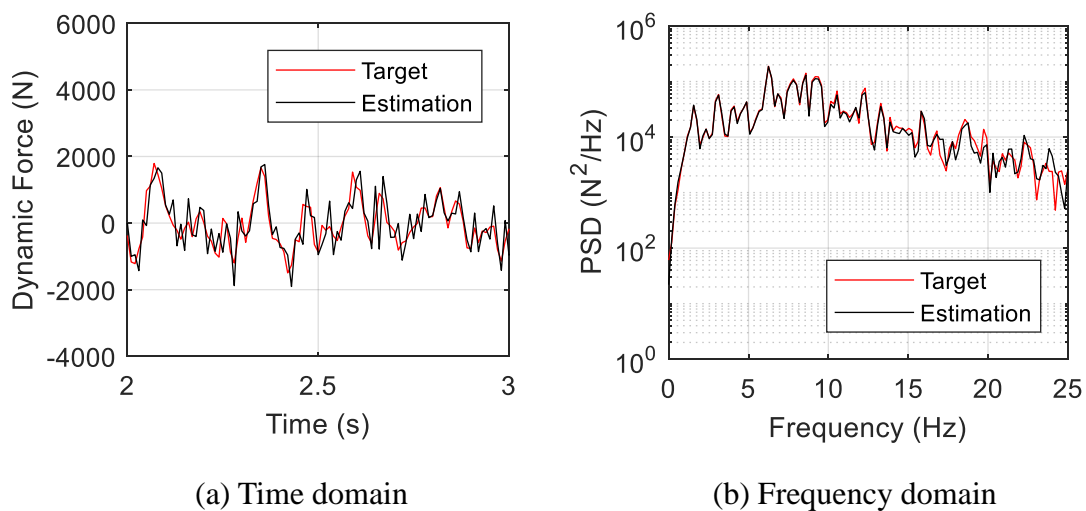
Fig. 3-8. Estimation with noise and error for Case 1

(a) Time domain   (b) Frequency domain
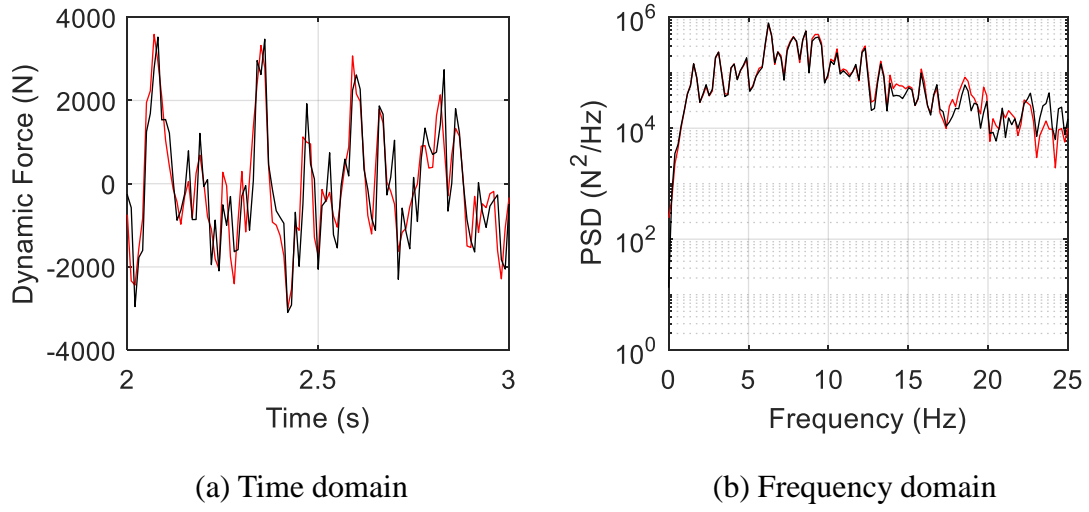
Fig. 3-9. Estimation with noise and error for Case 2

(a) Time domain   (b) Frequency domain
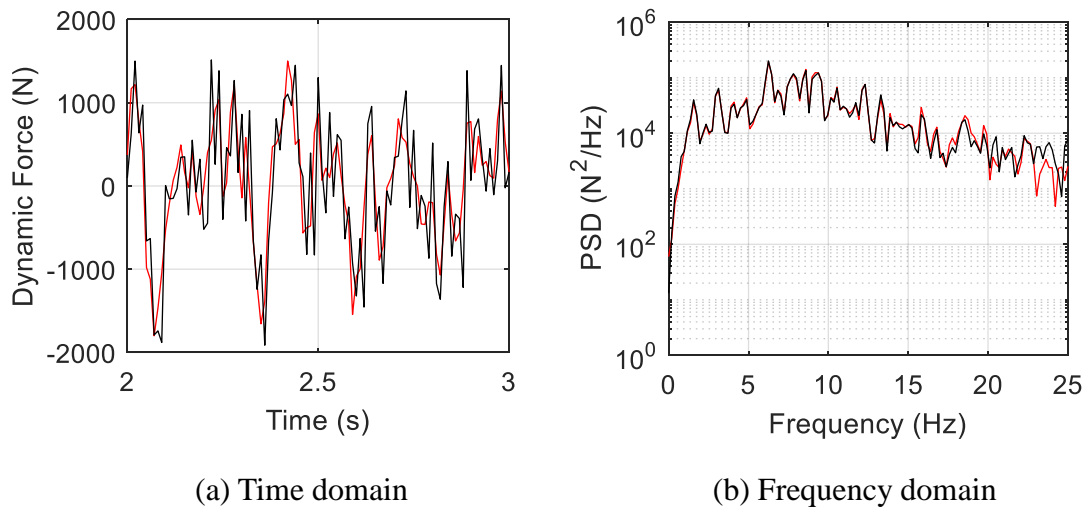
Fig. 3-10. Estimation with noise and error for Case 3

The accuracy of the tire force estimation is quantified by an error index ε, defined as the ratio of the norm of the difference between the true force and the estimated force to the norm of the true force as expressed by Eq. (3-22)

$$\varepsilon = \frac{\left\| F_{true} - F_{es} \right\|}{\left\| F_{true} \right\|} \times 100\% \tag{3-22}$$

where F_{true} is the simulated real force and F_{es} denotes the estimated force. The errors for each case with and without noises are listed in Table 3-5. It is observed that the errors with the influence from noise are only slightly higher than the errors without noise, indicating that the proposed method is robust against sensor noises.

Table 3-5. Estimation errors of each case

	Case	Left estimation	Right estimation	Total estimation
1	Without noise	20.12 %	20.04 %	20.05 %
	With noise	21.02 %	21.48 %	20.84 %
2	Without noise	70.15 %	33.90 %	20.48 %
	With noise	71.22 %	34.67 %	21.23 %
3	Without noise	130.33 %	46.61 %	20.34 %
	With noise	130.50 %	46.68 %	21.74 %

3.2.4 Sensitivity Analysis on Sensor Placement

In this study, each tire force is estimated using the vehicle body responses at the location above the corresponding tire. The reason for not choosing responses of other locations is discussed in the sensitivity analysis below following the method of Lu and Law (2007).

For a dynamic system, the general equation of motion is expressed as

$$\mathbf{M}\ddot{\mathbf{q}}(t) + \mathbf{C}\dot{\mathbf{q}}(t) + \mathbf{K}\mathbf{q}(t) = \mathbf{L} \cdot \mathbf{F}_P(t) \qquad (3\text{-}23)$$

where $\mathbf{M}$, $\mathbf{C}$, and $\mathbf{K}$ are the mass, damping, and stiffness matrix, $\mathbf{q}$ is the responses vector, $\mathbf{L}$ is the vector mapping the system input to each of the degree-of-freedom, and $\mathbf{F}_P$ is the

system input described by a series of Fourier harmonics, as

$$\mathbf{F}_P(t) = \sum_{n=1}^{N} A_n F_n(t) \tag{3-24}$$

in which A_n is the nth Fourier amplitude and $F_n(t)$ is the corresponding Fourier harmonics with a frequency of f_n.

By differentiating both sides of Eq. (3-25) with respect to the nth Fourier amplitude, the equation of motion becomes

$$\mathbf{M}\frac{\partial \ddot{\mathbf{q}}(t)}{\partial A_n} + \mathbf{C}\frac{\partial \dot{\mathbf{q}}(t)}{\partial A_n} + \mathbf{K}\frac{\partial \mathbf{q}(t)}{\partial A_n} = \mathbf{L} \cdot F_n(t) \tag{3-25}$$

where the derivative terms on the left-hand side indicate the sensitivity of the acceleration, velocity, and acceleration responses to the perturbation of the input force at frequency f_n.

The sensitivity of the vehicle body accelerations at four locations to the front left tire force are obtained as a frequency function. Eq. (3-25) is an equation of motion with a harmonic excitation force. The solution of the equation, which is the sensitivity of the displacement, is obtained as steady-state response. The sensitivities of the acceleration and velocity are obtained as the first and second-order derivatives. Note that these sensitivities are time histories. Therefore, the maximum value of each sensitivity time history is adopted as a sensitivity index for the purpose of comparison.

The sensitivity indices of the acceleration at each sensor location to the front left force are shown as a function of frequency in Fig. 3-11.
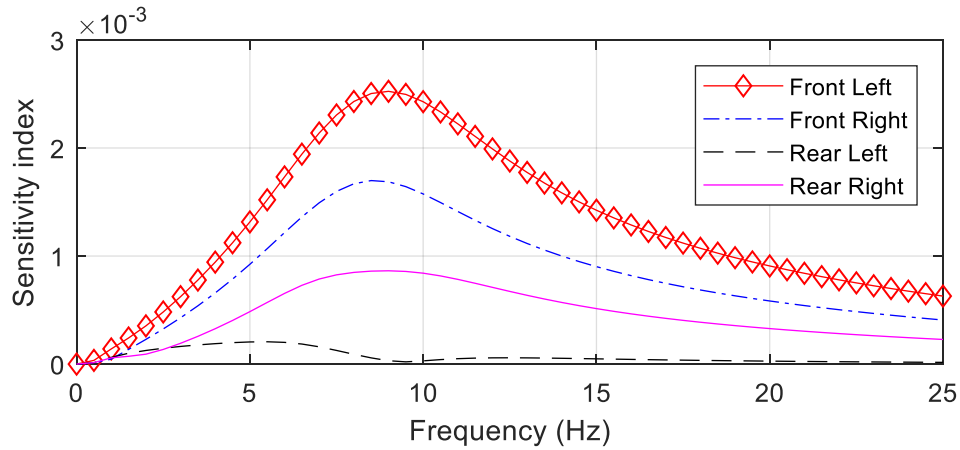
Fig. 3-11. Sensitivity index of acceleration at each sensor to front left tire force

The figure shows that the front left acceleration has the highest sensitivity to the front left tire force. Similar analyses on other tire forces also indicate that the highest acceleration sensitivity to a tire force is at the sensor location above the collocated tire. Also, the sensitivities of front side accelerations to the front tire forces are higher than those of rear side accelerations. Those of rear side accelerations to the rear tire forces are higher than those of front side accelerations. With the half-car model, the front tire forces should thus be estimated from the sensors above front tires while the rear tire forces should be estimated from the sensors above rear tires. Thus, the simulation configuration in Section 3.2.3 is supported.

3.3 Bridge Modal Mass Identification

After verifying the tire force estimation algorithm, the sensor-equipped vehicle can be used to run over a bridge while estimating the tire forces. Accelerometers should also be placed on the bridge to measure bridge acceleration responses induced by this passing vehicle. In this way, both the excitation force and the corresponding responses are

obtained, making it possible to extract the bridge modal mass values.

3.3.1 Implementation of Genetic Algorithm

In section 2, the equation of motion of the bridge system is decomposed as a series of equations, each of which represents one single-degree-of-freedom system corresponding to one specific mode.

$$M_n \ddot{q}_n(t) + C_n \dot{q}_n(t) + K_n q_n(t) = P_n(t) \tag{3-26}$$

where M_n, C_n, K_n, and P_n are the modal mass, damping, stiffness, and modal load of the nth mode, respectively, and q is the modal coordinate which is related with the bridge displacement responses through:

$$y(t) = \sum_n W_n q_n(t) \tag{3-27}$$

where W_n is the nth mode shape.

The relations between M_n, C_n, and K_n are shown as:

$$C_n = 2\xi_n \omega_n M_n, K_n = M_n \omega_n^2 \tag{3-28}$$

where ξ_n and ω_n is the damping ratio and natural frequency of the nth mode, respectively. Note that the damping ratio, natural frequency, and mode shape are considered as known values because they can be obtained by implementing output-only structural health monitoring technique.

The meanings of the physical quantities above are summarized in Table 3-6.

Table 3-6. Physical meanings of each quantity in bridge system

Name	Meaning	Notes
P_n	n^{th} modal load	Estimated from vehicle responses
ω_n	n^{th} natural frequency	Extracted from SHM technique
ξ_n	n^{th} damping ratio	Extracted from SHM technique
W_n	n^{th} mode shape	Extracted from SHM technique
$y(t)$	Bridge responses	Measured by sensors
M_n	n^{th} modal mass	Unknown

From Table 3-6, once the vehicle tire force is estimated from vehicle responses and other bridge parameters also obtained from SHM techniques, the only unknown variables of the bridge system are the modal mass values of each mode. Therefore, only the modal mass values are optimized through the iterations of the genetic algorithm.

In the genetic algorithm conducted in this study, the initial individuals are composed of different initial combinations of modal mass values of each mode. The modal damping and modal stiffness can thus be calculated through Eq. (3-28) for each individual. The tire forces estimated from Section 3.2 are used as the input of bridge system to calculate the bridge responses under the bridge parameters of each individual. The measured responses are then used to evaluate the fitness of each individual through the target function of Eq. (3-29).

$$R = \sum_i \int_0^T \left| \ddot{y}_{pre,i}(t) - \ddot{y}_{mea,i}(t) \right| \mathrm{d}t \qquad (3\text{-}29)$$

where the subscript 'pre' and 'mea' indicates 'predicted' and 'measured', respectively, T is the period of the vehicle's passage and the subscript 'i' stands for the ith location of the

sensors.

The individuals that have higher fitness will have higher chances to be chosen in the next generation. The iterations of the genetic algorithm continue following the procedure of selection, crossover, and mutation described in Section 1.6.3, until the termination condition is met.

3.3.2 Numerical Verification and Error Analysis

In this section, a numerical example is given to verify the implementation of genetic algorithm, followed by an error analysis to discuss the effects of sensor noise and the estimation error in tire forces.

In this numerical example, a two-lane slab model is adopted as the bridge model, where a vehicle is simulated to pass across the bridge as the exciter of the bridge vibration. Bridge acceleration responses at 1/4 span, mid-span, and 3/4 span are calculated as the 'measured' responses. The natural frequencies, damping ratios, and the corresponding mode shapes are extracted from Yokohama Bridge, whose details are described in Section 2.3.3. The bridge deck roughness is determined as the same as the one used for Section 3.2.3.

In the simulation, the bridge total physical mass is set as 300 ton, assumed to be equally distributed on the bridge deck. The modal mass values are then calculated based on the following equation.

67

$$M_n = \iint\limits_{Area} \bar{m} \cdot W_n^2 \mathrm{d}x\mathrm{d}y \qquad (3\text{-}30)$$

where $\bar{m}$ corresponds to the physical mass per area of the bridge. In this numerical example, calculated as 747.2 kg/m². The modal mass of each mode is listed in Table 3-7. The initial range in genetic algorithm is set as $0.2 - 5$ times of the correct values.

Table 3-7. Modal mass values used in simulation

No. of Mode	1	2	3	4
Modal mass	140.96 ton	125.62 ton	87.97 ton	152.75 ton

To check the correctness of the algorithm, sensor noise is not included and the vehicle tire force estimated from the vehicle responses is considered to be accurate. Genetic algorithm iterations are conducted to give the estimation results of the modal mass values of each mode shape, as shown in Fig. 3-12 (a) – (d). The number of individuals used here is 500 and 10 % of individuals are deleted at each iteration step.
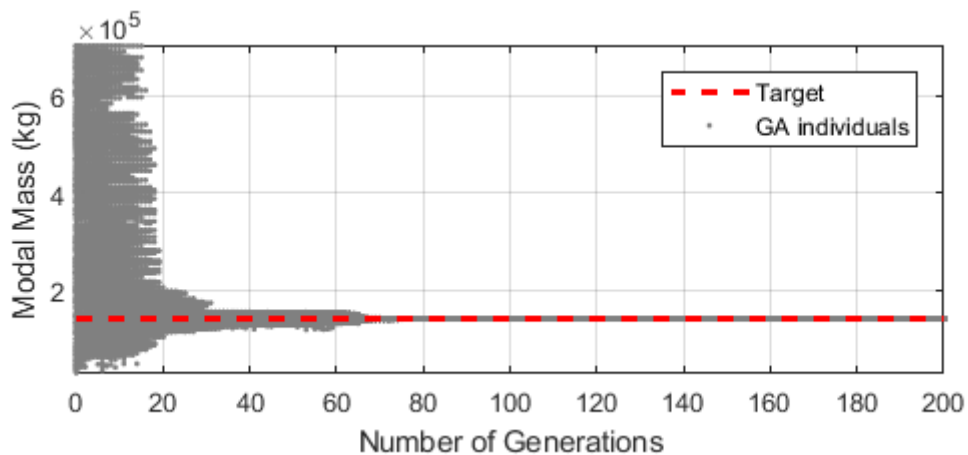
(a) First mode
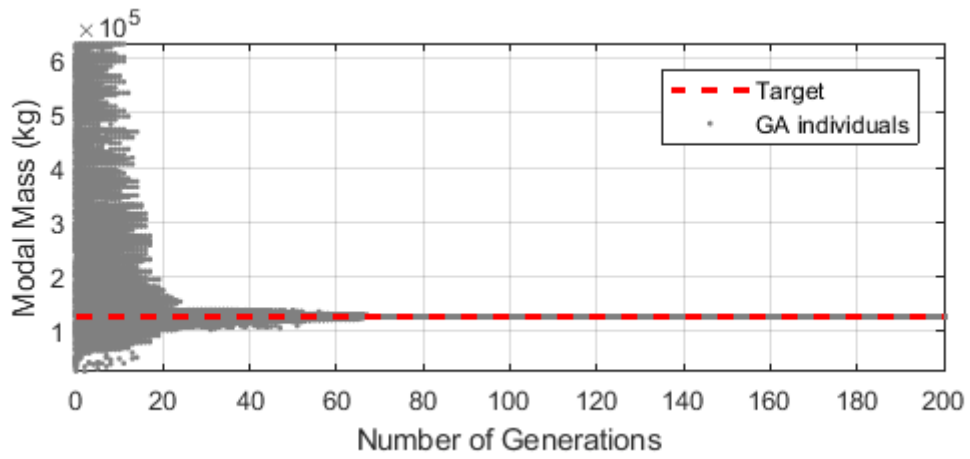
(b) Second mode
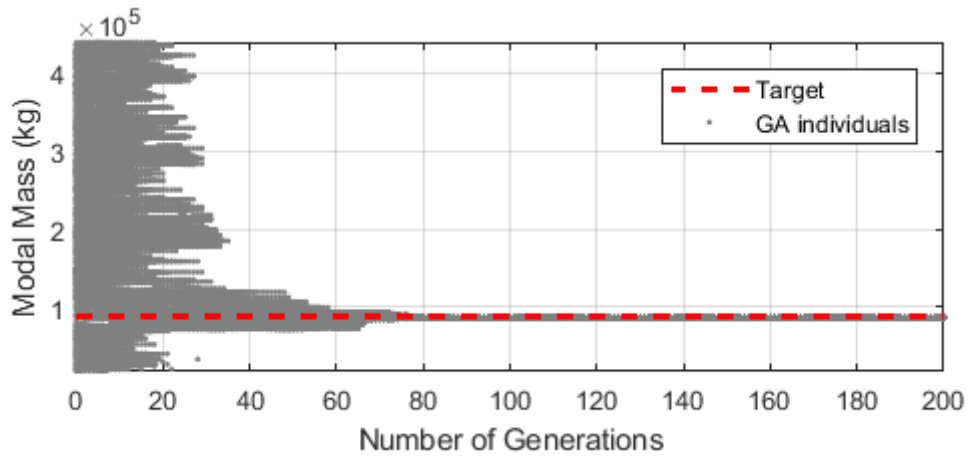
(c) Third mode
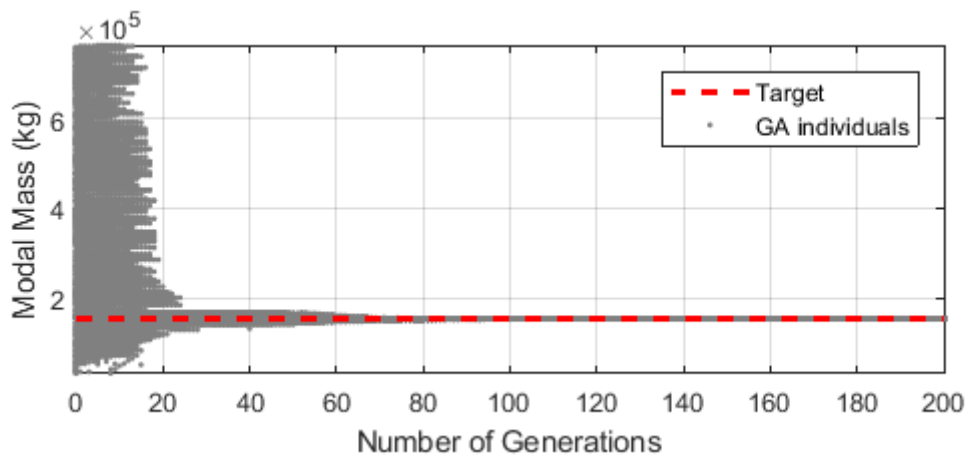
(d) Fourth mode

Fig. 3-12. Modal mass identification results without noise

After a few generations, all modal mass values converge to the target with a good accuracy. The errors defined from Eq. (3-31) are calculated and listed in Table 3-8. Also, the target function value of each generation step is shown in Fig. 3-13 to check the convergence of the algorithm.

$$error = \left| \frac{M_{n,real} - M_{n,estimated}}{M_{n,real}} \right| \times 100\% \qquad (3-31)$$

Table 3-8. Modal mass identification error without noise

Mode	First	Second	Third	Fourth
Error	0.05 %	0.02 %	0.01 %	0.02 %
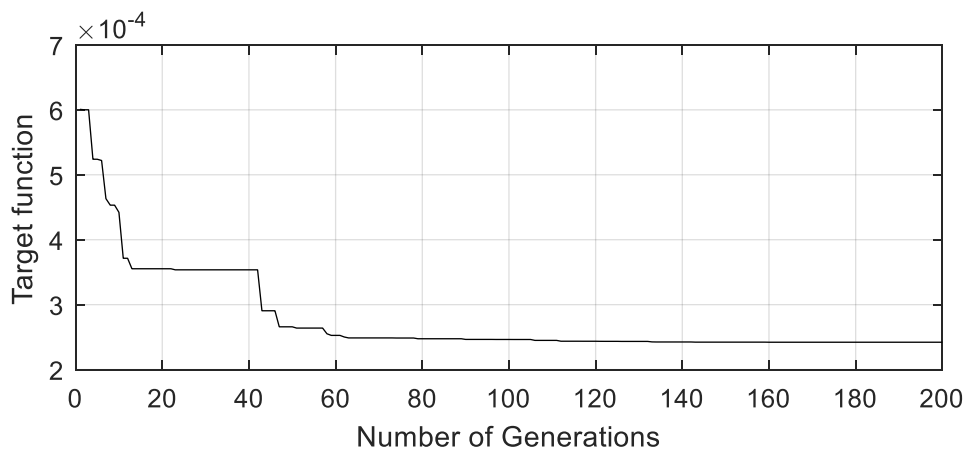
Fig. 3-13. Target function of each generation step without noise

An error analysis is conducted to check the robustness against noise. In this case, mainly two sources of errors are unavoidable, including sensor noise on bridge acceleration measurement, and the estimation error of vehicle dynamic tire forces.

For the sensor noise of bridge acceleration measurement, 10 % of noise is added following

the same manner as described in Eq. (3-21). To account for the possible error of tire force estimation, the results shown in Fig. 3-10, where vehicle sensor noise and calibration errors are considered, are used for the input of this simulation. The results with these errors are shown in Fig. 3-14.
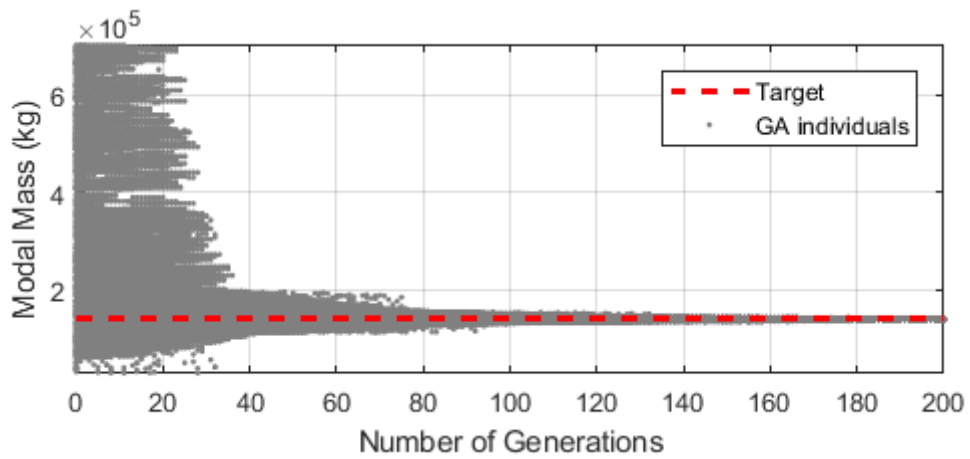
(a) First mode
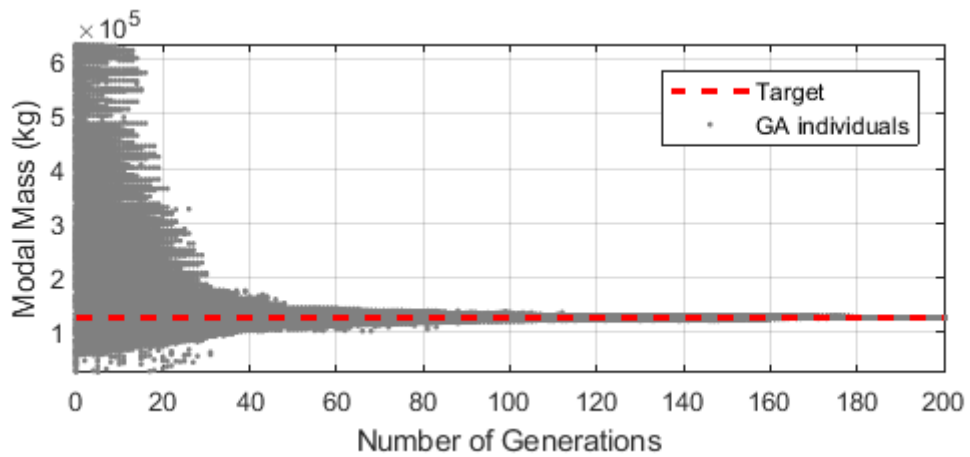
(b) Second mode
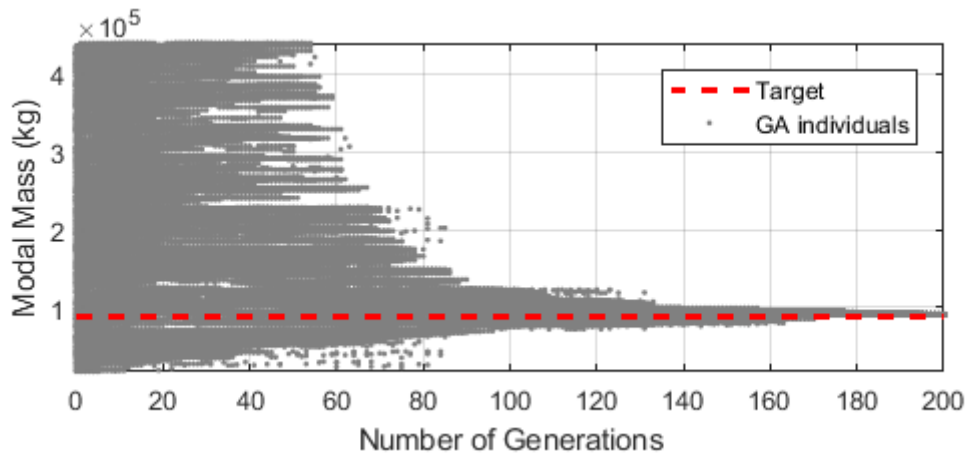
(c) Third mode
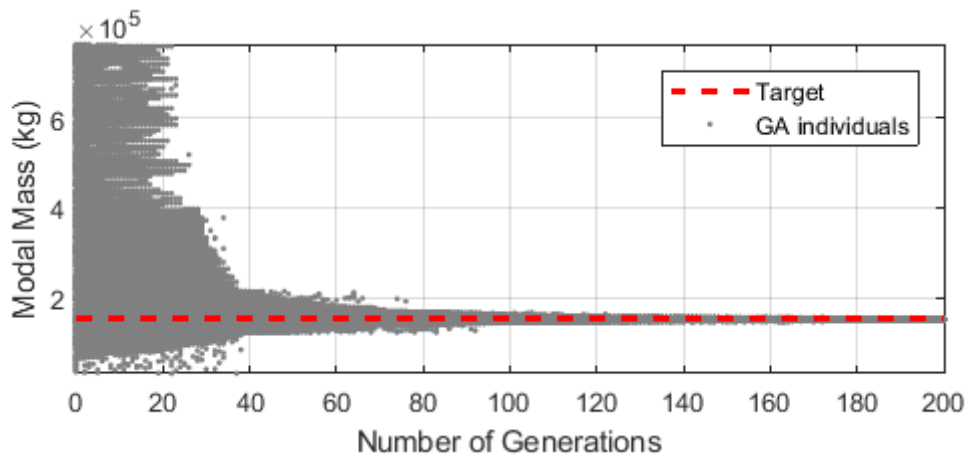
(d) Fourth mode

Fig. 3-14. Modal mass identification results with noise

Compared with the results shown in Fig. 3-12, it is noticed that the modal mass values need more generations to converge due to the existence of sensor noise and errors. The estimation errors in Fig. 3-14 are listed in Table 3-9. Note that these error values will be different for each run of the algorithm because GA is a stochastic parameter identification algorithm. The target function value of each generation step is also shown in Fig. 3-15.
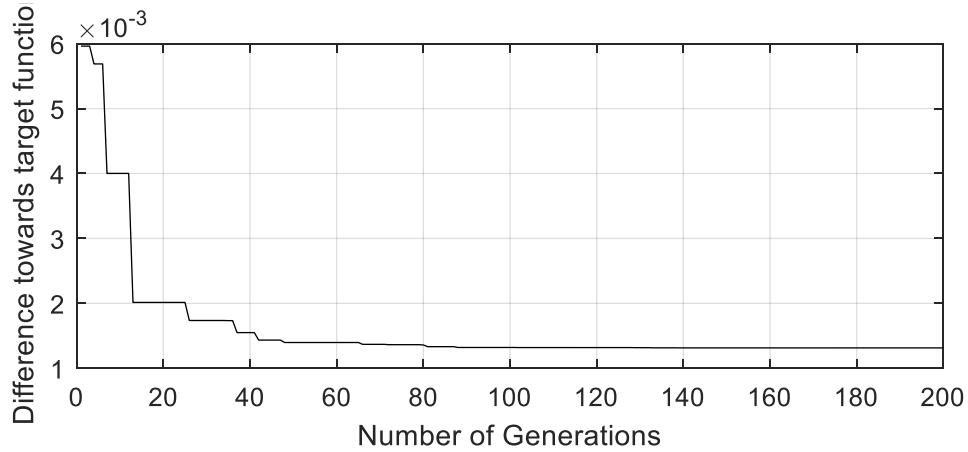
Fig. 3-15. Target function of each generation step with noise

Table 3-9. Modal mass identification error with sensor noise

Mode	First	Second	Third	Fourth
Error	1.01 %	1.31 %	0.51 %	0.88 %

3.4 Experimental Validation

In this section, the algorithms of vehicle dynamic tire force estimation and bridge modal mass identification are validated through field measurement. The tire force estimation algorithm is first validated in an experiment conducted on the campus of The University of Tokyo, Japan. With the vehicle dynamic tire force estimation algorithm being validated, one bridge is used to test the bridge modal mass identification algorithm.

3.4.1 Tire Force Estimation on Campus

In this section, an experiment was conducted to validate the proposed algorithm for the estimation of dynamic tire forces from measured vehicle responses. A Honda Step-wagon van was equipped with a SLW-20KNC wheel-load transducer (Tokyo Sokki Kenkyujo)

73

at the front left tire, which can record the contact force between the tire and the ground. Four iPod touch sensors equipped with accelerometers and gyros were attached on the vehicle body just above each vehicle tire to measure vertical acceleration and angular velocity. The iPod data was synchronized with the wheel-load transducer through an ARS-10A accelerometer attached next to the iPod sensor, sharing the same time system with the wheel-load transducer. The sampling frequencies of all devices were set at 100 Hz. In addition, a GPS sensor was attached to the iPod sensor to determine the vehicle driving speed at every second.

(a) Test vehicle (Honda Corporation) (b) wheel-load transducer (Tokyo Sokki)

(c) Sensors on vehicle body

Fig. 3-16. Experimental setup of for dynamic tire force estimation

As stated before, the vehicle parameters are necessary for the tire force estimation. A calibration test, in which a known-size hump was used as the input when the test vehicle drove over the hump, was conducted to obtain the half-car model parameters of the test vehicle. The hump is shown in Fig. 3-17 while the calibrated vehicle parameters are listed in Table 3-10.

Fig. 3-17. Portable humps for vehicle parameter calibration

Table 3-10. Vehicle parameters calibrated from hump test

m_b(kg)	m_f(kg)	I_y(kg/m^2)	k_f(N/m)	k_r(N/m)
1263	143.7	393.3	61088	69297
c_f(Ns/m)	c_r(Ns/m)	k_{tf}(N/m)	k_{tr}(N/m)	L_f(m)
1965.6	3736.7	517380	990850	1.87

The test vehicle was driven at various speeds on a road on the campus of The University of Tokyo. Data of around 16 minutes was obtained. The vertical acceleration, angular velocity, and driving speed are shown in Fig. 3-18 (a), (b), and (c), respectively. Reference acceleration records given by ARS-10A accelerometer is also shown.
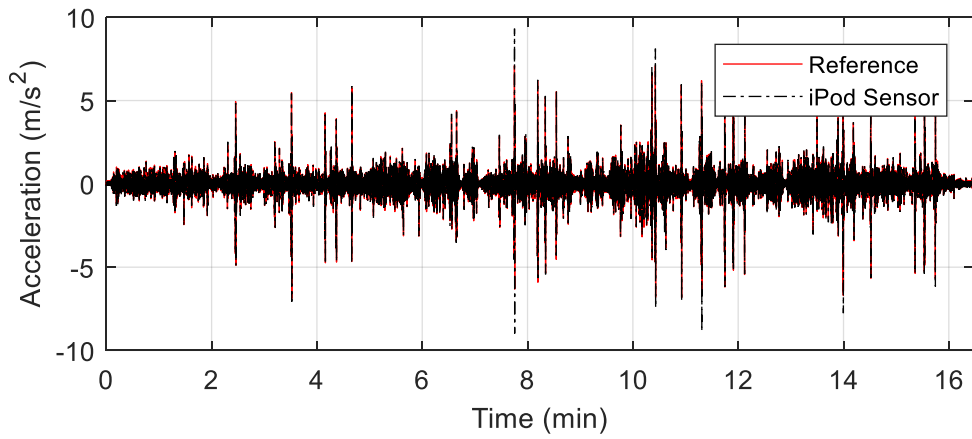
(a) Vehicle body vertical acceleration (measured above front left tire)
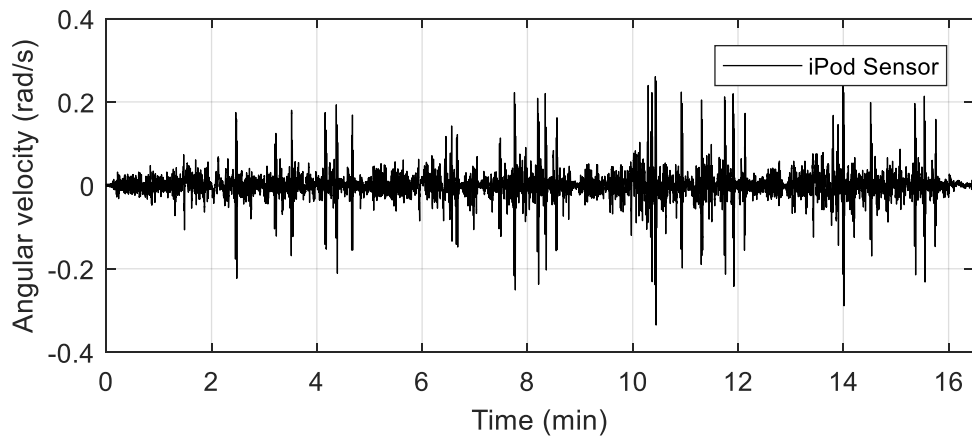
(b) Vehicle body angular velocity (measured above front left tire)
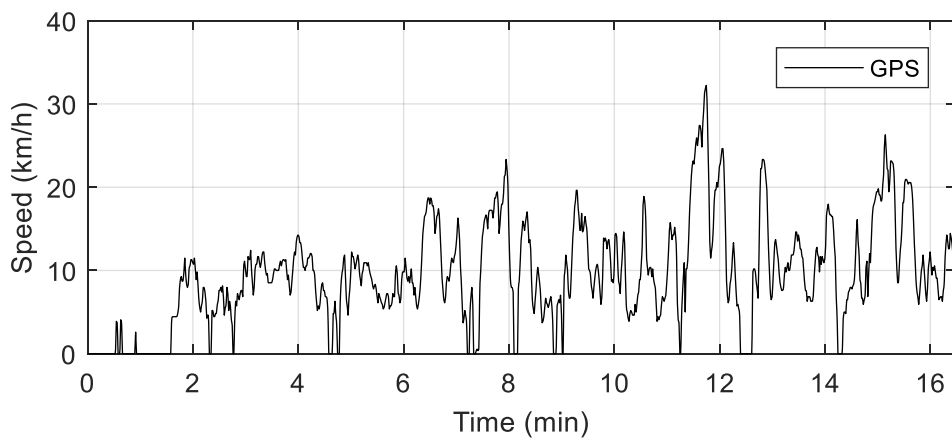
(c) Vehicle driving speed

Fig. 3-18. Measured vehicle responses

Following the process described above, the tire force was estimated from the measured data. The result is shown in Fig. 3-19 (a) and (b) in the time domain and the frequency domain, respectively, together with the reference force recorded from the wheel-load transducer. Good accuracy is observed in the time domain, while in the frequency domain, the components within 1 – 4 Hz coincide well with the load cell signal.
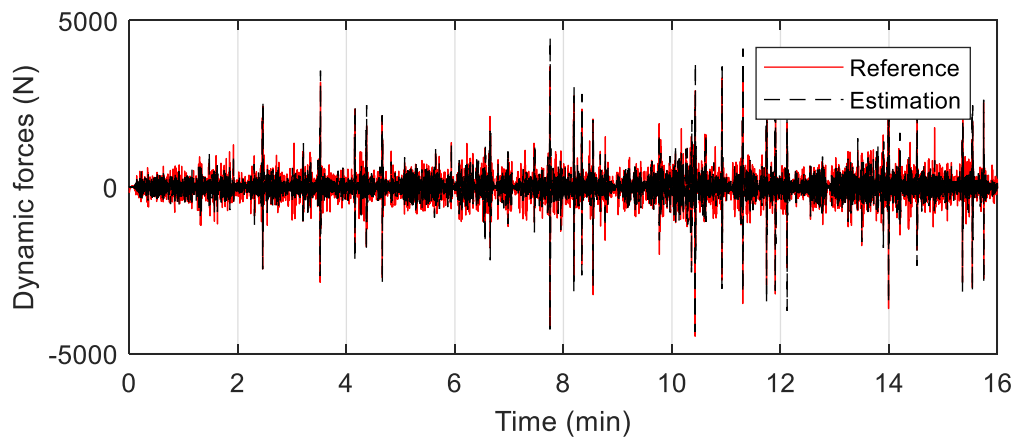
(a) Estimation results in the time domain
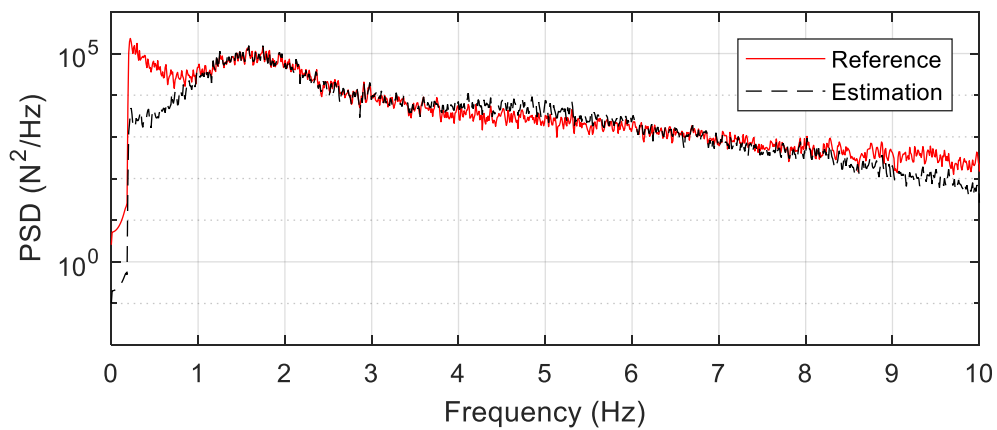
(b) Estimation results in the frequency domain

Fig. 3-19. Estimation results of dynamic tire force

Because the driving speed and the road roughness fluctuate, the results of four sections are extracted from the signal estimation and are shown in Fig. 3-20 (a) – (d), in which (a)

– (c) correspond to the driving speeds around 10, 20, and 30 km/h, while (d) shows the tire force estimation when the vehicle passed over a hump on the road. These figures indicate that the proposed algorithm is robust against driving speed difference in the range (Fig. 3-20(a) – (c)) and has good performance even when the road condition suddenly changes (Fig. 3-20(d)). The error of each case following the definition of Eq. (3-22) is calculated and listed in Table 3-11. The possible reasons of these errors include:

(1) Sensor noises and half-car modelling errors reduce the accuracy of the method.

(2) The linear half-car model, even when well calibrated, may not fully reflect the dynamic properties of the real vehicle due to more complex mechanical components and some other non-linear parts.

(3) The reference force was recorded only at the front left tire. Although the effect of the vehicle rolling motion may be small, this effect is not considered in this experiment.
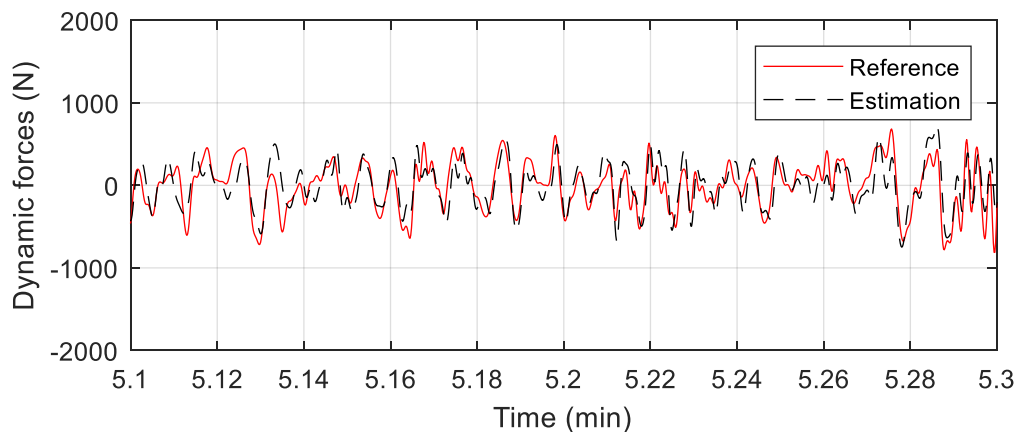
(a) Around 10 km/h
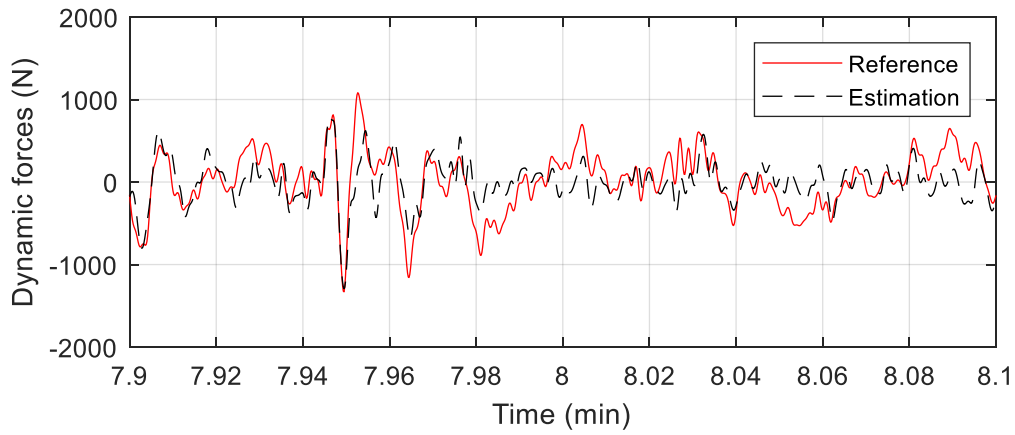
(b) Around 20 km/h
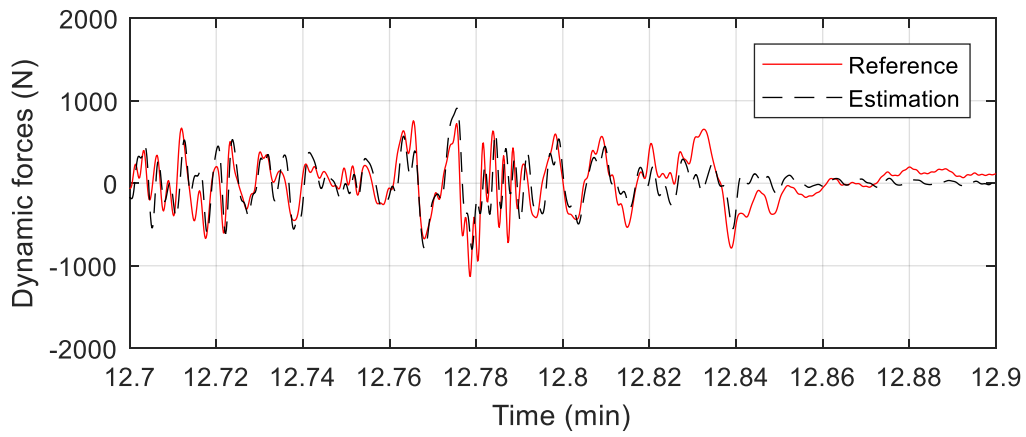
(c) Around 30 km/h
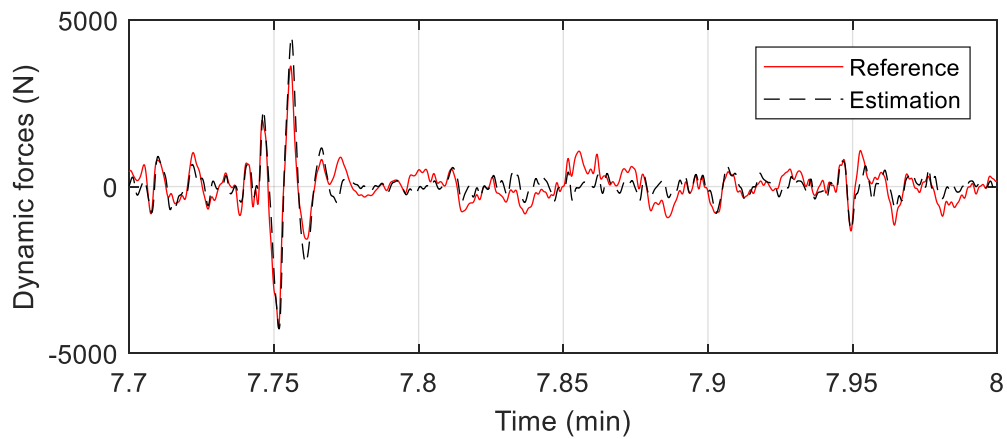
(d) Vehicle passing over a hump

Fig. 3-20. Estimation for different driving speeds and road conditions

Table 3-11. Tire force estimation error under different driving speeds and road conditions

Case	10 km/h	20 km/h	30 km/h	Hump
Error (%)	44.57	55.84	56.42	29.59

3.4.2 Bridge Modal Mass Identification on Tsukige Bridge

To validate the modal mass identification method using the genetic algorithm, a field measurement was conducted at Tsukige Bridge. Description of this bridge and its dynamic properties are shown in Section 2.3.1. A Toyota hi-ace van (Toyota Corporation) shown in Fig. 3-21 is adopted as the test vehicle to excite the bridge.

Fig. 3-21. Test vehicle (Toyota Corporation) on Tsukige Bridge

The purpose of this field measurement is to estimate bridge modal mass values from estimated vehicle dynamic tire forces and the bridge responses. To estimate tire forces, sensors were equipped on the vehicle body in the same way as described in Section 3.4.1. The sensor on the vehicle are shown in Fig. 3-22.

Fig. 3-22. Sensors on the test vehicle

The iPod sensor shown in Fig. 3-22 is used for vehicle body acceleration and angular velocity measurement. A GPS device was attached to the iPod sensor to provide vehicle speed information at a sampling rate of 1 Hz. The JAE sensor connected to GPS to obtain the time stamp was installed next to the iPod sensor for the purpose of synchronization between vehicle responses and bridge responses.

The test vehicle was driven across the bridge to provide excitation source. Based on the vehicle tire force identification algorithm, the front and rear tire forces of the vehicle were estimated from sensors on the vehicle and are shown in Fig. 3-23 and Fig. 3-24, respectively. These forces are used as the known input to the bridge for the modal mass identification problem.
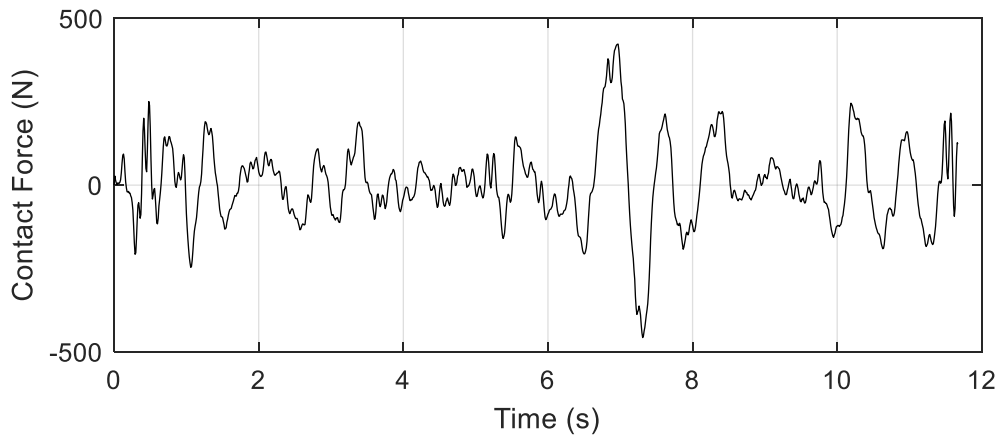
Fig. 3-23. Estimation of front dynamic tire force from vehicle responses
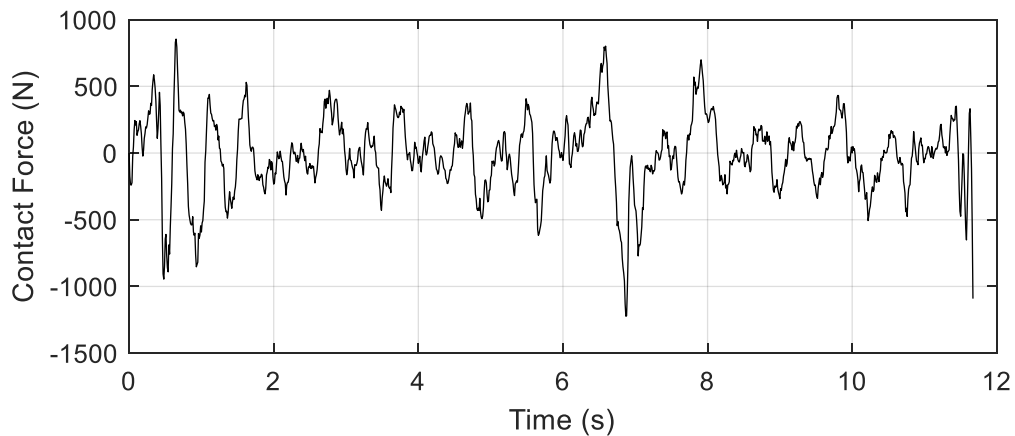
Fig. 3-24. Estimation of rear dynamic tire force from vehicle responses

To measure the bridge responses, accelerometers were attached on the bridge. Fig. 3-25 shows the adopted wireless accelerometer. Although many accelerometers are used for bridge dynamic property extraction as shown in Fig. 2-8, the responses at bridge mid-span, 1/4-span, and 3/4-span are used in the genetic algorithm.

Fig. 3-25. Sensor on Tsukige bridge (Sonas Corporation and JAE Corporation)

A typical time history of bridge mid-span acceleration responses of one vehicle passage is shown in Fig. 3-26. These sensors on the bridge were synchronized to wireless sensors on the bridge by developing acceleration measurement systems equipped with GPS and installing them both on the vehicle and on the bridge. The mid-span responses are used together with the 1/4-span and 3/4 span responses as the target function in genetic algorithm. The bridge modal mass values are estimated with the converging process shown in Fig. 3-25 (a) – (c) for each mode, respectively.
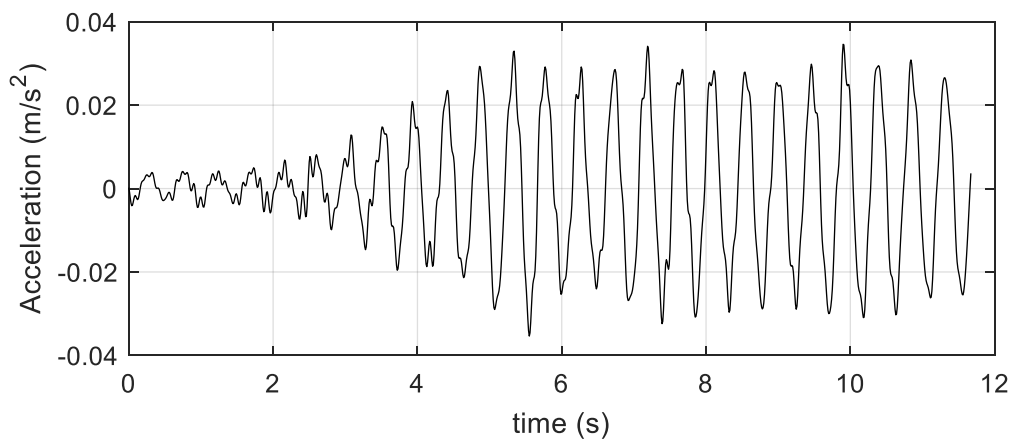
Fig. 3-26. Bridge mid-span acceleration responses under one vehicle passage
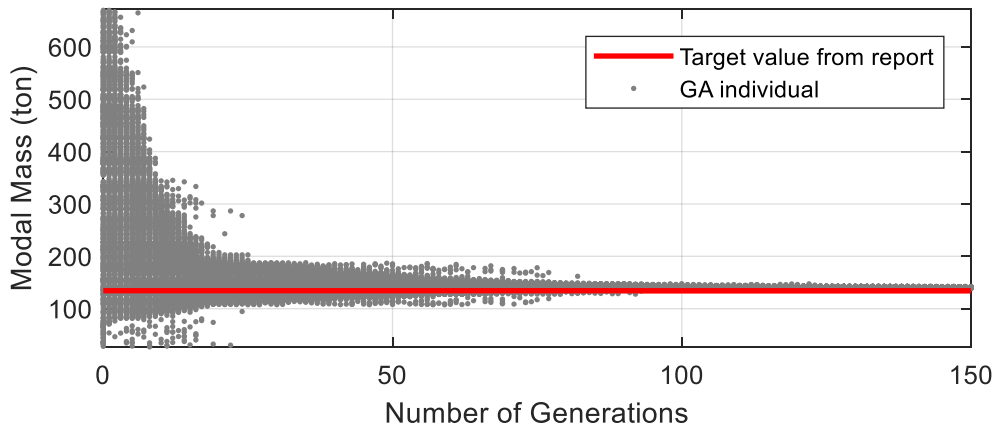
(a) Converging process of the first mode
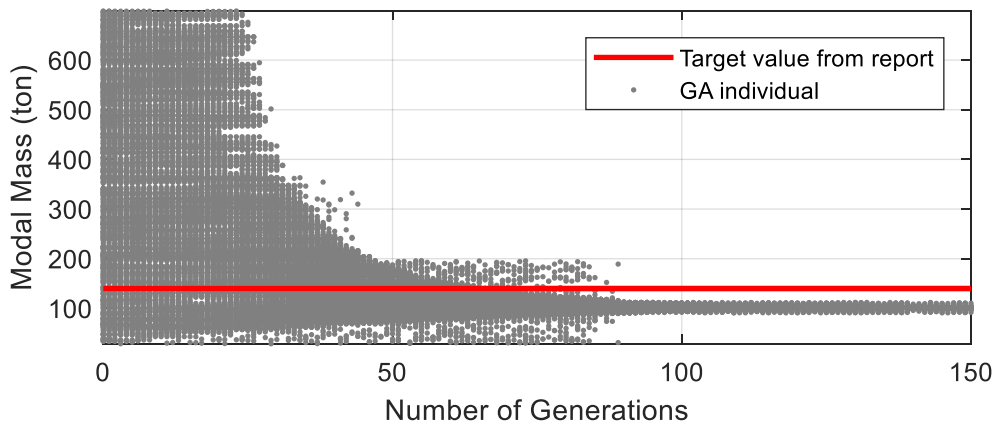
(b) Converging process of the second mode
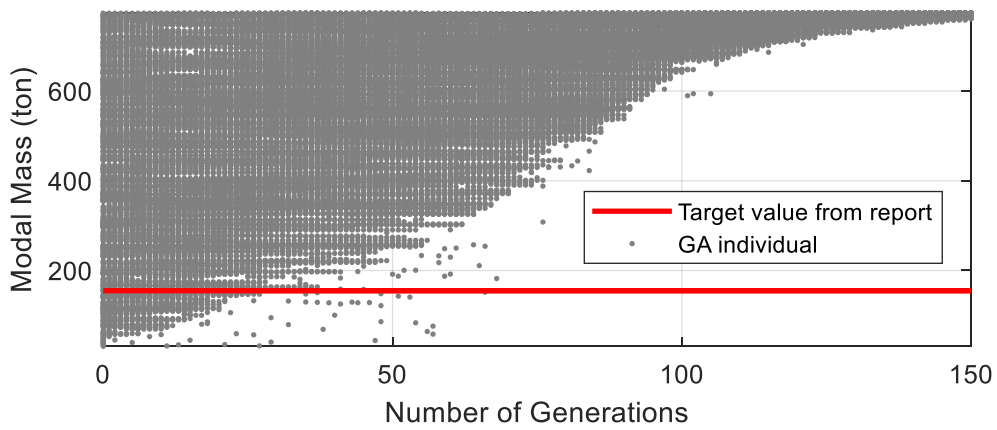
(c) Converging process of the third mode

Fig. 3-27. Converging process of modal mass value of each mode

From Fig. 3-27, the modal mass value of the first mode is estimated with an error of 4.80 %. The second modal mass value has an error of 15.75 %. This is possibly due to the vehicle dynamic tire force error. For the third mode, the modal mass value does not converge with all the individual values much higher than the target value. This phenomenon can be explained by the tire force estimation result in the frequency domain shown in Fig. 3-19, where the high frequency range is shown to have much lower amplitudes with higher inaccuracy.

As discussed above, the modal mass values of high order modes are identified with a poorer accuracy due to the error of the vehicle dynamic tire force estimation in the first step. Therefore, those mass values corresponding to higher modes are calculated from Eq. (3-30), in which the mass per length is calculated by the estimated modal mass value of the first mode using the same formula. The adopted estimation of modal mass values is listed in Table 3-12, where the target values are calculated from the physical mass and the normalized mode shapes.

Table 3-12. Estimation of modal mass values

No. of mode	1	2	3
Target value	134.35 ton	139.92 ton	154.89 ton
Estimated value	140.76 ton	146.60 ton	162.28 ton
Error	4.80 %		

In the field measurement, the above procedure was repeated for several times at different driving speeds. For each driving speed, i.e., 20, 30, 40, and 50 km/h, three tests were

conducted. The estimation value of the first modal mass and the corresponding estimation error are listed in Table 3-13.

Table 3-13. Estimation result and error of first modal mass value

Vehicle Speed		20 km/h	30 km/h	40 km/h	50 km/h
Test 1	Value	127.90 ton	122.87 ton	129.78 ton	135.79 ton
	Error	-4.80 %	-8.54 %	-3.40 %	1.07 %
Test 2	Value	137.15 ton	131.18 ton	139.41 ton	147.77 ton
	Error	2.09 %	-2.36 %	3.77 %	9.99 %
Test 3	Value	132.61 ton	151.19 ton	125.20	135.55 ton
	Error	-1.29 %	12.54 %	-6.81 %	0.90 %

It is shown in Table 3-13 that the proposed modal mass identification method is robust against driving speed with a good repeatability. Moreover, from these tests, the dependency on the vehicle driving speed is not found. The largest estimation error, 12.54 %, occurs at the third test of 30 km/h tests. Note that for each test, the estimation error is not a deterministic value due to the stochastic nature of the genetic algorithm. The errors, as well as the estimated values, are also affected by the values of the randomly generated individuals during each generation of the genetic algorithm. The proposed method exhibits good accuracy with the largest error (12.54 %) when estimating bridge modal mass value.

3.5 Summary

In this chapter, a two-step method for bridge modal mass identification is proposed. The

vehicle dynamic tire forces are first estimated through the measurement of vehicle body acceleration and angular velocity, whose feasibility is proved by an observability analysis. In the second step, the sensor-equipped vehicle is driven to pass across a bridge as the excitation source. The vehicle dynamic tire forces are estimated following the algorithm in step 1, while the bridge acceleration responses are measured simultaneously. With the estimated input and the measured output, the bridge modal mass values are optimized using a genetic algorithm. Both tire force estimation and modal mass identification are verified by numerical example and validated by field measurement.

Chapter 4 Bridge Pavement Roughness Estimation from Measurement on Vehicle Responses with Consideration of Vehicle-Bridge Interaction

4.1 Overview

Bridge pavement roughness, i.e., the longitudinal profile of bridge pavement, has an important role in the vehicle-bridge dynamics, because it acts as the only excitation source of the vehicle-bridge coupling system. When a vehicle crosses the bridge, the bridge pavement roughness causes vehicle vibration, which, in turn, leads to bridge vibration. Therefore, an accurate estimate of the pavement roughness is of great importance. However, as stated in Chapter 1, most existing methods cannot deal with the influence from bridge vibration, which will lead to a certain degree of inaccuracy.

In this chapter, the pavement roughness of the target bridge is estimated using a probe car with calibrated parameters. As the output of the vehicle-bridge coupled system, vehicle responses are measured through sensors installed on the probe car. The system input, i.e., the pavement roughness, is estimated through an inverse analysis.

The structure of this chapter is arranged as follows. Section 4.1 gives an overview of the chapter. Section 4.2 describes the process of the implementation of particle filter on bridge pavement roughness estimation problem considering vehicle-bridge interaction.

Numerical example is given in Section 4.3 to verify the proposed algorithm with error analysis on the influence from sensor noise and driving speed. Section 4.4 gives an experimental validation conducted at Tsukige Bridge, where the estimation from the proposed algorithm is examined by the reference data given by a portable profiler, i.e., a hand cart equipped with inertia sensors to accurately measure the profile. Finally, a summary is provided in Section 4.5.

4.2 Implementation of Particle Filter on Bridge Pavement Roughness Estimation with Vehicle-Bridge Interaction

When a vehicle passes over a bridge, the pavement roughness and bridge vibration are the main sources of vertical excitation. Through vehicle-bridge interaction, the vehicle responses are affected by the pavement roughness as well as the bridge vibration.

In this chapter, a two-axle vehicle passing over a bridge is considered, as shown in Fig. 4-1. The pavement roughness at the front and rear tires is defined as $r_f(t)$ and $r_r(t)$, respectively, while the bridge deflection under each tire is $y_f(t)$ and $y_r(t)$. The total excitation inputs to the vehicle are expressed as the summation of pavement roughness and bridge deflection, as shown in Eq. (4-1).
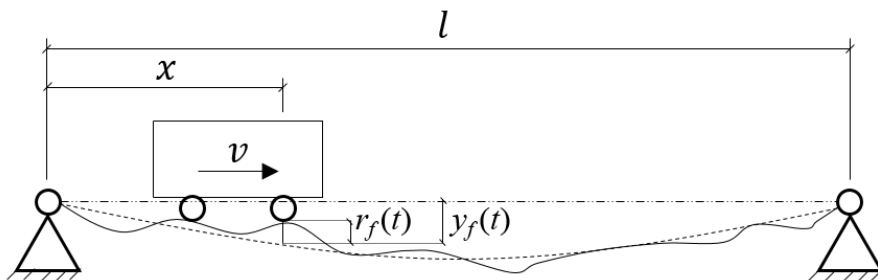
Fig. 4-1. Vehicle passing over a bridge with bridge vibration

90

$$h_f(t) = r_f(t) + y_f(t)$$
$$h_r(t) = r_r(t) + y_r(t)$$
(4-1)

The equation of motion of the vehicle system, which has been described in previous sections, is rewritten here for the convenience.

$$\mathbf{M}_v\ddot{\mathbf{U}}(t) + \mathbf{C}_v\dot{\mathbf{U}}(t) + \mathbf{K}_v\mathbf{U}(t) = \mathbf{P}(t)$$
(4-2)

where

$$\mathbf{U} = \begin{bmatrix} u_b & \theta & u_f & u_r \end{bmatrix}^{\mathbf{T}}, \mathbf{P} = \begin{bmatrix} 0 & 0 & h_f k_{tf} & h_r k_{tr} \end{bmatrix}^{\mathbf{T}}$$
(4-3)

Vehicle responses, including vehicle body acceleration and the angular velocity, are measured considering the practical sensor installation situation. For the implementation of the particle filter, the unknown pavement roughness is included in the evolution process of the system state to formulate an augmented state vector, which is expressed as

$$\mathbf{X} = \begin{bmatrix} \mathbf{U} & \dot{\mathbf{U}} & \ddot{\mathbf{U}} & h_f & h_r \end{bmatrix}^{\mathbf{T}}$$
(4-4)

where $\mathbf{X}$ is the system vector. The two displacements h_f and h_r are assumed to be independent of each other. Because the pavement roughness is considered a random process, a random-walk model is adopted, in which the mean value of the prior PDF of excitation at time step $k+1$ is equal to the estimated value at time step k, assuming there is not a large difference between two consecutive input values. This relation is expressed as

$$h_{f,k} = h_{f,k-1} + \xi_{f,k}$$
$$h_{r,k} = h_{r,k-1} + \xi_{r,k}$$
(4-5)

in which ξ is the difference between two consecutive excitation values following normal distribution. The standard deviation of ξ for the pavement roughness considered in this simulation is empirically set here to be 0.005 m. The theoretical relation between this

91

value and pavement roughness is not investigated in this research.

For the vehicle response terms in the state vector, the following formula are developed by Newmark method to connect the vehicle acceleration, velocity, and displacement response at time step k with those at time step k-1 (Bang and Kwon, 2000).

$$\ddot{\mathbf{U}}_k = \left(\mathbf{M}_v + \frac{\Delta t}{2} \mathbf{C}_v + \frac{(\Delta t)^2}{4} \mathbf{K}_v \right)^{-1} \left(\mathbf{P}_k + \mathbf{C}_v \mathbf{B}_C + \mathbf{K}_v \mathbf{B}_K \right)$$

$$\dot{\mathbf{U}}_k = \dot{\mathbf{U}}_{k-1} + \frac{\ddot{\mathbf{U}}_{k-1} + \ddot{\mathbf{U}}_k}{2} \Delta t \qquad (4\text{-}6)$$

$$\mathbf{U}_k = \mathbf{U}_{k-1} + \dot{\mathbf{U}}_{k-1} \Delta t + \frac{\ddot{\mathbf{U}}_{k-1} + \ddot{\mathbf{U}}_k}{4} (\Delta t)^2$$

where

$$\mathbf{P}_k = \begin{bmatrix} 0 & 0 & h_{f,k} k_{tf} & h_{r,k} k_{tr} \end{bmatrix}^{\mathrm{T}}$$

$$\mathbf{B}_C = -\dot{\mathbf{U}}_{k-1} - \frac{\ddot{\mathbf{U}}_{k-1}}{2} \Delta t$$

$$\mathbf{B}_K = -\mathbf{U}_{k-1} - \dot{\mathbf{U}}_{k-1} \Delta t - \frac{\ddot{\mathbf{U}}_{k-1}}{4} (\Delta t)^2 \qquad (4\text{-}7)$$

$$\Delta t = t_k - t_{k-1}$$

The relations above are summarized as Eq. (4-8), where J_k is the function defining the relation between system responses in two consecutive steps.

$$\begin{bmatrix} \mathbf{U}_k, \dot{\mathbf{U}}_k, \ddot{\mathbf{U}}_k \end{bmatrix}^{\mathrm{T}} = J_k \left(\begin{bmatrix} \mathbf{U}_{k-1}, \dot{\mathbf{U}}_{k-1}, \ddot{\mathbf{U}}_{k-1}, h_{f,k}, h_{r,k} \end{bmatrix}^{\mathrm{T}} \right) + \mathbf{w}(k) \qquad (4\text{-}8)$$

where $\mathbf{w}(k)$ is the system error aiming at making up for the incompleteness coming from the dynamic model and the discretization for the time evolution in the Newmark method.

Eq. (4-5) and Eq. (4-8) formulate the system equation in which particles are evolved to obtain the prior PDF of the state. The state vector of each particle is transferred to the observation vector through the observation equation shown in Eq. (4-9).

$$\mathbf{Y}_k = \mathbf{BX}_k + \mathbf{v}(k) \tag{4-9}$$

where **B** is the observation matrix defined to extract the corresponding observed values from the state vector, and $\mathbf{Y}_k$ is the observation vector. In this case, the vehicle body acceleration, angular velocity, displacement and angle are included in the observation vector, as shown in Eq. (4-10). The vehicle body displacement and vehicle angle are calculated by double integration of vehicle body acceleration and angular velocity as well as by a high-pass filter. The inclusion of vehicle body displacement and angle is based on the observability analysis (Zhao, 2017). Note that the method may fail if the vehicle body displacement and angle are not included, because the system will thus become unobservable.

$$\mathbf{Y}_k = \begin{bmatrix} u_b & \theta & \ddot{u}_b & \dot{\theta} \end{bmatrix}^{\mathbf{T}} \tag{4-10}$$

The observation matrix B is

$$\mathbf{B} = \begin{bmatrix} 1 & 0 & 0 & 0 & 0 & 0 & 0 & 0 & 0 & 0 & 0 & 0 & 0 & 0 \\ 0 & 1 & 0 & 0 & 0 & 0 & 0 & 0 & 0 & 0 & 0 & 0 & 0 & 0 \\ 0 & 0 & 0 & 0 & 0 & 0 & 0 & 0 & 1 & 0 & 0 & 0 & 0 & 0 \\ 0 & 0 & 0 & 0 & 0 & 1 & 0 & 0 & 0 & 0 & 0 & 0 & 0 & 0 \end{bmatrix} \tag{4-11}$$

In the particle filtering process, the vehicle-bridge interaction is taken into consideration by the iteration process discussed in Section 2.2.2. From the roughness excitation $h_{f,k}$ and $h_{r,k}$, the corresponding bridge responses for each particle can be calculated through the process shown in Fig. 2.3. The bridge responses are then added back to the pavement roughness excitation and the process is repeated until the present calculation of bridge displacement is not larger than 1 % of the absolute value calculated in the previous iteration. The vehicle response after this convergence is then taken as the prediction.

The measurement data is then introduced to evaluate the probability density as represented by the particles. The system state, including the bridge pavement roughness at the front and rear tires at this time step, is then estimated.

4.3 Numerical Example

In this section, a numerical example is given to estimate bridge pavement roughness generated based on ISO 8608. A particle filter is used to estimate the roughness input from the vehicle responses and the estimation result is compared with the true roughness value.

4.3.1 Verification without Noise and Error

The bridge pavement roughness is the main excitation source of the coupled vehicle-bridge system and significantly influences the responses of the system. Therefore, pavement roughness must be realistically assumed. The ISO 8608 provides the power spectral density of road roughness, which is expressed in terms of the summation of a series of harmonics, shown by

$$R(x) = \sum_{i}^{D} \sqrt{2G(n_i)\Delta n} \cos(2\pi n_i x + \varphi_i) \tag{4-12}$$

in which x is the distance along the road; $R(\mathrm{x})$ is the road roughness; Δn is the frequency spacing determined by the total length of the roughness; φ_i is the phase angle, which follows a uniform distribution from 0 to 2π; $G(n_i)$ is the one-sided PSD defined in Eq. (4-13), where $G(n_0)$ is chosen according to different road classes defined in ISO 8608.

$$G(n) = G(n_0)\left(n/n_0\right)^{-2} \tag{4-13}$$

In this chapter, a typical distance history for a 40-meter long pavement with a roughness of class A is generated using the procedure detailed in ISO 8608, which is then used as the deterministic excitation in the simulation. The value of $G(n_0)$ corresponding to class A is 32×10^{-6} m in Eq. (4-13), and n_0 is 0.1 cycles/m. The sampling interval of the pavement roughness is set to 0.05 m, resulting in a sampling frequency of 20 cycles/m, and a D value of 800 is used in Eq. (4-12). The generated roughness is shown in Fig. 4-2.
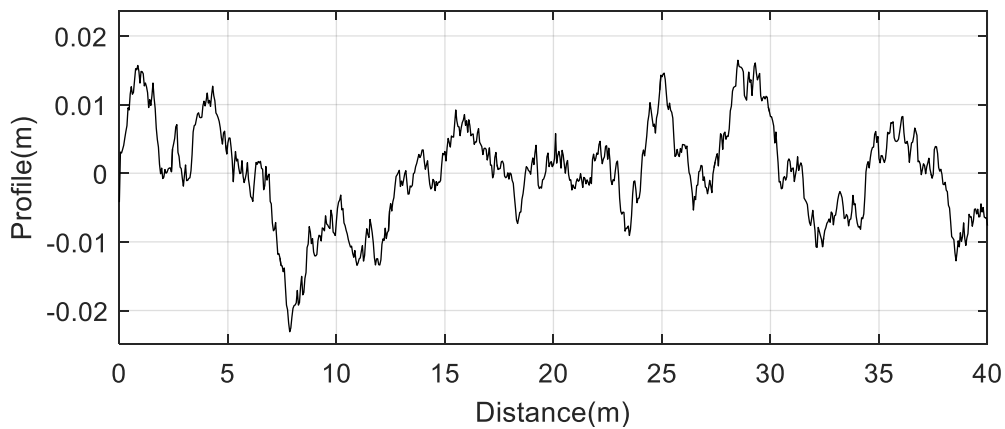
Fig. 4-2. Roughness of a 40-meter long road of Class A

A simply-supported beam model is used for the simulation of the bridge, whose parameters are $\bar{m}$ = 16381 kg/m, length l_s = 40 m, $EI = 1.67\times10^{11}$ N·m², and a damping ratio of 0.05. The first natural frequency is 2.66 Hz.

A probe car with known parameters as listed in Table 4-1 is simulated to cross the test bridge at a speed of 18 km/h. The vehicle responses, such as the vehicle body acceleration response at d_{sen} = 0.3 m and angular velocity response, are calculated by the Newmark method with consideration of the vehicle-bridge interaction. The calculated vehicle responses are shown in Fig. 4-3.

Table 4-1. Vehicle parameters used in simulation

m_b (kg)	m_f (kg)	m_r (kg)	I_y (m^2)	$c_f = c_r$ (N·m/s)
840	106	152	1100	2500
k_f (N/m)	k_r (N/m)	$k_{tf} = k_{tr}$ (N/m)	L_f (m)	Wheelbase (m)
20 000	26 000	400 000	1.4	2.87
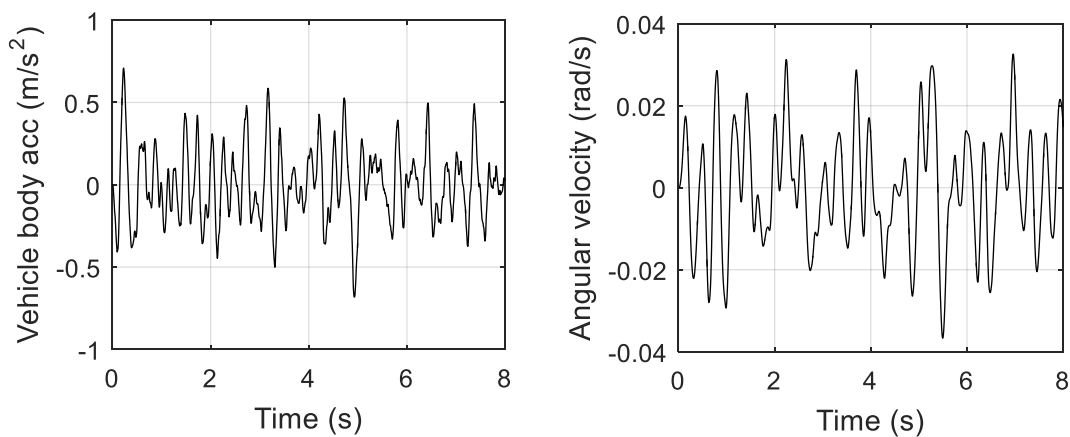
Fig. 4-3. Calculated vehicle responses

The simulation is conducted as per the process detailed in Section 4.2 and the results are shown in Fig. 4-4 (a) and (b), for front and rear estimation, respectively. It is seen that the estimated bridge pavement roughness coincides well with the target roughness. Also, the estimation result without considering vehicle-bridge interaction is also shown. Clear difference is observed compared with the target values, especially around bridge mid-span, where the bridge deflection is considered to be large. Therefore, the vehicle-bridge interaction must be considered to avoid large errors from bridge vibration.
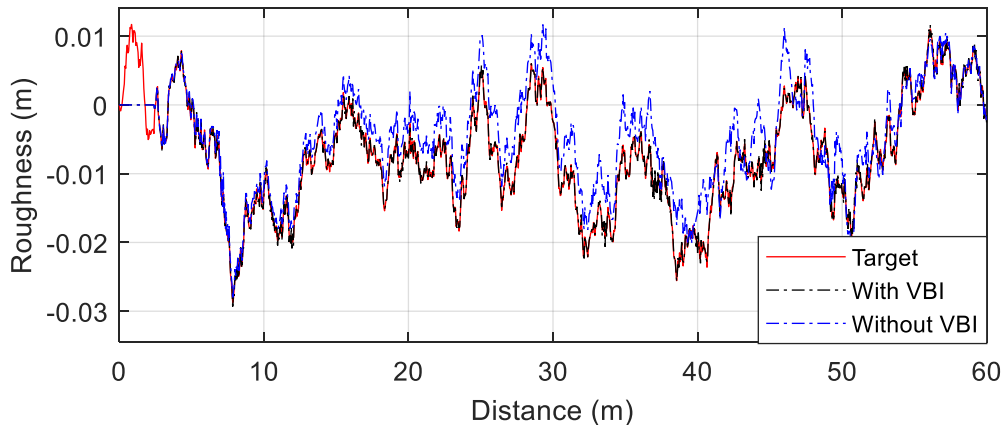
(a) Estimation under front tire
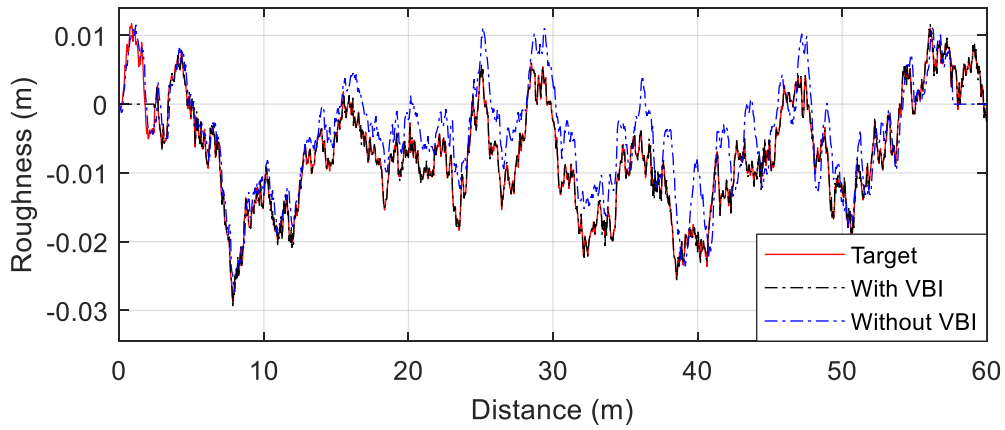
(b) Estimation under rear tire

Fig. 4-4. Estimation results for front and rear tire for with and without VBI

To check the influence from VBI more clearly, the signals shown in Fig. 4-4 (a) are also shown in the frequency domain as Fig. 4-5. From this figure, it is observed that when VBI is not considered, a clear peak occurs at the bridge fundamental frequency (in this case, 2.66 Hz), which makes the estimation of the pavement roughness inaccurate.
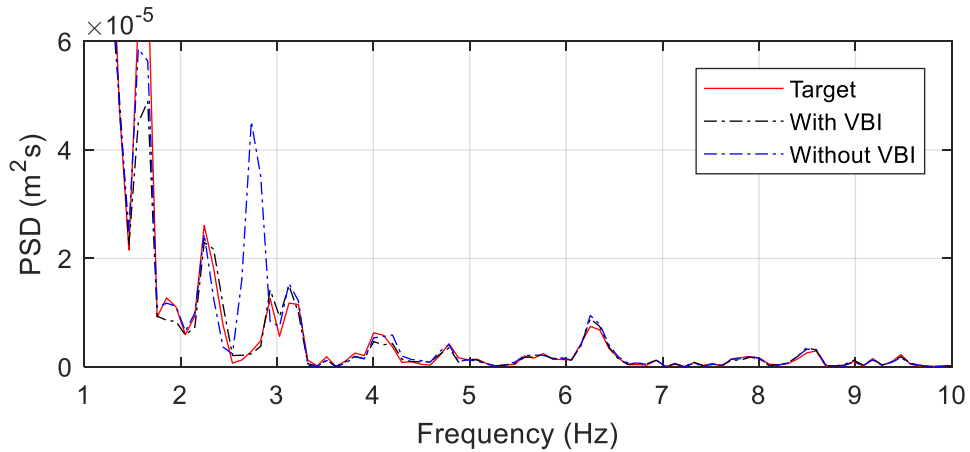
Fig. 4-5. Estimation under front tire in the frequency domain

4.3.2 Influence from Sensor Noise and Modelling Error

As discussed in the corresponding section in Chapter 3, the main noise and error source of vehicle drive-by monitoring include vehicle sensor noise and the vehicle model calibration error. In this section, the influence from vehicle sensor noise and vehicle modelling error is included in the numerical example.

An artificial white noise with a standard deviation of 10 % of the RMS value of the real response is added to the measured responses to account for sensor noise. This percentage of noise is based on the noise and signal levels of typical sensors. The noise-polluted vehicle body acceleration and angular velocity are then integrated to obtain the vehicle body displacement and angle to form the observation vector as per Eq. (4-10). A high-pass filter of 0.2 Hz is used before the integration to reduce the integration error at the low frequency range. A high-pass filter of 0.2 Hz is used before the integration to reduce the integration error at the low frequency range.

In a real implementation, the probe car should be calibrated to obtain the half-car model parameters. The calibration errors for the parameters of the probe car also need to be addressed. The half-car parameters listed in Table 4-1 are calibrated through a hump test described in Chapter 3.4.1. The calibration errors of these parameters are shown in Table 4-2. These errors are multiplied by a scale factor of two to account for the possibility of larger estimation errors in real implementation. The vehicle parameter errors lead to a 10 % decrease in the vehicle fundamental frequency, from 1.13 Hz to 1.02 Hz.

The errors in the bridge stiffness and damping ratio are also accounted for by increasing the bridge stiffness EI by 10 % and the damping ratio by 30 %.

Table 4-2. Artificial errors in the vehicle parameters

Name	m_b	m_f	m_r	I_y	k_f
Calibrated	-0.4%	+7.2%	N/A[*]	+4.3%	+11.1%
Adopted	-0.8%	+14.4%	N/A	+8.6%	+22.2%
Name	k_r	k_{tf}	k_{tr}	c_f	c_r
Calibrated	-9.7%	-12.2%	+5.1%	+9.1%	-3.5%
Adopted	-19.4%	-24.4%	+10.2%	+18.2%	-7.0%

[*]m_r is obtained by $m_r = m_{total} - m_b - m_f$, where m_{total} is considered to be accurate

The estimation results considering the sensor noise and vehicle calibration error are shown in Fig. 4-6. As discussed in previous section, the results without considering vehicle-bridge interaction are not shown here.
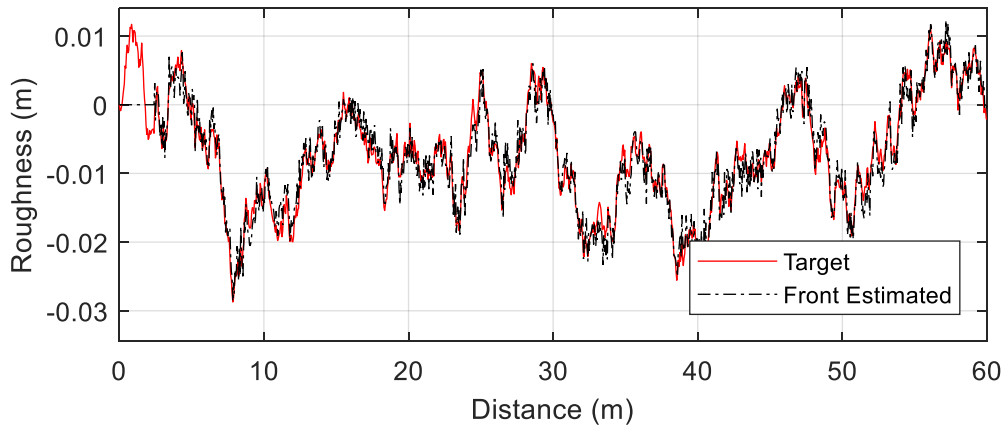
(a) Estimation under front tire
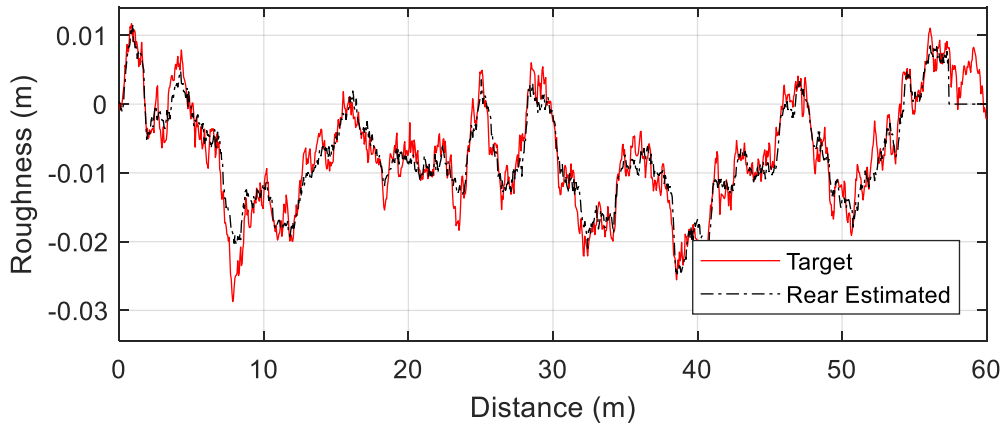
(b) Estimation under rear tire

Fig. 4-6. Estimation with sensor noise and vehicle modelling error

The front and rear estimation errors for the cases of with and without noise are listed in Table 4-3. The rear estimation has larger errors than the front estimation. This is because the sensor is simulated to be placed closer to the front tire than the rear tire. Therefore, the responses at the sensor location is more sensitive to the input pavement roughness under the front tires

Table 4-3. Front and rear estimation errors in simulation

	Without noise	With noise
Front estimation	11.81 %	29.39 %
Rear estimation	33.49 %	42.77 %

4.3.3 Influence from Driving Speed

The above process for roughness estimation is repeated for different driving speeds to check the dependency on the vehicle speed. The estimation errors are summarized in Table 4-4. When the vehicle speed is 10 km/h, the estimation error is larger than other speed cases. This error is due to the high-pass filter with the cut-off frequency of 0.2 Hz before the integration of the vehicle acceleration and angular velocity. The signals lower than 0.072 cycle/m are eliminated through the high-pass filter for 10 km/h case, leading to a large error in the roughness. For higher speeds, the estimation error becomes larger. The reason is that when vehicle speed increases, the same spatial frequency components of the roughness correspond to higher temporal frequency, whose estimation accuracy level is lower than the low frequency part.

Table 4-4. Roughness estimation errors for different driving speed cases

Speed (km/h)	10	20	30	40
Error (%)	51.01	28.75	30.88	36.81

4.4 Experimental Validation at Tsukige Bridge

To validate the proposed algorithm, a field measurement was conducted at Tsukige bridge.

Overview of this bridge and the bridge properties are described in Section 2.3.1.

A Toyota Hi-Ace van, shown in Fig. 4-7, was chosen as the probe car to conduct the bridge pavement roughness estimation. The vehicle parameters must be known in order to accurately estimate the roughness. A hump test was conducted to obtain the necessary parameters of the probe car, in which a portable hump with known geometry was used as input, as already described in Section 3.4.1.

Fig. 4-7. Vehicle used to estimate pavement roughness

The probe car was then driven across the bridge and the vehicle response data was recorded by an iPod touch® device equipped with accelerometers and gyros installed on the vehicle body above the front wheel. This device was set to record the acceleration and angular velocity time history with a sampling frequency of 100 Hz. Because the fluctuation of the sampling rate over time of the iPod touch-based sensors was larger than that of conventional measurement equipment, a resampling based on the time stamp was performed (Nagayama et al, 2009). These sensors were synchronized to wireless sensors

on the bridge by developing acceleration measurement systems equipped with GPS and installing them both on the vehicle and on the bridge. In addition, a GPS sensor was used to determine the vehicle speed data at every second to capture any possible change in speed.

The test vehicle was driven to pass across the bridge at different speeds, including 20, 30, 40, and 50 km/h. The passing route of the vehicle is shown in Fig. 4-8. The route includes the bridge and a road section of around 200 meters. The route is determined considering reasonable place for the vehicle to take U-turn.
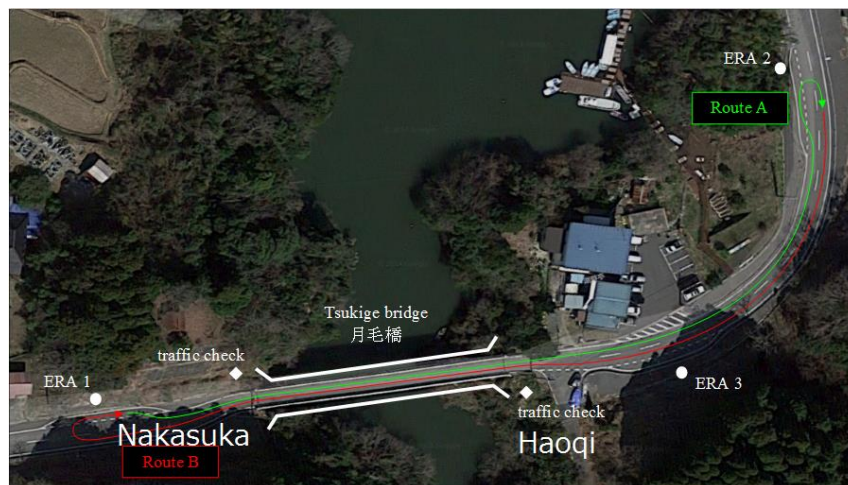
Fig. 4-8. Passing route of the vehicle

For each driving speed, three tests were conducted. To examine the accuracy of the roughness estimation, the bridge pavement roughness was also measured by a portable profiler, shown in Fig. 4-9.

Fig. 4-9. Portable pavement profiler (Suntop techno Corporation)

The roughness excitation to the vehicle is estimated following the procedure described in previous sections and is compared with the values obtained through the portable profiler. A band-pass filter of 0.05–1.5 cycles/m was applied before comparison. For normal driving speeds, 1.5 cycles/m corresponds to around 10 Hz in the frequency domain, so the band-pass filter used here covers the range of effective excitation.

A typical result when the driving speed is 30 km/h is shown in Fig. 4-10. The first 59 m corresponds to the bridge length, while the remainder of the data is shown in the figure for the purposes of comparison. Good accuracy of the proposed roughness estimation method is observed with an error of 7.94 %. The definition of this error is the same as shown in Eq. (3-22).
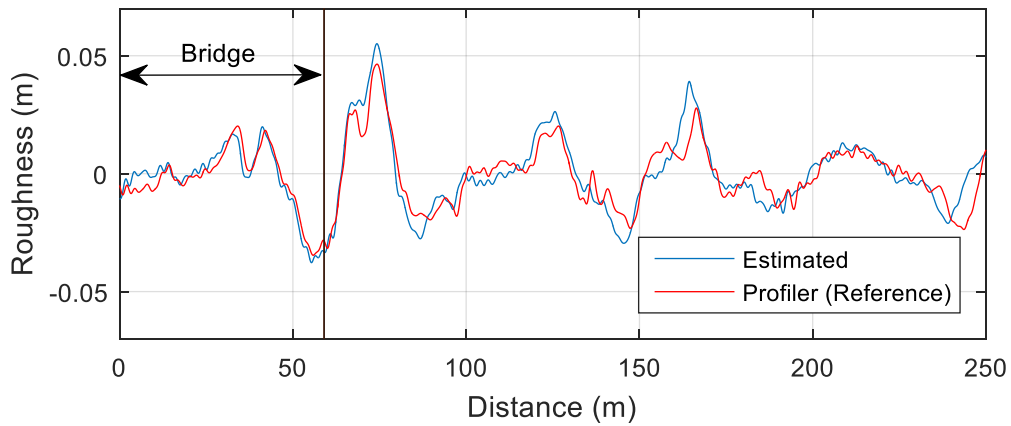
Fig. 4-10. Pavement roughness estimation of the entire vehicle passing route

The results without considering vehicle-bridge interaction is also shown in Fig. 4-11. The fluctuations caused by the components of bridge vibration is clearly observed, showing again the importance of compensating the influence from bridge vibration.
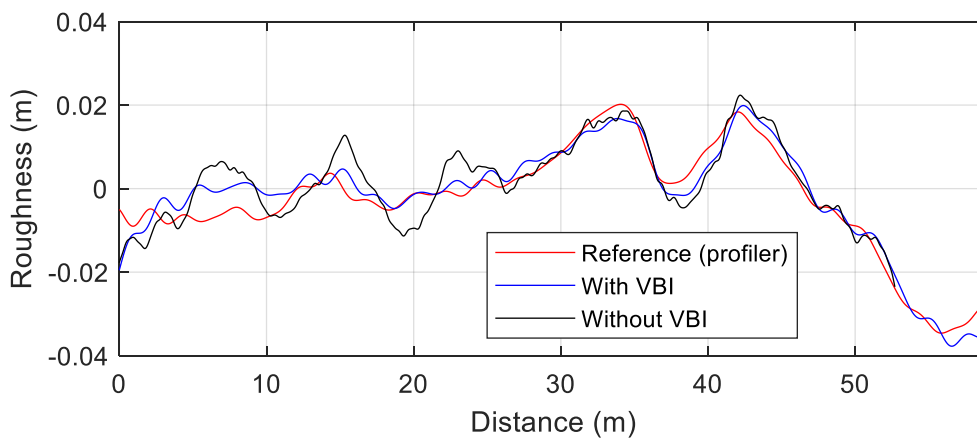
Fig. 4-11. Effect of with and without considering vehicle-bridge interaction

The estimation errors for all the tests of each driving speed are listed in Table 4-5. It is observed that the accuracy is higher when the vehicle is driven at 30 and 40 km/h. For the lower driving speed, the error is mainly due to the high-pass filter before the integration

105

of the vehicle acceleration and angular velocity, making some long wavelength components disappear for the low driving speed tests. For the high driving speed around 50 km/h, the vehicle speed may be obtained with poor accuracy due to the low sampling rate of 1 Hz of the GPS device. Also, at high driving speed, the vehicle-bridge interaction is enlarged because the bridge vibration becomes larger. Estimation error from the bridge dynamic properties will thus be enlarged, leading to a lower accuracy for the high driving speed of the vehicles.

Table 4-5. Estimation result and error

Vehicle Speed		20 km/h	30 km/h	40 km/h	50 km/h
Error	Test 1	56.14 %	7.94 %	17.52 %	41.94 %
	Test 2	48.36 %	11.83 %	18.26 %	71.94 %
	Test 3	59.70 %	20.21 %	21.12 %	54.87 %

Some typical results for each driving speed is shown in Fig. 4-12 (a) – (d). Together with Table 4-5, one conclusion can be drawn that for the bridge pavement roughness estimation, the driving speed of around 30 – 40 km/h is preferred to obtain higher estimation accuracy.
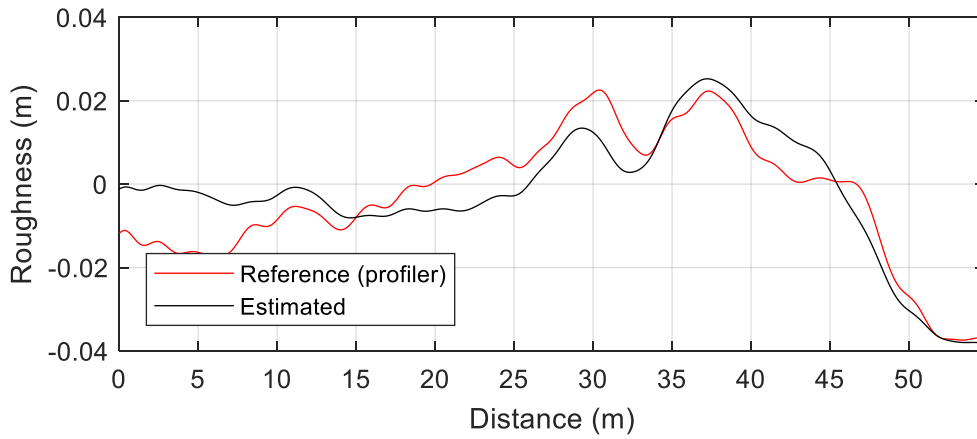
(a) 20 km/h (Error: 48.36 %)
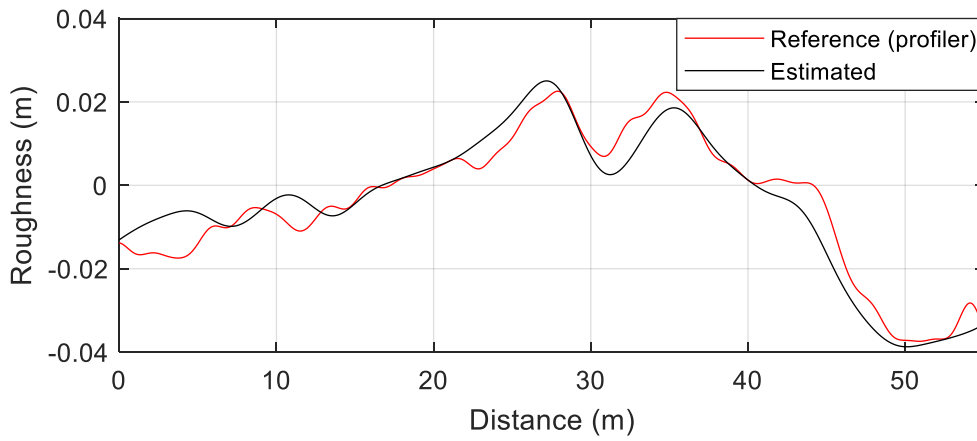
(b) 30 km/h (Error: 7.94 %)
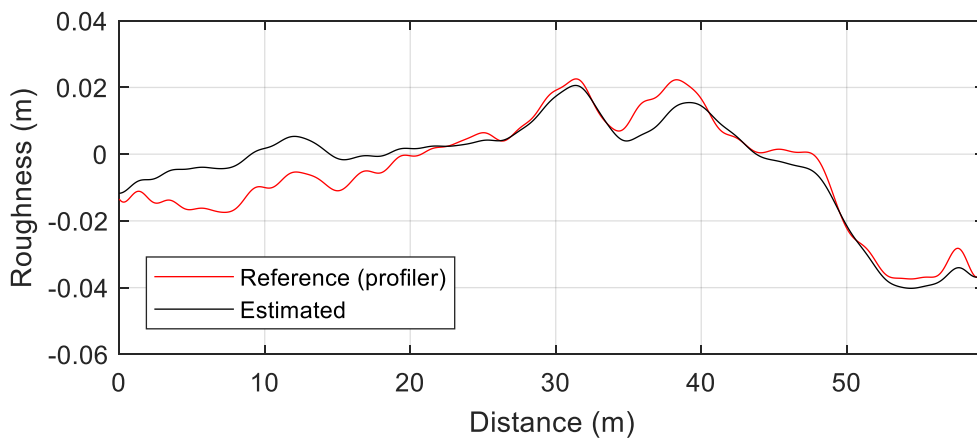
(c) 40 km/h (Error: 17.52 %)
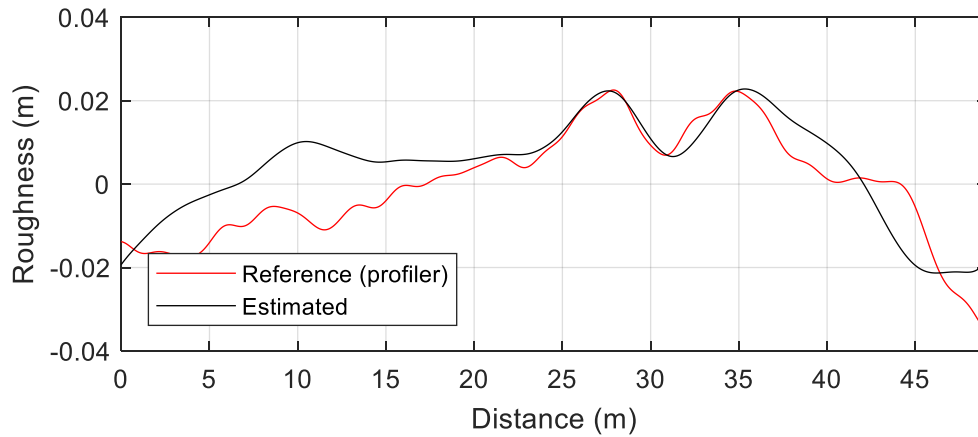
(d) 50 km/h (Error: 41.94 %)

Fig. 4-12. Typical results for each driving speed

4.5 Summary

In this chapter, a method to estimate bridge pavement roughness from vehicle responses is proposed. Vehicle body acceleration and angular velocity are measured as observation in the particle filter method. Integration is conducted from acceleration and angular velocity to obtain vehicle displacement and angle to satisfy the requirement from observability. Comparison was made between the estimation with and without considering vehicle-bridge interaction. Numerical results and experimental results both show that the bridge vibration affects the pavement roughness estimation if the vehicle-bridge interaction is neglected. Good accuracy is obtained by comparing the estimation results with the roughness measured by a portable profiler. The estimated roughness will serve as the system input for vehicle parameter identification in the next chapter.

Chapter 5 Identification of moving vehicle parameters using bridge responses and estimated bridge pavement roughness

5.1 Overview

Passing vehicles cause bridge deformation and vibration. Overloaded vehicles can result in fatigue damage to, or even failure of, the bridge. The bridge response is related to the properties of the passing vehicles, particularly the vehicle weight. Therefore, a bridge weigh-in-motion system for estimating vehicle parameters is important for evaluating the bridge condition under repeated load. However, traditional weigh-in-motion methods, which involve the installation of strain gauges on bridge members and calibration with known weight truck, are often costly and time-consuming.

In this chapter, a method for the identification of moving vehicle parameters using bridge acceleration responses is investigated. A time-domain method base on the Bayesian theory application of a particle filter is adopted. The bridge pavement roughness, which is estimated from Chapter 4, is adopted as the input of the vehicle-bridge coupling system. Numerical simulations demonstrate that the vehicle parameters, including the vehicle weight, are estimated with high accuracy and robustness against observation noise and modelling error. Finally, this method is validated through field measurement at Tsukige Bridge. The resulting estimate of the vehicle mass agrees well with the measured value, demonstrating the practicality of the proposed method.

5.2 Implementation of Particle Filter on Vehicle Parameter Identification from Bridge Responses

In this section, a method for identifying vehicle parameters from the known roughness input and measured bridge responses is introduced. When a vehicle passes over a bridge, vehicle-induced vibration occurs. The bridge acceleration and displacement responses are obtained and used to estimate the parameters of the vehicle causing this bridge vibration through the particle filter process. The vehicle-bridge interaction is also taken into consideration using the iterative method explained in Section 2.2.2. For the purposes of parameter identification, the state vector should include the unknown parameters shown in

$$\mathbf{X}_2 = \begin{bmatrix} \mathbf{U} & \dot{\mathbf{U}} & \ddot{\mathbf{U}} & \mathbf{q} & \dot{\mathbf{q}} & \ddot{\mathbf{q}} & \mathbf{\Theta} \end{bmatrix}^T \tag{5-1}$$

in which $\mathbf{U}$ is vehicle displacement response defined in Eq. (2-6), $\mathbf{q}$ is the bridge modal displacement response, and $\mathbf{\Theta}$ is the unknown vehicle parameter vector with the form of

$$\mathbf{\Theta} = \begin{bmatrix} m_b & I_y & m_f & m_r & k_f & k_r & k_{tf} & k_{tr} & c_f & c_r \end{bmatrix}^T \tag{5-2}$$

If the vehicle passing lane is to be estimated, the parameter indicating the vehicle's transverse position should also be included in the state vector. This issue will be addressed in Chapter 6.

For the unknown parameters, particles are generated following a uniform distribution. As the parameter values are time-invariant, they evolve through the system equation given by:

$$\mathbf{\Theta}_{k+1} = \mathbf{\Theta}_k + \mathbf{w}(k) \tag{5-3}$$

where $\mathbf{w}(k)$ is the system error term that prevents the parameters from getting frozen in the particle filtering process.

For the observation equation, the bridge response data at 1/4 span, mid-span, and 3/4 span after the convergence of the vehicle-bridge interaction are calculated through the observation equation in Eq. (5-4) for each particle, and are considered to be the prediction values for this step, which are accordingly used for particle filtering. The reason for choosing 1/4 span, mid-span, and 3/4 span is that the first and second mode bridge responses are well captured at these three points. The observation equation is shown as

$$\mathbf{Y}_k = \mathbf{B}\mathbf{X}_k + \mathbf{v}(k) \tag{5-4}$$

where $\mathbf{Y}_k$ is the observation vector:

$$\mathbf{Y}_k = \left[\ddot{y}_{1/2,k}, \ddot{y}_{1/4,k}, \ddot{y}_{3/4,k} \right]^{\mathrm{T}} \tag{5-5}$$

The equation above corresponds to the case where only bridge acceleration responses at three locations are observed. For the case where bridge displacement responses are also included, the observation vector becomes:

$$\mathbf{Y}_k = \left[y_{1/2,k}, y_{1/4,k}, y_{3/4,k}, \ddot{y}_{1/2,k}, \ddot{y}_{1/4,k}, \ddot{y}_{3/4,k} \right]^{\mathrm{T}} \tag{5-6}$$

The effectiveness of including the bridge displacement responses in the observation vector is discussed in Section 5.3.4 and is theoretically proven through the sensitivity analysis described in Section 5. 3.7.

5.3 Numerical Example

5.3.1 Verification without Noise and Error

In this section, the parameters of the passing vehicle are identified by using the bridge responses and the estimated bridge pavement roughness in Chapter 4, as shown Fig. (4-2). Bridge acceleration responses induced by a passing vehicle with a speed of 30 km/h are calculated at 1/4 span, mid-span, and 3/4 span as the measured responses. Although the inclusion of more modes will lead to a more accurate result, only the first three modes are considered in the modal decomposition analysis in this paper because for a simply-supported bridge with a natural frequency of 2.66 Hz, as considered here, the frequency of the 4th mode will be higher than 40 Hz, making the amplitudes of the frequency components of the pavement roughness input negligibly low compared to the first three modes.

The estimation results for each of the half-car parameters are shown in Fig. 5-1 (a) – (i). All parameters converge to the corresponding target value in short time. The standard deviation of the particle at each time step is also shown, which become closer to zero as the time step increases. The converging process of the vehicle total mass, i.e., vehicle body mass plus two tire mass, is shown in Fig. 5-1 (j). The estimation error of each parameter is smaller than 0.1 %, compared with each corresponding true value.
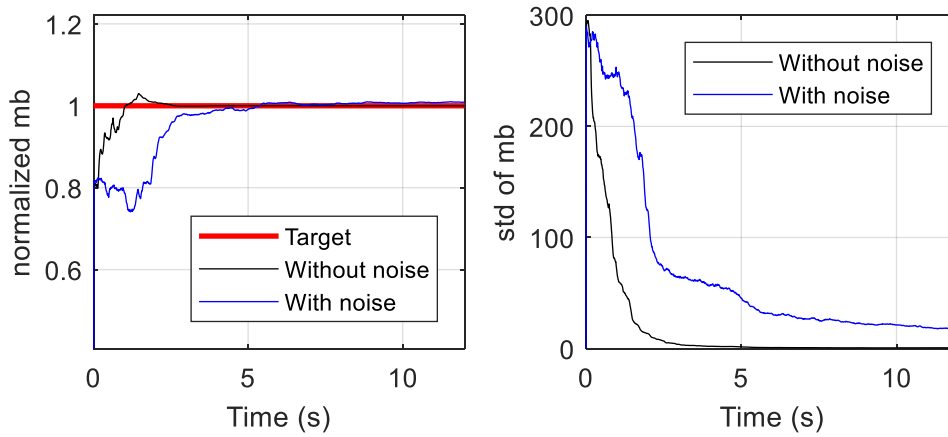
(a) Converging process of vehicle body mass
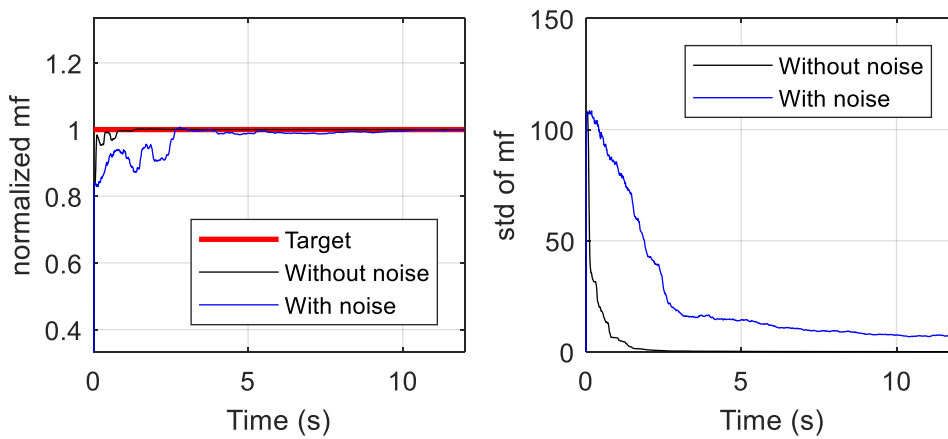
(b) Converging process of front tire mass
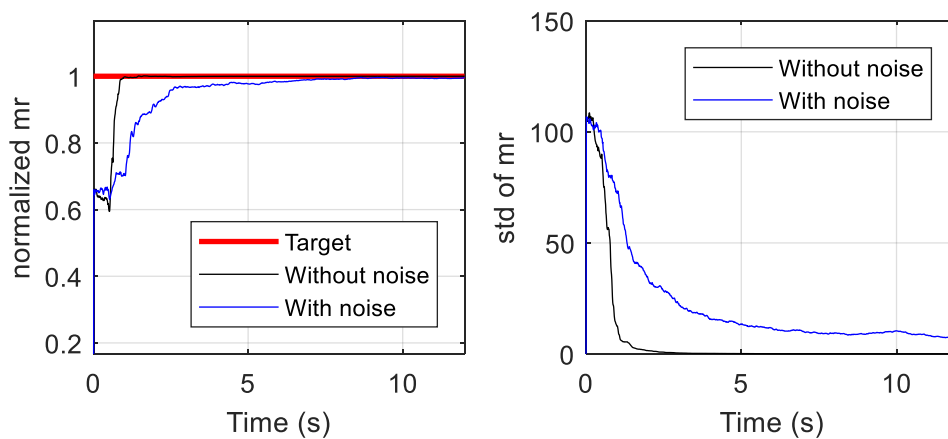
(c) Converging process of rear tire mass

113
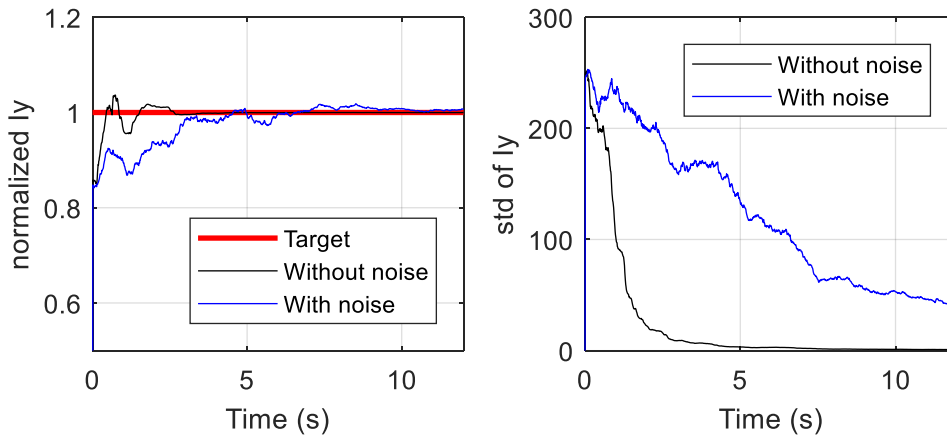
(d) Converging process of moment of inertia
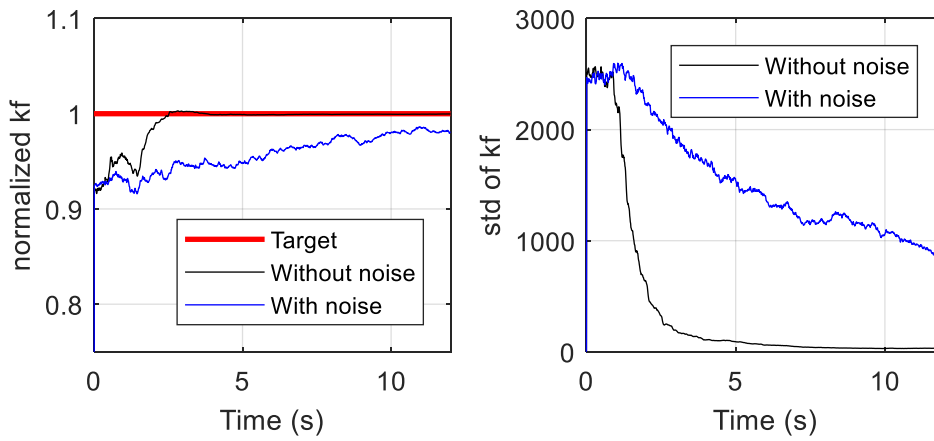
(e) Converging process of front suspension stiffness
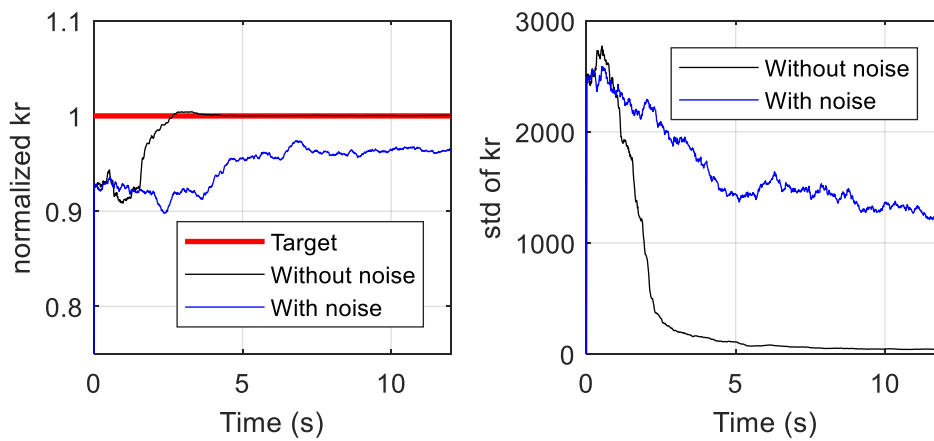
(f) Converging process of rear suspension stiffness
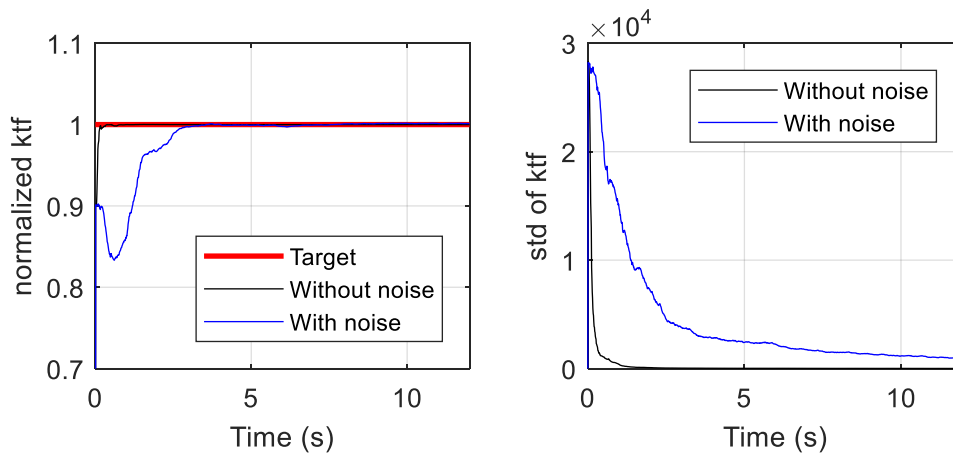
(g) Converging process of front tire stiffness
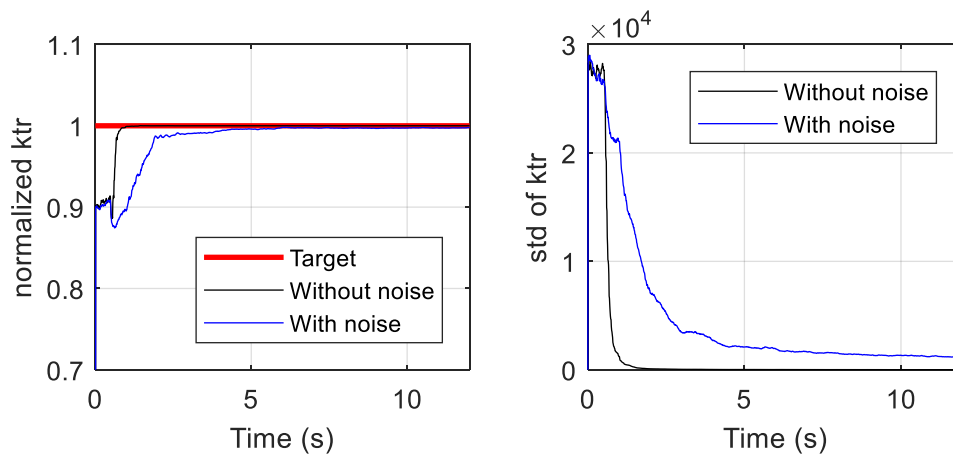
(h) Converging process of rear tire stiffness
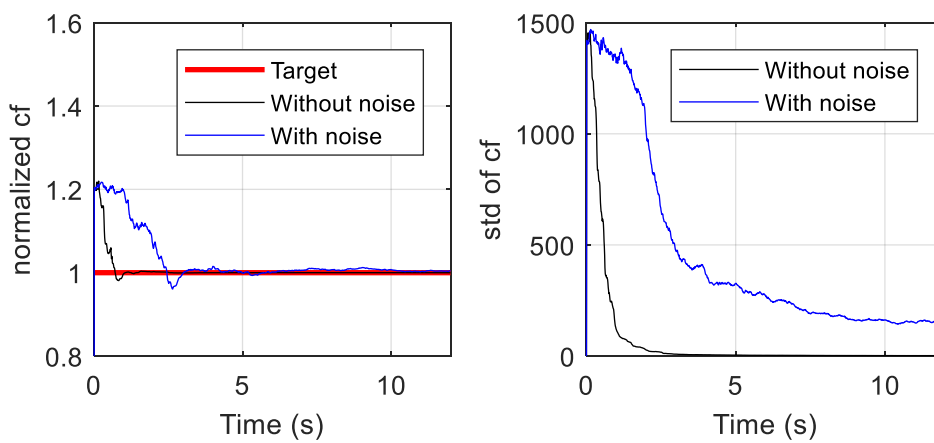
(i) Converging process of front suspension damping
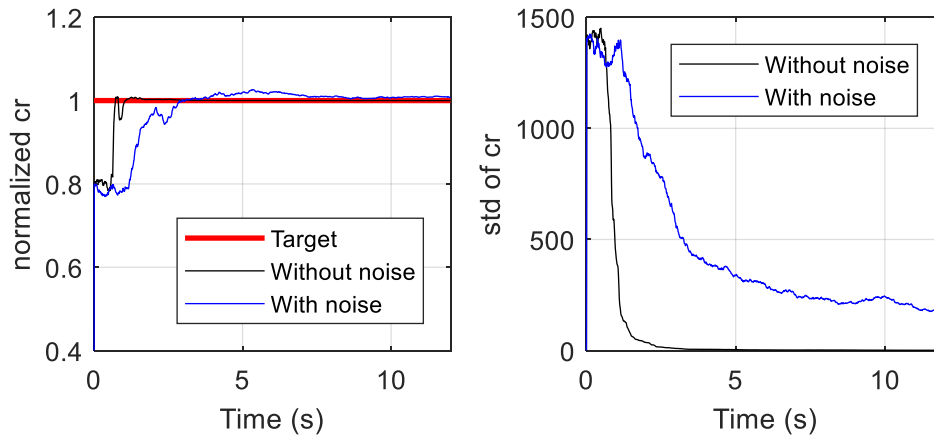
(j) Converging process of rear suspension damping
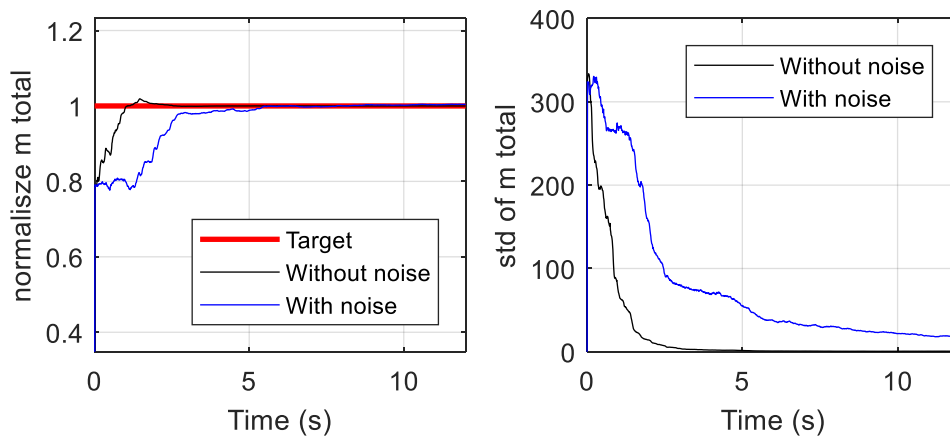
(k) Converging process of vehicle total mass

Fig. 5-1. Converging process of each vehicle parameter

The bridge responses at each of the sensor place, i.e., mid-span, 1/4-span, and 3/4-span, are reconstructed from the estimated vehicle parameters and are shown in Fig. 5-2. The good agreement between the reconstructed signal and the real one partially supports the estimation results.
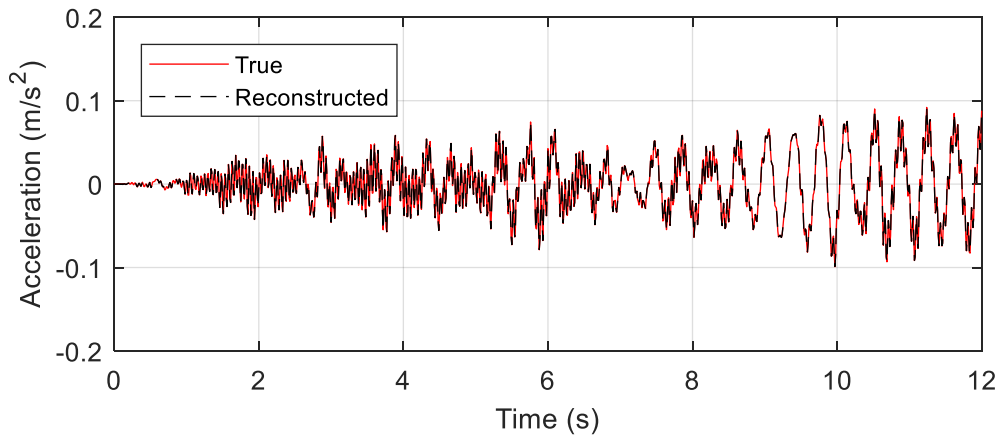
(a) Mid-span acceleration
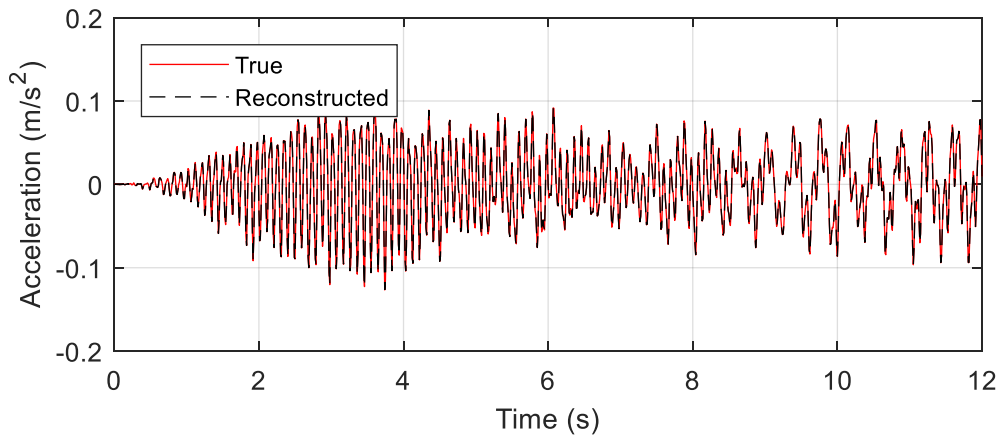
(b) 1/4-span acceleration
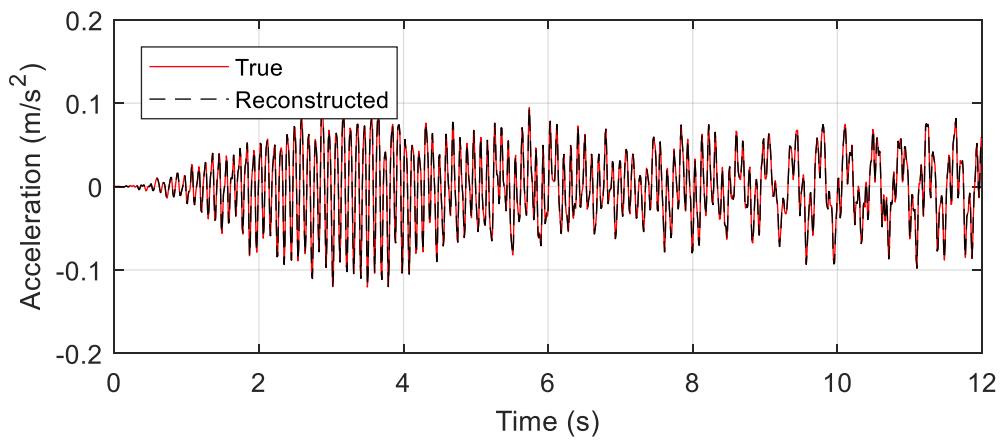
(c) 3/4-span acceleration

Fig. 5-2. Comparison of true responses and reconstructed responses

5.3.2 Influence from Sensor Noise and Pavement Estimation Error

For the problem discussed in this chapter, the noise and error sources come from the sensor noise and the pavement estimation error. In this section, the influence from these noise and error terms are discussed.

Instead of using the true pavement input, the estimated roughness from Chapter 4 is used as the input roughness to the vehicle, to consider the errors terms induced by pavement estimation error. 10 % artificial noise is added to the bridge acceleration data to simulate the sensor noise in real situations. In this simulation, the standard deviation of system error $\mathbf{w}(k)$ in Eq. (5-3) is set to 0.5 % of the nominal values of each unknown parameter, while the standard deviation of the observation error is set as 10 % of the corresponding responses, which is the same as the sensor noise level.

The estimation error of each parameter is shown together with the case without noise in Fig. 5-1. It is noted that although slower than the case without noise, most parameters converge to the target value. However, the front suspension stiffness k_f and rear suspension stiffness k_r do not converge to the target value. This effect is due to fact that these two parameters are not sensitive to bridge acceleration response, which will be discussed in later sections.

Table 5-1. Estimation error of vehicle parameters

Parameter	m_b	m_f	m_r	I_y	k_f
Error	0.8 %	0.2 %	0.5 %	0.5 %	2.5 %

Parameter	k_r	k_{tf}	k_{tr}	c_f	c_r
Error	3.5 %	0.15 %	0.2 %	0.5 %	1 %
Parameter	m_{total}				
Error	0.5 %				

5.3.3 Influence from Bridge Modal Mass Error

The bridge model mass is considered in this section. As stated in previous section, the bridge modal mass is an important value in the vehicle static load identification problem. In the particle filtering process of the numerical example, the bridge modal mass is increased by 5 % to consider possible error in the estimation of bridge modal mass values from Chapter 3 or from bridge design drawings. The bridge natural frequencies and damping ratios of each mode are assumed to be obtained accurately. As a result, in the decomposed equations of motion of the bridge system shown in Eq. (2-22), the modal damping and stiffness on the left-hand side are increased proportionally with the modal mass. Therefore, the vehicle load in the right-hand side is also identified with proportional inaccuracy, as shown in Fig. 5-3, where an estimation error of 4.86 % is found.
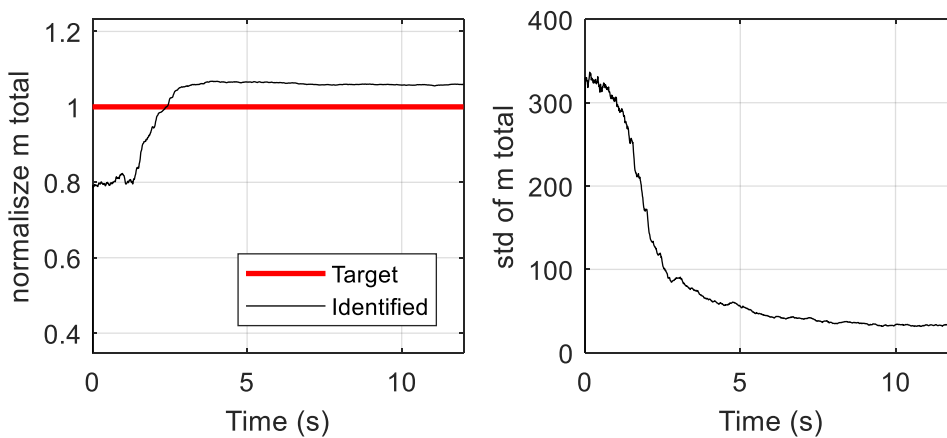
Fig. 5-3. Converging process of vehicle total mass with noise and modal mass error

5.3.4 Effect of Including Bridge Displacement Estimation

To determine the effect of including the bridge displacement responses, a comparison was made between the result of using only bridge acceleration and of using both acceleration and displacement, which is obtained through the double-integration of acceleration data with a cut-off frequency of 0.2 Hz in a high-pass filter. While all the vehicle parameters converge to their real values, the converging process for only the total mass is shown in Fig. 5-4 (a), as normalized by its real value. Fig. 5-4 (b) shows the standard deviation of the particle at each time step. When bridge displacement response is considered, the vehicle parameters, in particular the vehicle mass, converge faster and more accurately towards the target value. This increase in accuracy provided by including bridge displacement can be proven by the parameter sensitivity analysis described in the sensitivity analysis in this chapter.
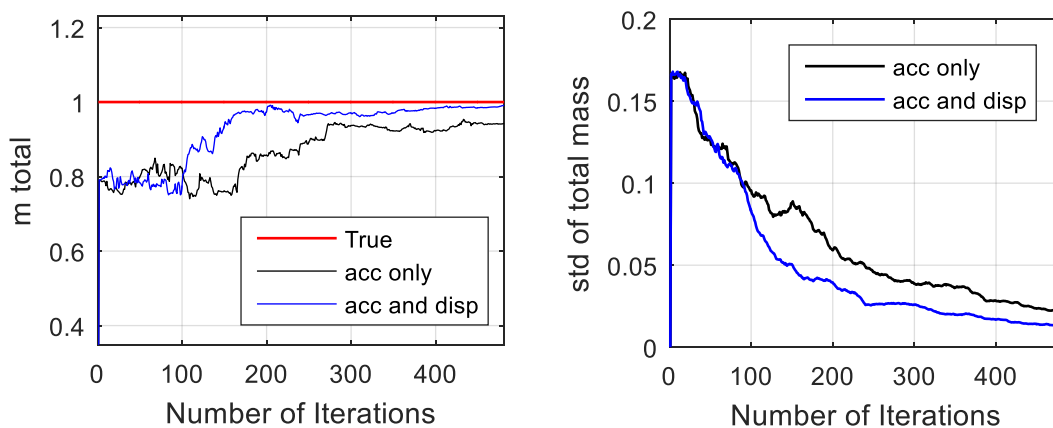
Fig. 5-4. Convergence of vehicle total mass with bridge displacement estimation

5.3.5 Influence from Vehicle Speed

The parameter identification process is repeated for different driving speeds using the same estimated roughness as shown in Fig. 4-5. The identification error of total mass is

summarized in Table 5-2. As the driving speeds become higher, the identification error slightly increases, because less points of the estimated roughness are used in the identification process due to a fixed value of Δt while still showing satisfied accuracy level.

Table 5-2. Vehicle total mass identification errors for different driving speed cases

Speed	20 km/h	30 km/h	40 km/h	50 km/h
Error	1.5 %	1.5 %	1.9 %	2.1 %

5.3.6 Effect of Weighted Global Iteration

In the above numerical example, the noise level is set as 10 %. However, when the noise is artificially increased in to 30 %, a larger identification error occurs, as shown in Fig. 5-5. A weighted-global-iteration (WGI) method is used here to improve the accuracy (Hoshiya and Maruyama, 1987). This method is based on the fact that after each filtering process, the particles can better represent the distribution of the system state, which leads to more accurate identification results. More rounds of particle filtering are conducted. The initial uniform distribution range of each round is reset to be ±15 % of the converged value of the previous round for each parameter. The converging process of up to six rounds are shown in Fig. 9. After WGI process, the accuracy is improved from 5.2 % to 1.0 %.
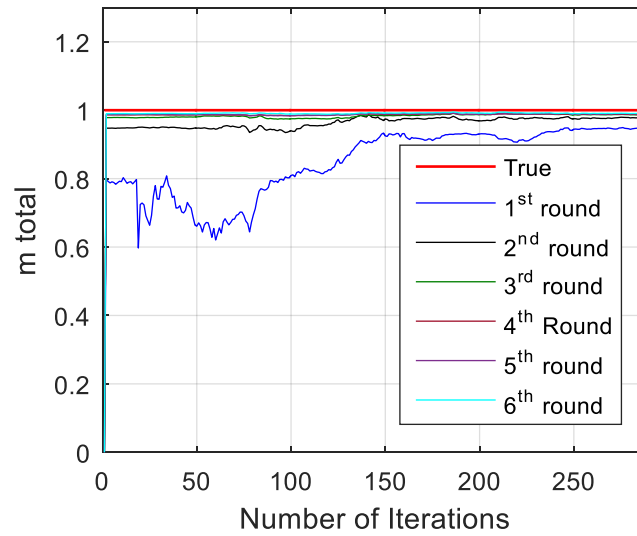
Fig. 5-5. The effect of weighted global iteration

5.3.7 Sensitivity Analysis of Vehicle Parameters on Bridge Responses

The value of each vehicle parameter is identified using the measured bridge responses. To achieve this end, the bridge responses must be sufficiently sensitive to the change of vehicle parameters. An analysis is conducted here to evaluate the sensitivity of each vehicle parameter to the bridge acceleration and displacement response following the method of Lu and Law (2007).

The equation of motion of a dynamic system is written as

$$\mathbf{M\ddot{d}} + \mathbf{C\dot{d}} + \mathbf{Kd} = \mathbf{F}_P \tag{5-7}$$

where $\mathbf{M}$, $\mathbf{C}$, and $\mathbf{K}$ are the mass, damping, and stiffness matrices, respectively, F_P is the system input, and d is the displacement response.

122

If a system parameter α, which is assumed to be only related to the stiffness matrix $\mathbf{K}$, is perturbed by $\Delta\alpha$, the perturbed equation of motion is obtained by differentiating both sides of Eq. (5-7) with respect to the system parameter α. The perturbed equation is:

$$\mathbf{M}\frac{\partial\ddot{\mathbf{d}}}{\partial\alpha}+\mathbf{C}\frac{\partial\dot{\mathbf{d}}}{\partial\alpha}+\mathbf{K}\frac{\partial\mathbf{d}}{\partial\alpha}=-\frac{\partial\mathbf{K}}{\partial\alpha}\mathbf{d} \tag{5-8}$$

Assuming that

$$\mathbf{w}=\frac{\partial\mathbf{d}}{\partial\alpha} \tag{5-9}$$

we have

$$\mathbf{M}\ddot{\mathbf{w}}+\mathbf{C}\dot{\mathbf{w}}+\mathbf{K}\mathbf{w}=-\frac{\partial\mathbf{K}}{\partial\alpha}\mathbf{d} \tag{5-10}$$

Since the displacement $\mathbf{d}$ and system matrices $\mathbf{M}$, $\mathbf{C}$, and $\mathbf{K}$ are all known, the sensitivities $\mathbf{w}$, $\dot{\mathbf{w}}$, and $\ddot{\mathbf{w}}$ can be numerically calculated by solving Eq. (5-10) using the Newmark method.

The equations of motion for the vehicle and bridge are described in Section 2 and repeated here:

$$\mathbf{M}_v\ddot{\mathbf{U}}+\mathbf{C}_v\dot{\mathbf{U}}+\mathbf{K}_v\mathbf{U}=\mathbf{P} \tag{5-11}$$

$$\mathbf{M}_b\ddot{\mathbf{q}}+\mathbf{C}_b\dot{\mathbf{q}}+\mathbf{K}_b\mathbf{q}=\mathbf{F}_b \tag{5-12}$$

The process of calculating the sensitivity of k_f in the vehicle stiffness matrix $\mathbf{K}_v$ is given here. The analysis of other vehicle parameters is similar. The equations of the vehicle and bridge system are differentiated on both sides, giving

$$\mathbf{M}_v\frac{\partial\ddot{\mathbf{U}}}{\partial k_f}+\mathbf{C}_v\frac{\partial\dot{\mathbf{U}}}{\partial k_f}+\mathbf{K}_v\frac{\partial\mathbf{U}}{\partial k_f}=-\frac{\partial\mathbf{K}_v}{\partial k_f}\mathbf{U} \tag{5-13}$$

$$\mathbf{M}_b \frac{\partial \ddot{\mathbf{q}}}{\partial k_f} + \mathbf{C}_b \frac{\partial \dot{\mathbf{q}}}{\partial k_f} + \mathbf{K}_b \frac{\partial \mathbf{q}}{\partial k_f} = k_{tf} \frac{\partial u_f}{\partial k_f} \phi_i(x_f) + k_{tr} \frac{\partial u_r}{\partial k_f} \phi_i(x_r) \qquad (5\text{-}14)$$

where x_f and x_r are the location of the front and rear tire on the bridge, respectively. Note that $\partial u_f/\partial k_f$ and $\partial u_r/\partial k_f$ in Eq. (5-14) are extracted from the third and fourth terms of $\partial U/\partial k_f$ in Eq. (5-13), respectively. The sensitivity terms are thus obtained by solving Eq. (5-14).

The acceleration and displacement sensitivities at mid-span are calculated by Eq. (5-15) using modal decomposition:

$$\frac{\partial \ddot{y}_{mid-span}}{\partial k_f} = \sum_{i=1}^{3} \frac{\partial \ddot{\mathbf{q}}_i}{\partial k_f} \phi_{i,mid-span}$$

$$\frac{\partial y_{mid-span}}{\partial k_f} = \sum_{i=1}^{3} \frac{\partial \mathbf{q}_i}{\partial k_f} \phi_{i,mid-span} \qquad (5\text{-}15)$$

where $\mathbf{q}_i$ is the bridge response for the ith mode.

The sensitivity of k_f to the mid-span acceleration and displacement responses based on the vehicle-bridge system are shown in Fig. 5-6.

(a) Acceleration sensitivity of k_f (b) Displacement sensitivity of k_f
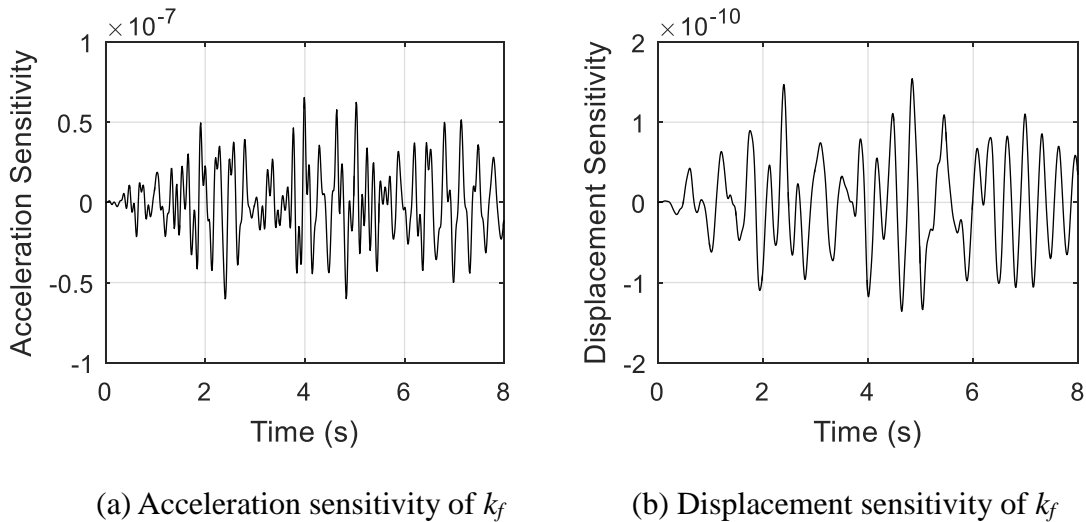
Fig. 5-6. Acceleration and displacement sensitivity of k_f

The above process is repeated for each vehicle parameter and the corresponding sensitivity of the estimates to bridge mid-span responses are calculated. Because the sensitivity in this analysis is a time history, the maximum value of the sensitivity time history is taken as an index to evaluate the parameter sensitivity for the purposes of comparison between the sensitivities of the estimates to each parameter. Moreover, to make the sensitivities of acceleration and displacement comparable, these indices of acceleration and displacement are further normalized by the mean value of the sensitivities to all 10 vehicle parameters, to eliminate the influence from unit magnitude. The index is defined as:

$$S_{a,i} = \frac{\max\left|\partial \ddot{y}_{mid-span}/\partial \alpha_i\right|}{\dfrac{1}{10}\sum_{i=1}^{10}\max\left|\partial \ddot{y}_{mid-span}/\partial \alpha_i\right|}, S_{d,i} = \frac{\max\left|\partial y_{mid-span}/\partial \alpha_i\right|}{\dfrac{1}{10}\sum_{i=1}^{10}\max\left|\partial y_{mid-span}/\partial \alpha_i\right|} \tag{5-16}$$

where $S_{a,i}$ and $S_{d,i}$ are the sensitivity index of bridge mid-span acceleration and displacement response, respectively, against the ith vehicle parameter.

The sensitivity index of each parameter is listed in Table 5-3.

Table 5-3. Sensitivity index of each parameter

Name	m_b	m_f	m_r	I_y	k_f	k_r	k_{tf}	k_{tr}	c_f	c_r
S_a	0.080	4.702	4.977	0.021	0.003	0.003	0.002	0.002	0.096	0.115
S_d	0.514	4.191	4.724	0.095	0.012	0.015	0.001	0.001	0.210	0.237

From Table 5-3, it is observed that the sensitivities of displacement to the vehicle parameters m_b, I_y, k_f, k_r, c_f and c_r are higher than the corresponding sensitivities of

acceleration, while the sensitivities to m_f, m_r, k_{tf}, and k_{tr} were lower. This is due to the fact that the first set of parameters are from the upper vehicle body, whose dominant frequency is lower than the frequency of the bottom tire component. Therefore, the inclusion of bridge displacement, whose main frequency components are in a lower frequency range, increases the sensitivity index of the upper body parameters, making it easier for those parameters to converge.

5.4 Experimental Validation

The bridge pavement roughness estimated in Section 5.1 is used as the excitation source of the passing vehicle, which leads to the coupled vibration of the vehicle-bridge system. The vehicle used for excitation was the same one used for pavement roughness estimation, though in this experiment the vehicle parameters were assumed to be unknown. For the purpose of identifying the vehicle parameters, wireless sensor nodes equipped with Epson M-A351AU accelerometers were installed at the 1/4 span, mid-span, and 3/4 span of the bridge to measure the bridge acceleration response. An additional sensor was placed at each end of the bridge to record the time the vehicle entered and exited the bridge, from which the average vehicle speed on the bridge was estimated. The sensor arrangement is shown in Fig. 5-7. The bridge displacement responses were obtained through the double-integration of the recorded acceleration data after application of a high-pass filter with a cut-off frequency of 0.15 Hz. Because the physical mass of this bridge is available, the modal mass values are obtained from the physical mass and the measured mode shapes in Section 2.3.1
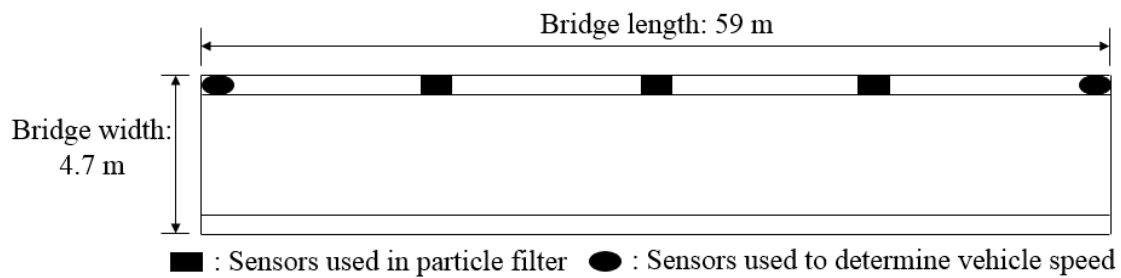
Fig. 5-7. Arrangement of wireless sensor nodes on the bridge

In this section, the parameters of the vehicle, including the vehicle weight, are assumed to be unknown and are identified through the process described in Section 5.2. The initial range of the vehicle mass, expressed as $m_b+m_f+m_r$, is set between 1000 kg to 25 000 kg following a uniform distribution. The vehicle mass was also measured for comparison and its true value was estimated at 1850 kg. The weighing pad is shown in Fig. 5-8.
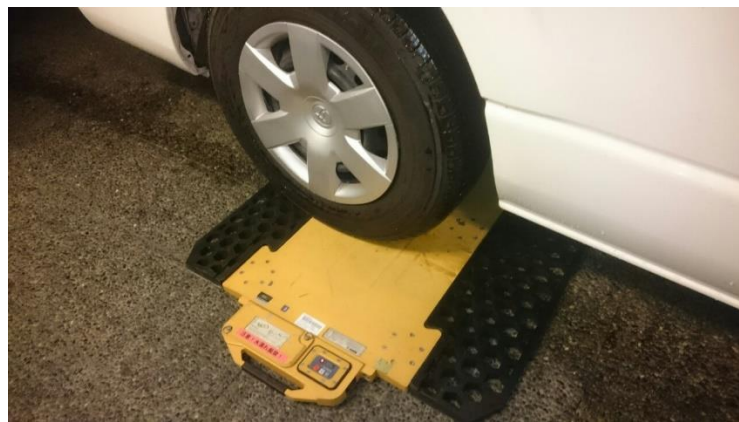
Fig. 5-8. Weighing pad to measure vehicle weight (Rex Corporation)

Four different speeds, 20 km/h, 30 km/h, 40 km/h, and 50 km/h, were used to investigate the speed dependency of the proposed method. For each speed, three separate tests, denoted Test 1, Test 2, and Test 3, were conducted. The estimated mass at each vehicle speed is shown in Fig. 5-8. Only the total mass result is shown as there are no accurate

127

reference values for the other vehicle parameters. For Test 1 at each driving speed, the data was processed first with acceleration only and then with both acceleration and displacement. If bridge displacement is not included, the estimation results are poor compared with cases in which both displacement and acceleration are included.

(a) 20 km/h

(b) 30 km/h
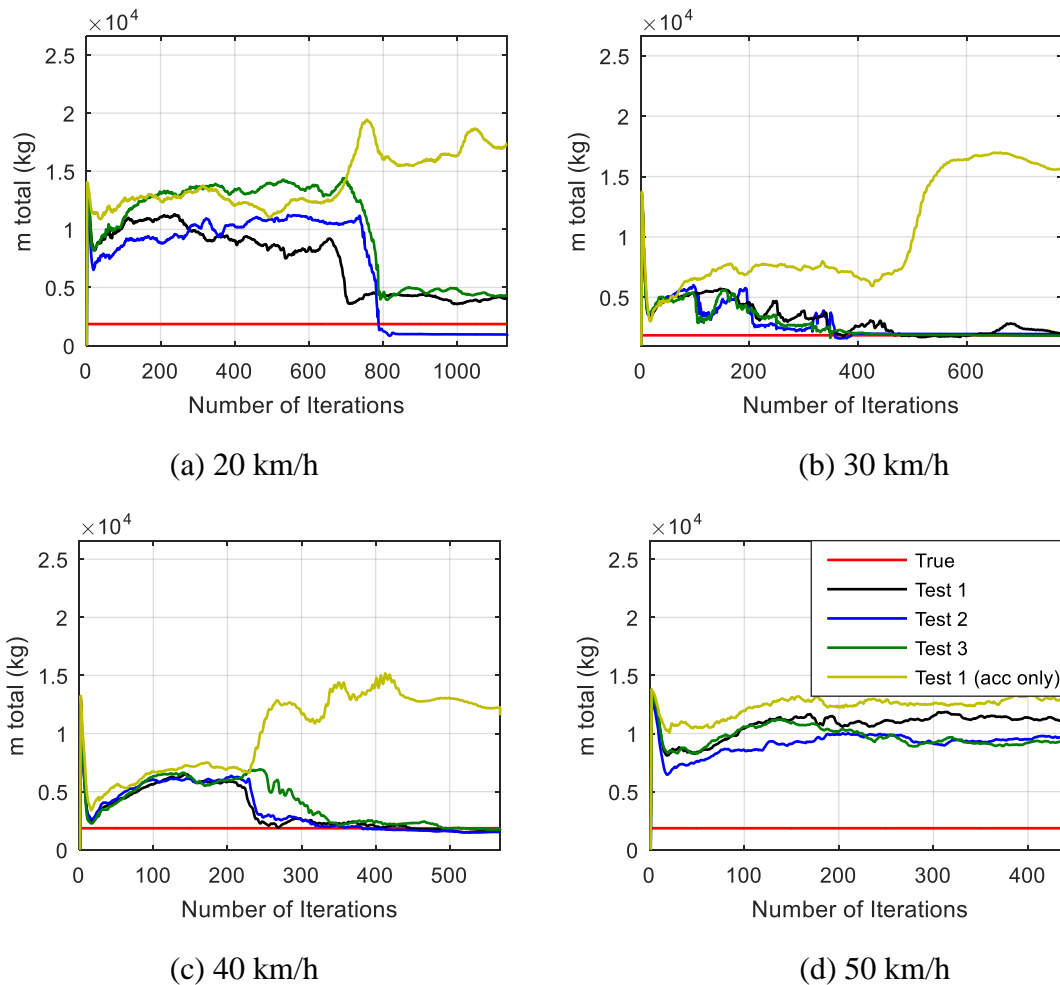
(c) 40 km/h

(d) 50 km/h

Fig. 5-8. Estimated vehicle weight before WGI

As shown in Fig. 5-8, the estimate of vehicle mass for the 30 km/h and 40 km/h speed cases exhibit high accuracy (around or less than 10 % error) while for the 20 km/h and 50 km/h speed cases, large estimation errors were observed. Although the estimation results are poor in these cases, the results are still closer to the true value when compared to the

128

initial range. In an attempt to increase the estimation accuracy in the 20 km/h and 50 km/h speed cases, WGI method is adopted. The results when using the WGI process for the 20 km/h and 50 km/h speed cases after a second repetition of the filtering are shown in Fig. 16.

(a) 20 km/h   (b) 50 km/h
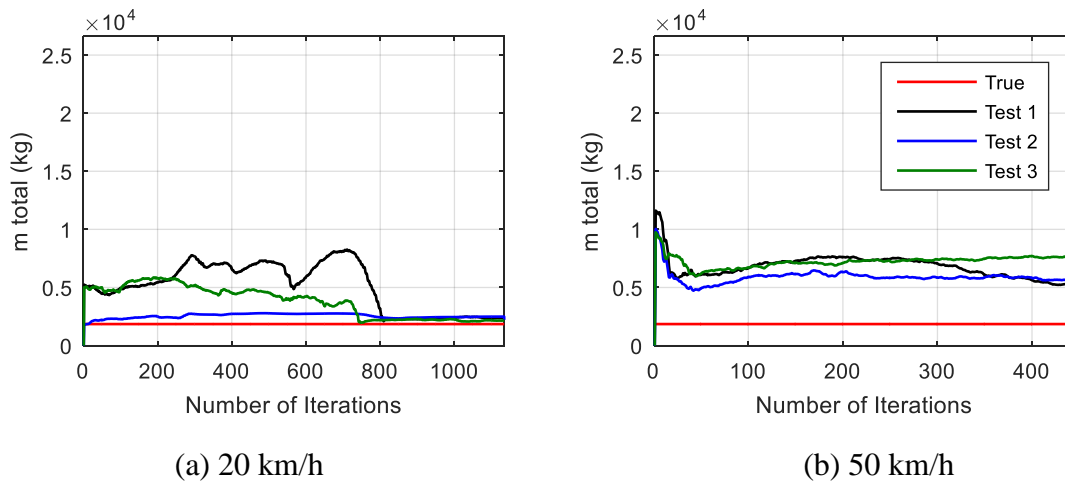
Fig. 5-9. Estimated vehicle weight after second WGI filtering round

The estimation results are noticeably closer to the true value after the second round of filtering. To achieve higher accuracy, the process was repeated several times. The estimation results using the WGI process are shown in Fig. 5-10. For the 20 km/h speed case, around 5 repetitions were required before the estimation result converged to the true value, and 15 repetitions were required for the 50 km/h speed case. In this analysis, when three consecutive repetitions produced estimation results within less than 10% of each other, the mean of these three values was taken as the final estimation result. This repetition method was also applied to the 30 km/h and 40 km/h speed cases to determine the converged values. The final results of each case are shown in Table 5-4.

(a) 20 km/h   (b) 50 km/h
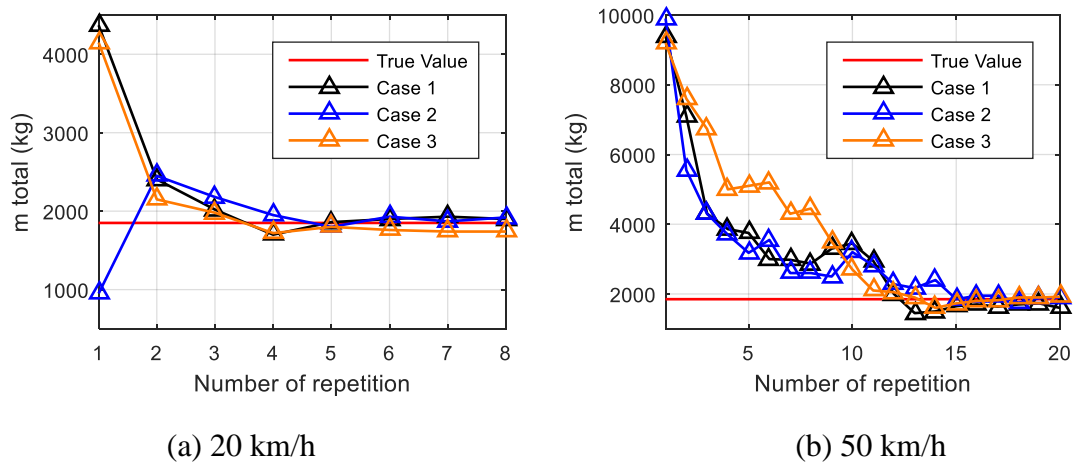
Fig. 5-10. Estimated vehicle weight after each WGI repetition

Table 5-4. Estimation result and error

Vehicle Speed		20 km/h	30 km/h	40 km/h	50 km/h
Test 1	Value	1910 kg	1975 kg	1650 kg	1677 kg
	Error	+6.0 %	+6.7 %	-10.8 %	-9.4 %
Test 2	Value	1906 kg	1948 kg	1630 kg	2000 kg
	Error	+3.1 %	+5.3 %	-11.9 %	+8.1 %
Test 3	Value	1746 kg	1825 kg	1760 kg	1906 kg
	Error	-5.6 %	-1.3 %	-4.9 %	+3.1 %

From Table 5-4, it can be seen that the largest error observed was 11.9 %. Note that for each case, the estimation error, as well as the number of repetitions required to converge, is not a deterministic value due to the stochastic nature of the particle filter method. The error and the number of WGI repetition are also affected by the values of the randomly generated particles at the beginning of each repetition. As indicated by the relatively small value of the largest error (11.9 %), the proposed method exhibits good accuracy when

130

estimating passing vehicle weight.

5.5 Summary

In this chapter, an algorithm for vehicle parameter identification from bridge responses is proposed. The bridge pavement roughness, which is the input excitation of the vehicle-bridge coupling system in the vertical direction, is assumed to be known based on the method proposed in Chapter 4. Bridge acceleration responses at certain places on the bridge are measured as the output of the system and included in the observation vector. The vehicle parameters, including the vehicle body weight, are determined based on the estimated bridge pavement roughness with a consideration of the vehicle-bridge interaction. A simulation was conducted to test the feasibility of the proposed method. High accuracy and robustness, even under the influence of simulated observation noise and modelling errors, were observed in the results. The method does not require the calibration process with the reference weight truck. The proposed method was further validated through a field measurement conducted with a steel box-girder bridge.

Chapter 6 Vehicle Moving Dynamic Load Estimation from Bridge Acceleration Responses

6.1 Overview

The identification of the dynamic part of the moving vehicle load is addressed in this Chapter. Although most bridge owners are interested in the vehicle static weight or sometimes the axle weight of the passing vehicles, the dynamic part of the moving vehicle is also important as the vehicle force on the bridge is not a constant moving load. Because the vehicle system has its own dynamic properties, e.g., stiffness and damping, the bridge pavement roughness which excites the vehicle system in the vertical direction will lead to the vehicle vibration. In return, the vehicle tire forces on the bridge deck fluctuate over time, which is dependent on both time and space.

The information of the dynamic part of the vehicle tire forces is necessary in at least two aspects. In the first place, depending on the bridge pavement condition, the amplitude of the tire force can be much higher than vehicle's static load due to the dynamic amplification factor. Only considering the static part of the vehicle load will increase the risk on the safety as well as the serviceability of the bridge system. On the other hand, the dominant frequency of the dynamic load needs to be monitored. If most vehicles passing across this bridge have the dominant frequency close to the bridge fundamental frequency, the risk of bridge resonance phenomenon becomes higher. Therefore, the vehicle moving dynamic load needs to be monitored for the safety of the bridge system.

133

In this chapter, a method for the vehicle moving dynamic load identification using bridge acceleration responses is investigated. Similar to previous chapters, the particle filter method is adopted as the main algorithm. The front and the rear tire dynamic forces are included in the state vector, together with another parameter indicating the passing lane of the vehicle. The vehicle dynamic forces as well as the vehicle passing lane are the target to be estimated in this chapter. Numerical simulations demonstrate that the vehicle moving dynamic force as well as the vehicle passing lane is estimated with high accuracy and robustness against observation noise. The problem of distinguishing the front and the rear axle dynamic load is discussed and it is found that the wheelbase value has a direct influence on the axle load identification. Finally, this method is validated through field measurement at the bridge in Yokohama. The resulting estimate of the vehicle moving dynamic load agrees well with the one estimated from the vehicle responses using the method proposed in Chapter 3, whose accuracy and robustness has been proved. The practicality of the proposed method is thus demonstrated.

6.2 Implementation of Particle Filter on Moving Load Identification from Bridge Responses

In this section, the particle filter method is used to directly identify the moving dynamic load from bridge responses. Similar to the previous chapter, the bridge response terms are included in the state vector as well as the vehicle front and rear tire forces. Moreover, a parameter d, defined as the distance between the vehicle's passing route and one edge of the bridge, is also included in the state vector, for the purpose of vehicle passing lane detection, as shown in Fig. 6-1.
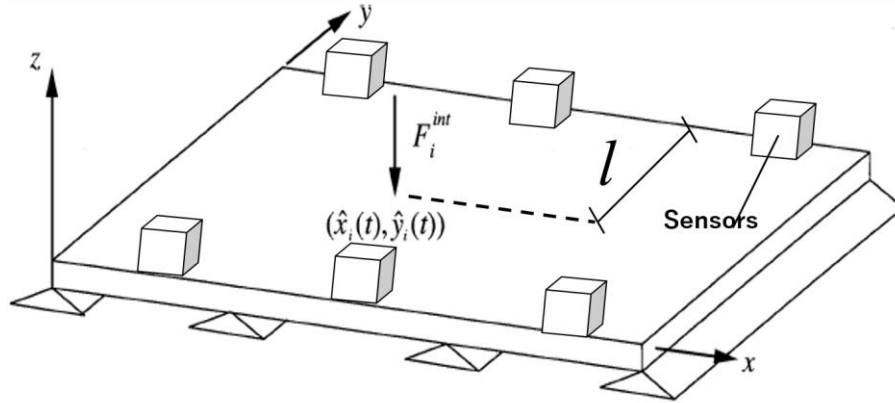
Fig. 6-1. Moving load identification from bridge responses (Zhu and Law, 2001)

The state vector of this problem is shown as:

$$\mathbf{X}_k = \begin{bmatrix} \mathbf{q}_k & \dot{\mathbf{q}}_k & \ddot{\mathbf{q}}_k & F_{f,k} & F_{r,k} & l_k \end{bmatrix} \tag{6-1}$$

where $\mathbf{q}$ is the vector including the modal coordinate of each mode of the bridge, F_f and F_r indicate the vehicle front and rear dynamic tire force, and l is the distance between the vehicle passing route and one edge of the bridge, as shown in Fig. 6-1.

For the particle evolution, the bridge responses terms, including $\mathbf{q}$ and its first and second order derivatives, evolve through Eq. (4-6), where the relation between response terms of two consecutive steps is described. On the other hand, due to the same reasons stated in Chapter 3, i.e., the complexity of modelling vehicle dynamic tire forces, F_f and F_r in the state vector evolve based on a random walk model, as repeated here in Eq. (6-2).

$$F_{f,k+1} = F_{f,k} + \eta_{f,k}$$
$$F_{r,k+1} = F_{r,k} + \eta_{r,k} \tag{6-2}$$

where η_f and η_r are independent zero-mean Gaussian processes governing the time evolution of the front and rear tire forces, respectively.

For parameter l, the particles of time step $k+1$ have the same l values as time step k except for the system error term, as described in Eq. (6-3). The reason is that in this study, it is assumed that the vehicle does not change its passing lane due to the passage of the bridge. Considering that the time of the passage is usually short, this is a reasonable assumption.

$$l_{k+1} = l_k + \omega_k \tag{6-3}$$

where ω_k is the system error term, mainly to prevent the particles getting frozen in the particle filtering process and to compensate for the error induced by time discretization.

For the observation equation, bridge acceleration responses at the position of both left and right edges of the bridge are included. For the case shown in Fig. 6-1, where the bridge acceleration at mid-span, 1/4-span, and 3/4-span are measured, the observation equation is shown as:

$$\mathbf{Y}_k = \begin{bmatrix} \ddot{y}_{L,1/4} & \ddot{y}_{L,1/2} & \ddot{y}_{L,3/4} & \ddot{y}_{R,1/4} & \ddot{y}_{R,1/2} & \ddot{y}_{R,3/4} \end{bmatrix} \tag{6-4}$$

where the subscript 'L' and 'R' indicates the 'left' and 'right' edge of the bridge.

6.3 Numerical Example

A numerical example is given in this section. The implementation process described in Section 6.2 is conducted here. The algorithm is first verified for the case of without sensor noise, followed by the error analysis considering sensor noise, vehicle speed, the ratio of vehicle wheelbase and bridge length, and the error of bridge modal mass.

6.3.1 Verification without Noise and Error

The algorithm proposed in Section 6.2 is verified through a numerical example in the section. A full-car model is used to model the vehicle passing over the bridge with an eccentricity while a two-span continuous plate model is adopted as the bridge model. The bridge dynamic properties, including the natural frequencies, damping ratios, and the corresponding mode shapes, are extracted from the bridge in Yokohama, whose details are described in Section 2.3.3. The bridge deck roughness is determined as the same as the one used for Section 3.2.3.

The bridge acceleration responses at the locations shown in Fig. 6-2 are calculated as the measured responses in this numerical example.
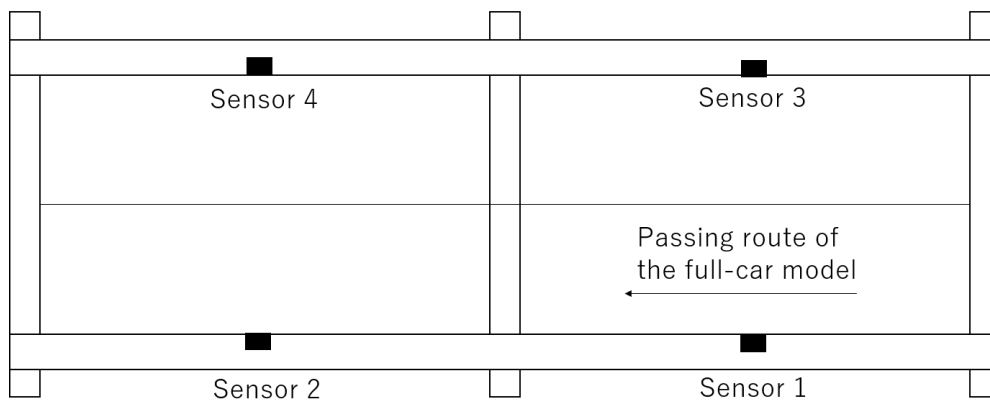
Fig. 6-2. Locations of acceleration responses used in the numerical example

The parameters of the full-car model used in this simulation are listed in Table 6-1. The bridge properties, including natural frequencies, damping ratios, and mode shapes, are extracted from a real bridge, which served as the target bridge in the field measurement described in this chapter in later sections.

Table 6-1. Full-car model parameters

m_b(kg)	m_f(kg)	m_r(kg)	I_x(kg/m^2)	I_y(kg/m^2)	k_f(N/m)	k_r(N/m)	k_R(Nm/rad)
840	53	76	820	1100	10000	13000	10000
c_f(Ns/m)	c_r(Ns/m)	k_{tf}(N/m)	k_{tr}(N/m)	a_1(m)	a_2(m)	b_1(m)	b_2(m)
2500	2500	200000	200000	1.4	1.45	0.7	0.75

In this example, there are in total four forces moving on the bridge, i.e., front left tire force, front rear tire force, rear left tire force, and rear right tire force. As a result, the bridge responses are calculated based on four moving forces acting simultaneously on the bridge with a distance delay. However, in the inverse moving force identification, the front left tire and the front rear tire are considered as one force acting in between the front left and front right tires, while the rear left and the rear right tire are also considered as one force acting in between the rear left and rear right tires. The reason for this simplification is explained by the fact that in the bridge load condition assessment, only axle weight and axle dynamic load is of interest without distinguishing the left and right tires.

The bridge acceleration responses at each of the mid-span are calculated as 'measured' responses and are put into the observation vector. The constant vehicle driving speed is set as 20 km/h and is assumed to be known. The calculated bridge acceleration responses at each sensor location are shown in Fig. 6-3.
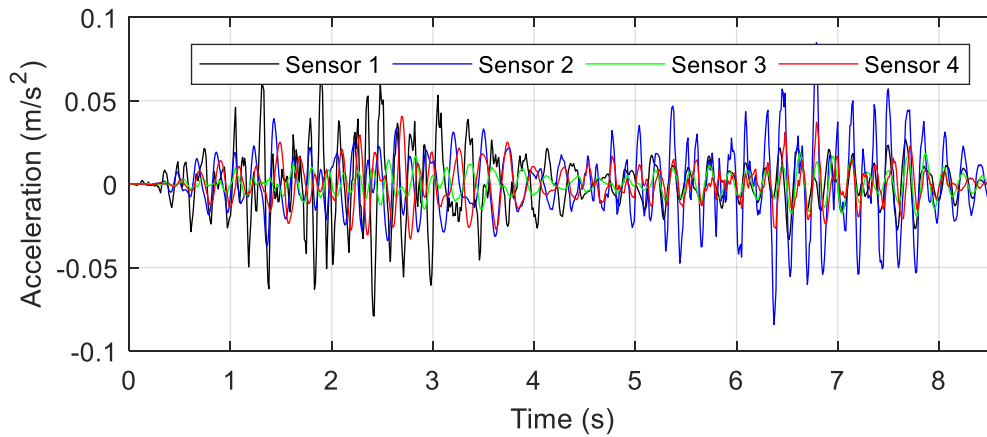
Fig. 6-3. Calculated bridge responses at each sensor location

While the left and right tire forces are not distinguished in this study, the front and rear tire forces are reflected in this algorithm, as separately listed in the state vector shown in Eq. (6-1). However, certain requirement should be satisfied if the front and rear tire forces are to be distinguished. Details are discussed in Section 6.3.4, where the ratio between the vehicle wheelbase and the bridge length is introduced as an important index. In the results shown here, only the summation of front and rear tires are addressed following the implementation process of particle filter described in Section 6.2. The vehicle dynamic tire force is shown in Fig. 6-4 (a) and (b), in the time and frequency domain, respectively.

(a) Estimation in the time domain

139
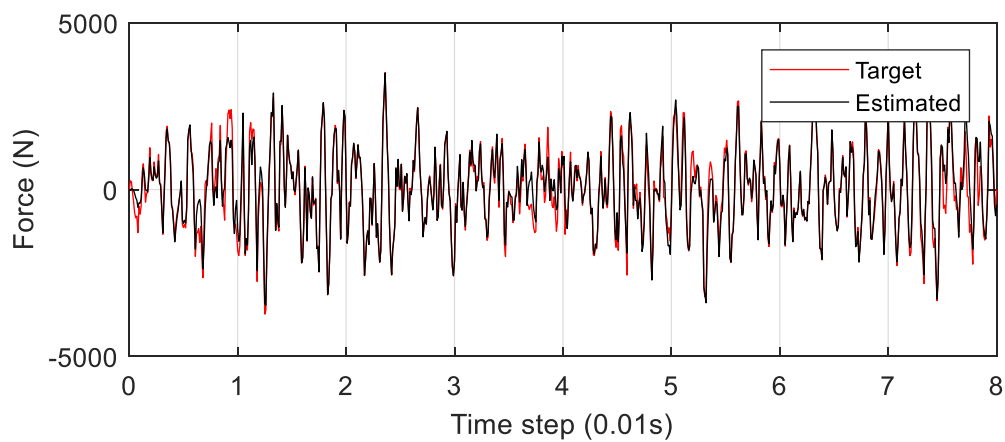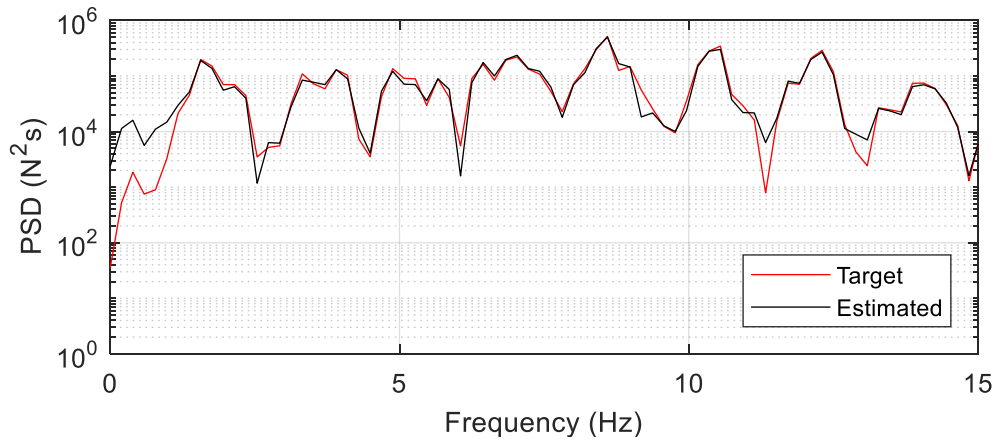
(b) Estimation in the frequency domain

Fig. 6-4. Moving dynamic force identification result without noise and error

As stated in Section 6.2, the vehicle passing route is also detected by identifying the parameter l, which is defined as the distance between the vehicle's passing route and one edge of the bridge. Fig. 6-5 shows the converging process of this parameter. Because the left and the right tires are not distinguished, there is no real target reference for this value. However, this parameter converges to a value in between the left tire path and the right tire path after a few steps, indicating that the vehicle passing route is identified correctly.
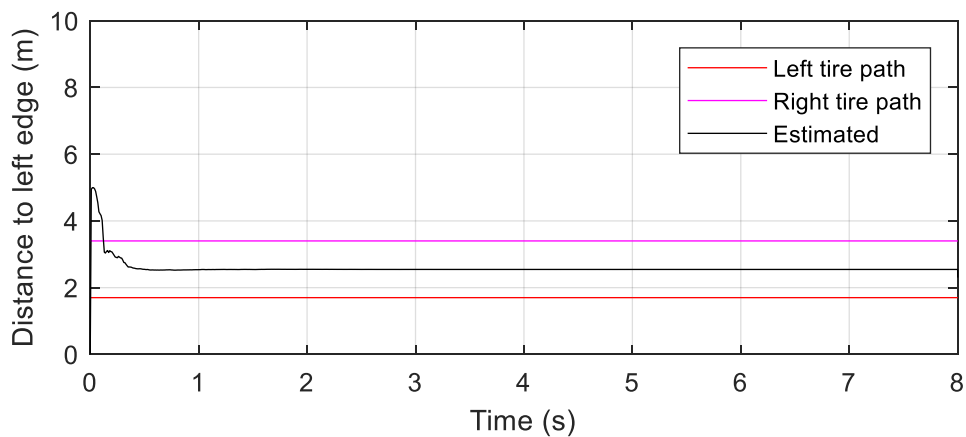
Fig. 6-5. Converging process of vehicle passing route parameter

From Fig. 6-4 and Fig. 6-5, the total dynamic forces are estimated correctly in both the time and the frequency domain as well as the vehicle passing lane, for the case without the influence from noise and errors. The proposed algorithm is thus verified. In the following sections, the robustness against sensor noise and other error terms are discussed through more numerical examples.

6.3.2 Influence from Sensor Noise

In this section, the influence from the sensor noise is checked. Artificial white noise is added in the calculated bridge acceleration responses shown in Fig. 6-3. Similar framework of the estimation process is conducted. The estimated dynamic load in the time and frequency domain are shown in Fig. 6-6 (a) – (b) together with the lane estimation result in Fig. 6-6 (c). The estimation errors are listed in Table 6-2.
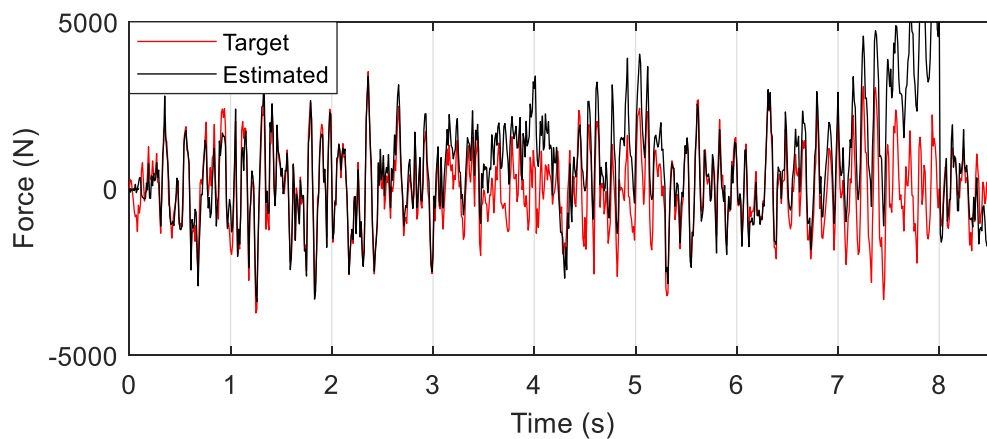
(a) Estimation in the time domain
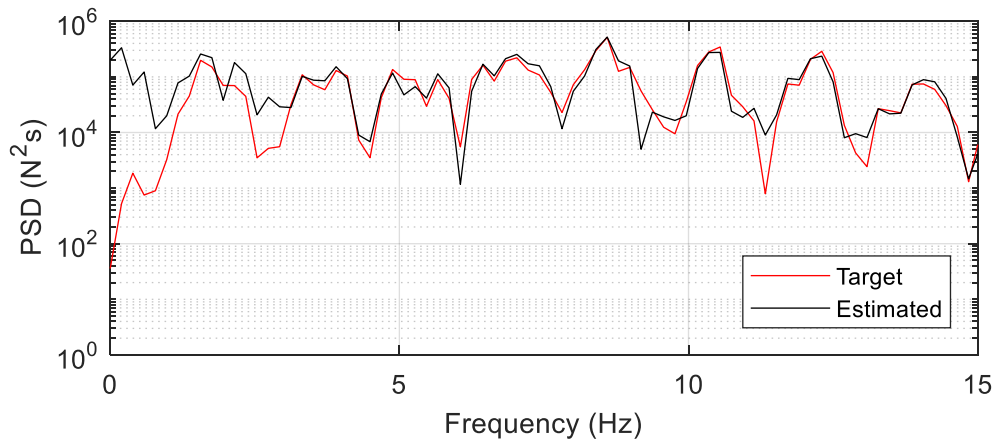
(b) Estimation in the frequency domain
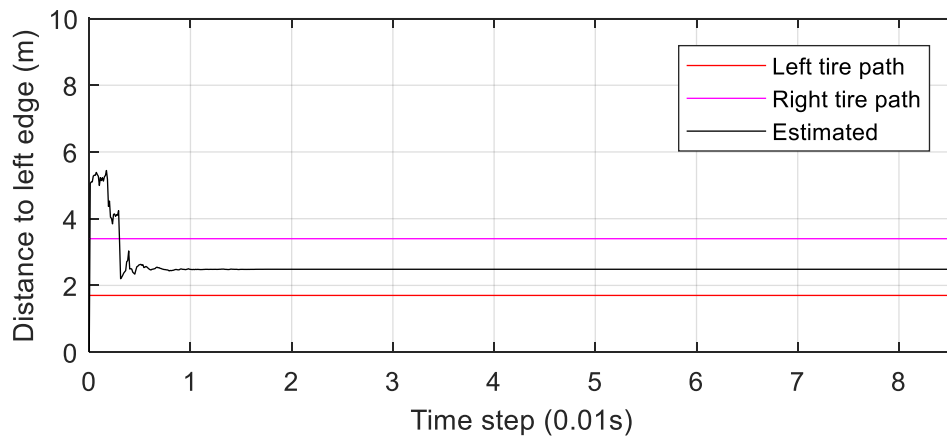
(c) Estimation of the vehicle passing lane parameter

Fig. 6-6. Estimation results with 10 % sensor noise

Table 6-2. Comparison of estimation results with and without sensor noise

Case	Without sensor noise	With sensor noise
Force error	11.46 %	34.68 %
Lane estimation value	2.54 m	2.53 m

From Fig. 6-6 and Table 6-2, it can be concluded that the proposed algorithm has good

robustness against sensor noise. Although an increase in the estimation error is observed

from 8.47 % to 34.68 %, this is mainly due to the large error in the middle, where a middle support is located, and at the ends of the bridge. These areas are defined as 'insensitive area', where the vehicle loads do not lead to large bridge mid-span responses. These 'insensitive areas' will be observed again in the experimental validation described in Section 6.4.

6.3.3 Influence from Vehicle Speed

The moving dynamic load identification process is repeated for different driving speeds. The identification error of the moving dynamic load is summarized in Table 6-3. These results are based on simulation without sensor noise to avoid possible influence on the results from the sensor noise.

Table 6-3. Vehicle total mass identification errors for different driving speed cases

Speed	20 km/h	30 km/h	40 km/h	50 km/h
Error	16.37 %	11.46 %	29.88 %	42.03 %

From Table 6-3, the smallest error occurs when the driving speed is around 30 km/h. As the driving speed becomes higher, a decreasing trend of the accuracy is observed, mainly due to the time discretization error in the dynamic response calculation procedure. For the lower vehicle speed at 20 km/h, the error is slightly larger than the error at 30 km/h. This is explained by the fact that lower driving speed leads to smaller bridge acceleration responses, which may require a different parameter setting in the particle filter algorithm.

143

6.3.4 Influence from Ratio of Vehicle Wheelbase and Bridge Span

In the numerical example shown in previous sections, the bridge vehicle wheel-base is set as 2.85 m, which is the normal case for commercial light vehicles. Although the total force is estimated with good accuracy, the front and rear axle loads are not distinguished accurately. The front and rear force estimation results are expressed in Fig. 6-7 (a) – (b), respectively.
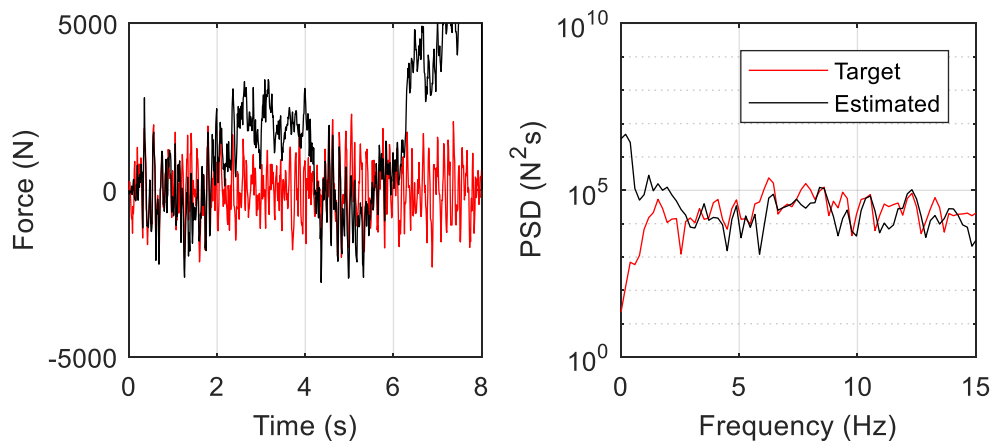
(a) Front axle load estimation for 2.85-meter wheelbase
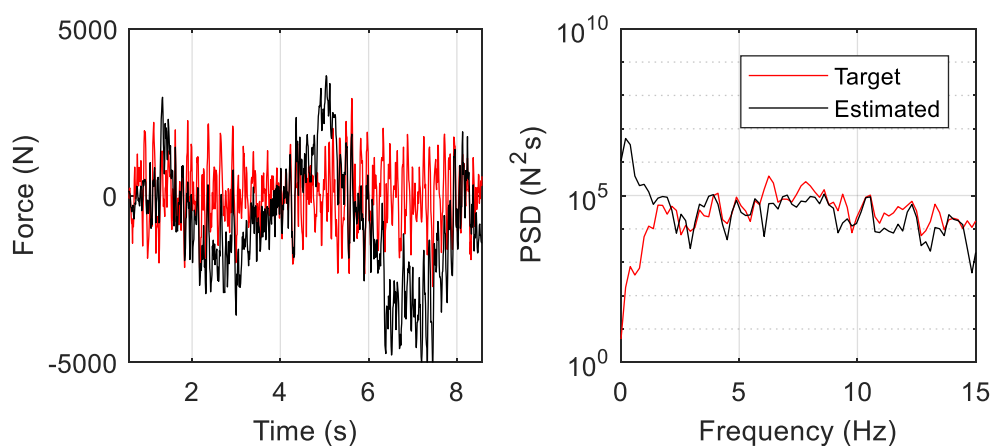
(b) Rear axle load estimation for 2.85-meter wheelbase

Fig. 6-7. Front and rear load estimation for 2.85-meter wheelbase

In Fig. 6-7 (a) and (b), it is observed that neither the front load nor the rear load is estimated correctly. However, it is observed that when the front axle force is over-estimated, the rear axle force is under-estimated at the corresponding time section, leading to a balanced total force estimation. This phenomenon is due to the fact that compared to the bridge length, the vehicle wheelbase value is relatively small that the front and rear axle load acting on the bridge is recognized as one force by the algorithm. If the wheelbase is increased to 4.85 m, the front and rear axle load is better distinguished, as shown in Fig. 6-8 (a) – (b).
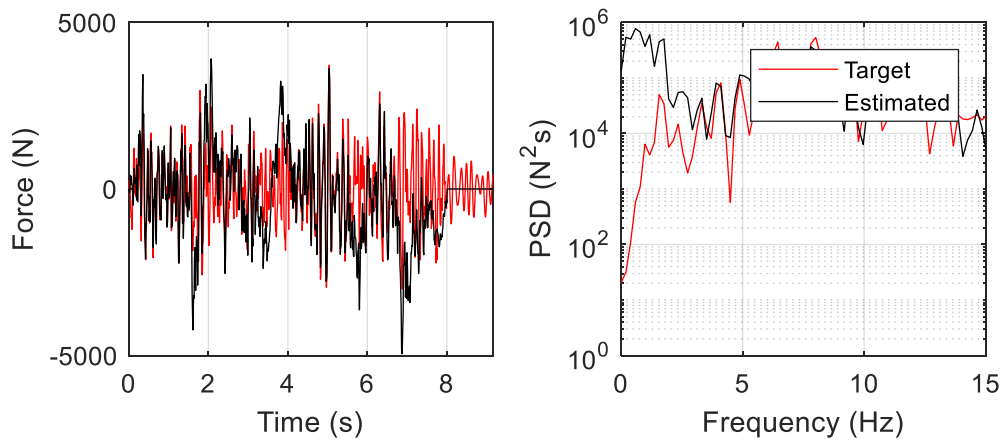
(a) Front axle load estimation for 4.85-meter wheelbase
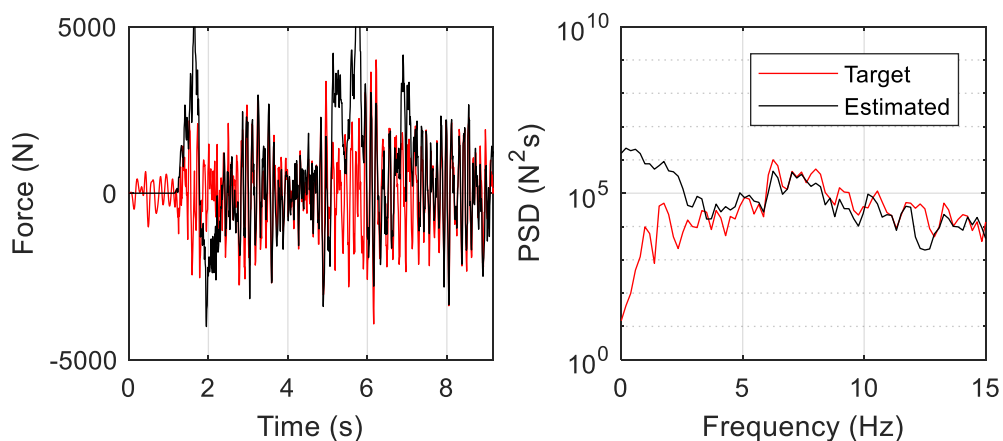
(b) Rear axle load estimation for 4.85-meter wheelbase

Fig. 6-8. Front and rear load estimation for 2.85-meter wheelbase

The relation between the wheelbase value and the front force estimation error is shown in Fig. 6-9. An obvious decreasing trend is observed, indicating that a large wheelbase value can lead to a better distinguish of the front and rear forces.
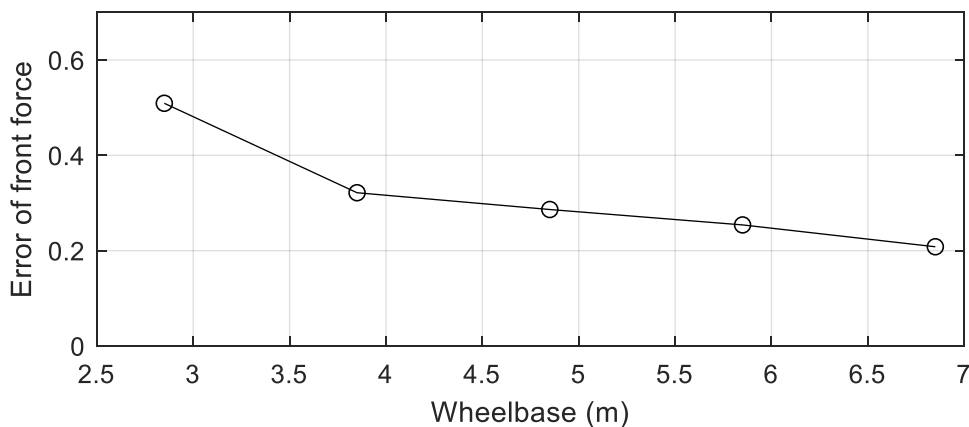
Fig. 6-9. The decreasing trend of front force estimation error with wheelbase

For most light vehicles, the wheelbase value is usually less than 3 m, making it difficult to distinguish the front and rear load. However, from the perspective of global vibration, it is not important to distinguish the front and the rear load. For the vehicles with larger wheelbase values, e.g., buses or trucks, which usually have wheelbase around 5 – 6 meters, the front and rear tire forces can be roughly distinguished by the proposed method.

6.3.4 Influence from Bridge Modal Mass Value Error

The influence from the errors of bridge modal mass values is discussed in this section. In the bridge weigh-in-motion as well as moving load identification system, the bridge serves as the weighing scale of the vehicles. Therefore, it is natural that the parameter errors of this weighing scale lead to errors of the estimation.

In the decomposed equations of motion of the bridge system shown in Eq. (2-22), the vehicle force acting on the bridge is related with the bridge modal parameters. Theoretically speaking, the errors in the bridge parameters will be proportionally reflected in the estimated tire forces, which is proved by a numerical example where the bridge modal mass values are increased by 20 % in the inverse particle filter problem. The bridge modal stiffness and modal damping values are increased by the same proportion assuming unchanged natural frequencies and damping ratios. The estimation results are shown in Fig. 6-10.
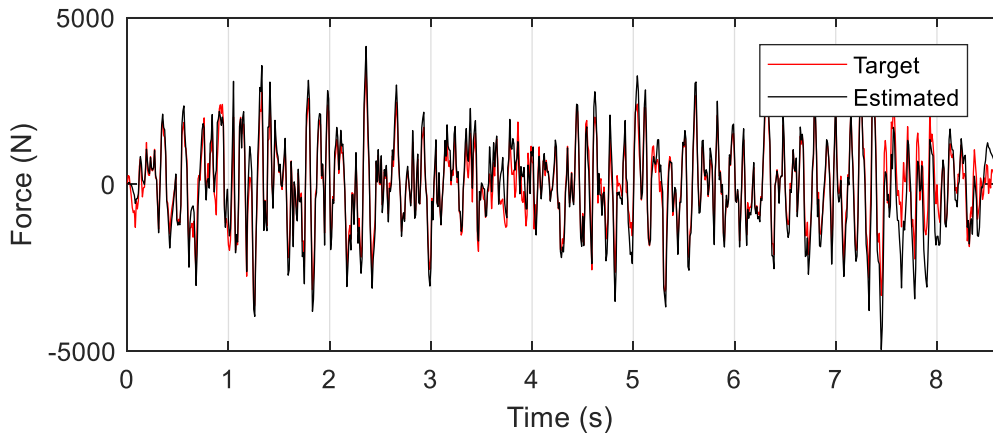
(a) Force estimation in the time domain with bridge modal mass error
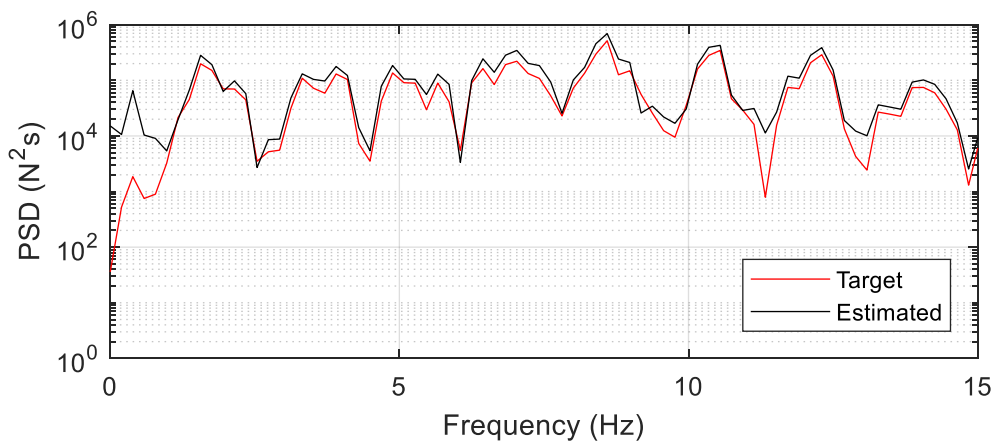
(b) Force estimation in the frequency domain with bridge modal mass error

Fig. 6-10. Force estimation results with bridge modal mass error

From Fig. 6-10, it is observed that the estimation values become higher than the target due to the existence of the bridge modelling errors. Although with some fluctuations, the estimated peak values shown in Fig. 6-10 (b) are 17.85 % (close to 20 %) higher than the target, showing a proportional inaccuracy induced by modal mass values. However, from Chapter 3, the bridge modal mass estimation error is usually less than 10 %. Therefore, the error induced by bridge modelling error is limited within the range of less than 10 %.

6.4 Experimental Validation at the Bridge in Yokohama

To validate the proposed algorithm, a field measurement was conducted at the bridge in Yokohama. Overview of this bridge and its properties are shown in Section 2.3.2.

A Honda Step-wagon car, shown in Fig. 6-11, is chosen as the test vehicle to excite the vibration of the bridge. As there is no reference data for the real dynamic tire force, sensors were installed on the vehicle as shown in Fig. 6-12 to measure vehicle responses when passing across the bridge, which are then used to give tire force values using the method developed in Chapter 3 and are used as the reference data to be compared with the dynamic forces estimated from bridge responses.

Fig. 6-11. Test vehicle on Yokohama Bridge (Honda Corporation)

Fig. 6-12. Sensors installed on the test vehicle

For the purpose of using the estimation from vehicle as the reference, the measured vehicle responses and the bridge responses need to be synchronized. This is achieved by using JAE sensors. As seen from Fig. 6-13, one JAE sensor was attached next to the wireless accelerometer on the bridge, while another JAE sensor was attached next to the iPod sensor on the vehicle shown in Fig. 6-12. The JAE sensors on the bridge and on the vehicle share the same time system. In this way, the wireless sensor on the bridge and the iPod sensors on the vehicle are synchronized.

The bridge responses at the middle of each span, i.e., left and right edge of each span, were measured to be included in the observation vector shown in Eq. (6-1). The reasons of choosing mid-span responses are explained by the bridge mode shapes shown in Fig. 2-8. As can be seen in the figure, all the four modes have their peak values at each of the mid-span.

Fig. 6-13. Accelerometers on Yokohama Bridge

(Sonas Corporation and JAE Corporation)

In the experiment, the sensor-equipped vehicle was driven across the bridge three times at each speed for each direction. The driving speeds were chosen as 20, 30, 40, and 50 km/h. In total, 24 driving tests were conducted. Following the process described in Section 6.2, the vehicle moving dynamic tire forces are estimated from bridge responses. One typical result for each driving speed is shown in Fig. 6-14 (a) – (d).
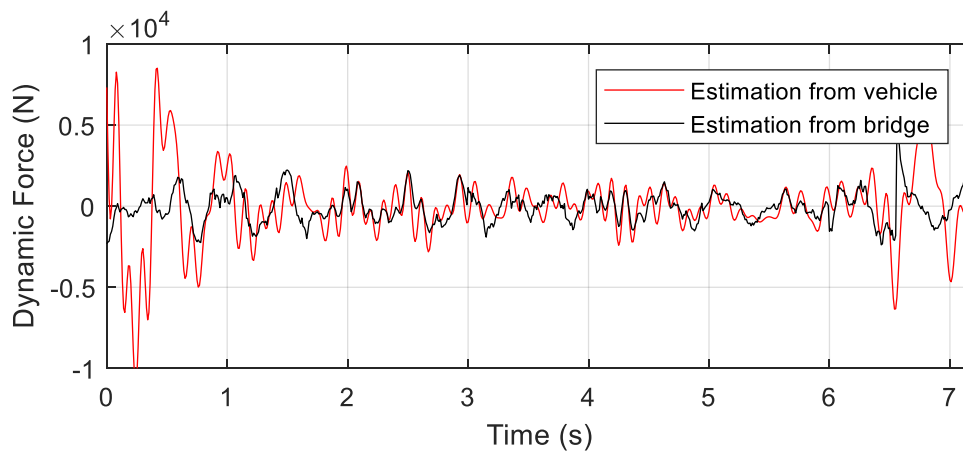
(a) 20 km/h
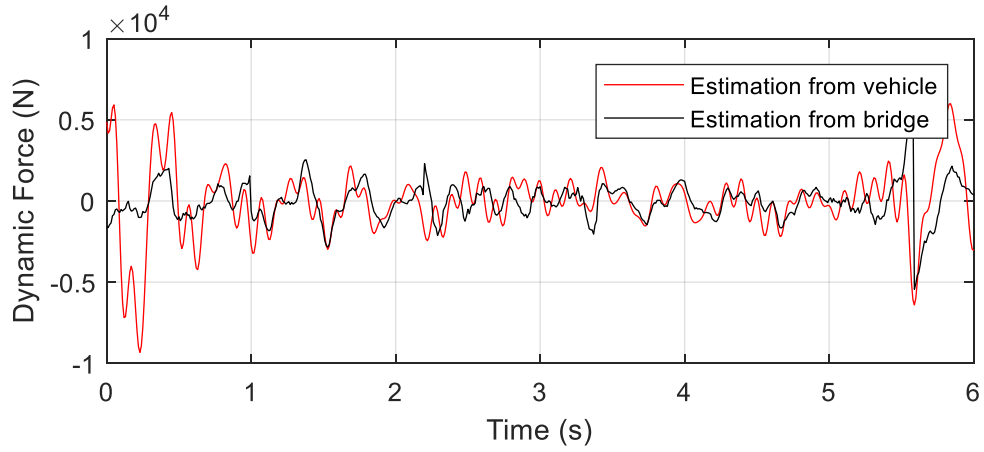
(b) 30 km/h
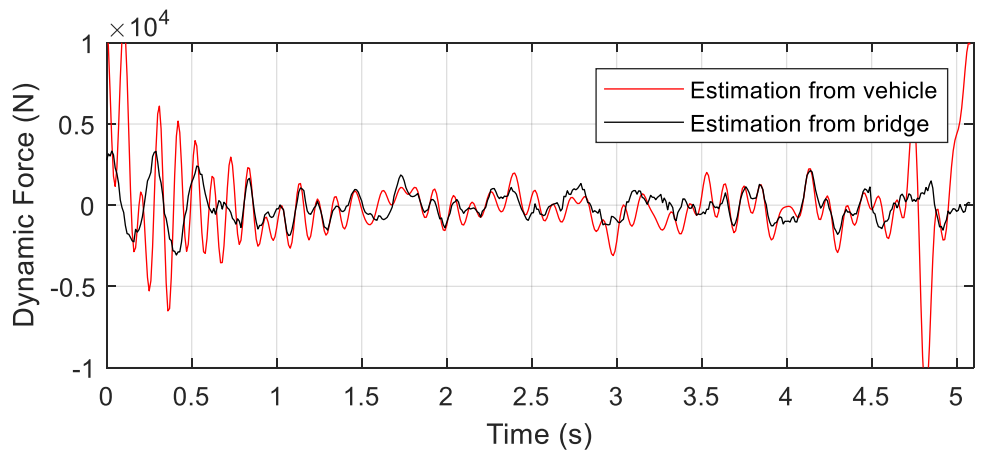
(c) 40 km/h
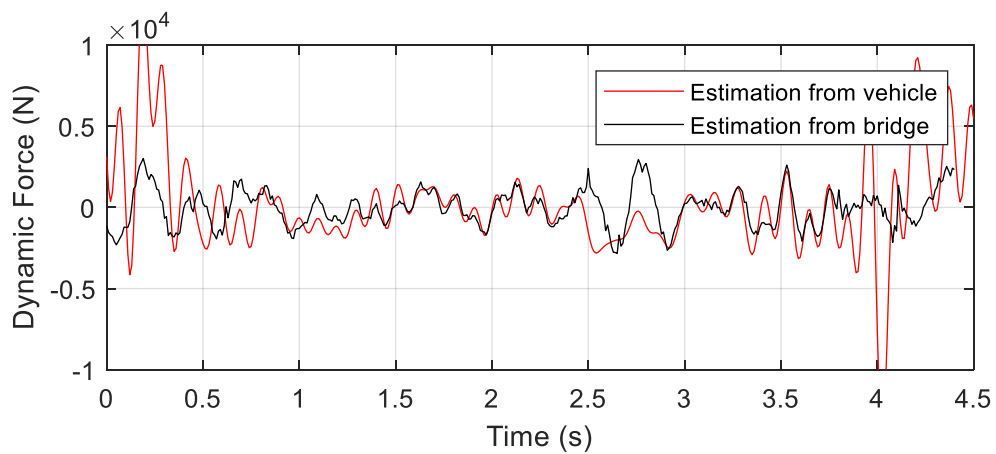
(d) 50 km/h

Fig. 6-14. Typical estimation results for each driving speed

In these figures, inaccuracy at both ends of the bridge and around the middle support is observed, which are known as 'insensitive area', because of the low sensitivity of the bridge mid-span responses. At the ends of the bridge, large force values appear due to the joints. However, these large values were not captured by the estimation from bridge responses, because the force around the end of the bridge does not give significant bridge mid-span responses. The inaccuracy observed around the middle support is explained by the same reason.

The estimation accuracy of Fig. 6-14 is evaluated. The criteria of evaluating the error shown in Eq. (6-22) is not adopted here, with the reason that the dynamic forces are zero-mean, which may lead to large error by the values around zeros. However, those values that are close to zero does not have large influence on the bridge due to their small values. Therefore, only the peak values in the time histories are extracted and compared, as shown in Fig. 6-15. In the time history shown in Fig. 6-14, if the time interval between the peak in the estimation and the peak in the reference is less than 0.05 s, they are considered as one peak and is picked up to Fig. 6-15.
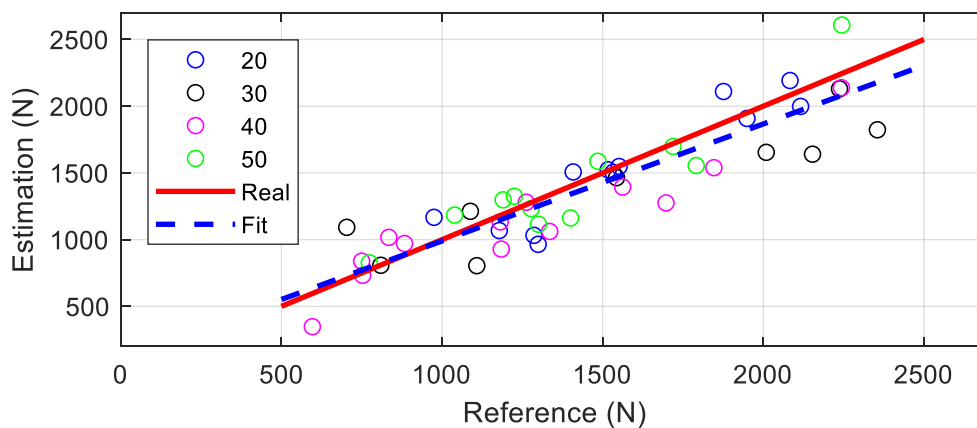
Fig. 6-15. Comparison of reference and estimation on peak values of the time history

In Fig. 6-15, the horizontal axis corresponds to the reference values from the estimation of the vehicle responses, while the vertical axis corresponds to the estimation from bridge responses. Each test is represented by a circle, whose reference and estimation values are shown by its coordinates in the two axes. Ideally, all the circles should be exactly along the line representing $y = x$ in the figure. However, due to the estimation errors, the circles are scattered around the $y = x$ line. A new line with the formation of $y = kx + b$ is fit and shown together in the figure, whose expression is shown in Eq. (6-5).

$$y = 0.88x + 113.23 \qquad (6\text{-}5)$$

where k is fit to be 0.88 and b is 113.23.

The lane information was simultaneously detected. Typical results for three tests of 30 km/h are shown in Fig. 6-16. In this case, the lane parameter l converges at 3.5 – 4 m. Note that the total width of the bridge is 10 m and there are two lanes on the bridge. Therefore, this estimation results indicates that the vehicle passing lane is correctly estimated. The converging process of the lane parameter l for other driving speeds cases is similar to the one shown in Fig. 6-16.
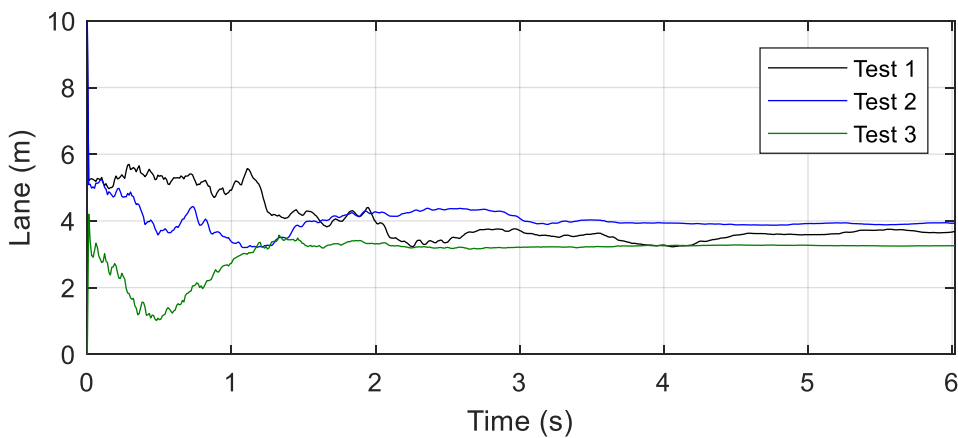
Fig. 6-16. Typical results of lane detection for 30 km/h cases

The estimation results are also checked in the frequency domain. Note that in each vehicle passage of the bridge, the passing time is usually limited within the range of 4 – 8 seconds. If the insensitive areas are considered, the 'effective' passing time becomes more limited, which is not sufficient for PSD analysis. Therefore, the estimated time history of the vehicle moving dynamic load of the total 24 tests are connected in the time domain after removing the parts corresponding to the 'insensitive areas', and is then used to calculate the PSD, which is shown in Fig. 6-17 together with the reference value.
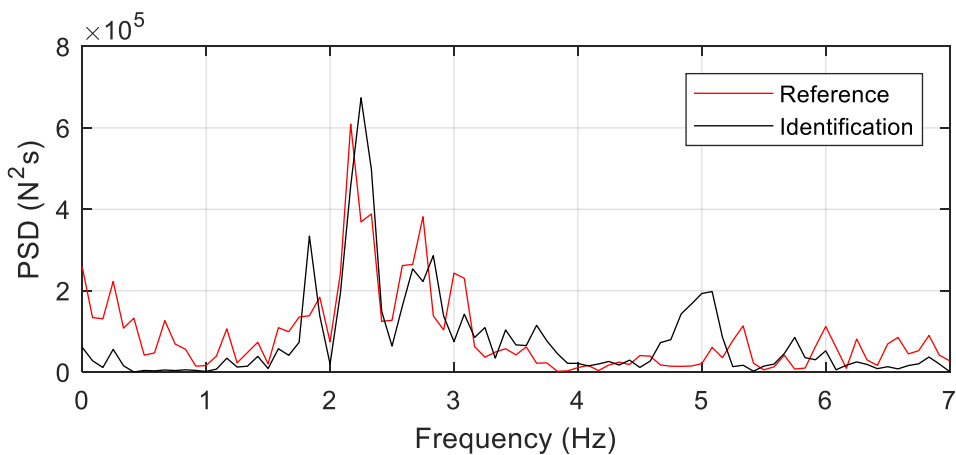
Fig. 6-17. The estimation in the frequency domain

From the reference spectrum in Fig. 6-17, the dominant frequency of the passing vehicles is shown to be 2.25 Hz, which is roughly reflected in the identified spectrum from the bridge responses. Note that this frequency is not close to neither of the bridge natural frequencies listed in Table 2-2. The load condition of this bridge, is suffering from the moving vehicle load with the dominant frequency of 2.25 Hz, which is determined by many factors including bridge pavement roughness, properties of the bridge, and properties of the vehicles passing across this bridge.

The robustness of the proposed algorithm is checked by calculating the error terms following the definition of Eq. (3-22), which are listed in Table 6-4.

Table 6-4. Estimation errors of all tests

Vehicle Speed	20 km/h	30 km/h	40 km/h	50 km/h
Test 1	10.02 %	14.82 %	17.28 %	9.12 %
Test 2	9.22 %	15.13 %	16.56 %	18.49 %
Test 3	14.16 %	16.64 %	10.36 %	19.34 %

From Table 6-4, it is observed that the estimation error of the peak values in the time history are less than 20 %.

6.5 Summary

In this chapter, a moving dynamic force identification technique is proposed by implementing the particle filtering technique. The vehicle front and rear tire dynamic forces are estimated from bridge acceleration responses at certain locations. Numerical examples show that the summation of the front and rear tire forces can be estimated with a good accuracy even when the sensor noises exist. For the vehicles with larger wheelbase, the front and rear tire forces can be distinguished, if needed. The influence from the driving speed is investigated, which shows that the estimation accuracy has decreasing trend for higher driving speeds, but still within the satisfactory range. A field measurement further validates the feasibility of the proposed method, where the dynamic force time history estimated from the bridge responses are compared with the one from

vehicle responses based on Chapter 3. A good agreement was found for different driving

cases, showing the robustness and the practicality of the algorithm.

Chapter 7 Conclusions and Future Work

7.1 Conclusions

This study proposed methods for bridge static weight estimation and moving dynamic load identification. The thesis is divided into two parts. The first part deals with bridge property estimation from vehicle responses, including bridge modal mass identification in Chapter 3 and bridge pavement roughness estimation in Chapter 4. The estimated bridge properties in these two chapters are used in the second part, which corresponds to bridge static moving load estimation in Chapter 5 and moving dynamic load identification in Chapter 6. The conclusions of each chapter are stated as follows.

In Chapter 3, a Kalman filter-based method to estimate vehicle dynamic tire force from simple measurement on vehicle body acceleration and angular velocity is proposed. Observability analysis shows that the combination of these responses is sufficient for tire force estimation while other response quantities of the vehicle may not be fully observable. Numerical examples show that this algorithm can achieve satisfactory accuracy even when sensor noise and modelling error exist. A field measurement shows that this method can estimate the tire force within the range of $1 - 5$ Hz, which is sufficient for most short-to-medium-span bridges. Genetic algorithm is then adopted for bridge modal mass identification using the estimated tire forces and simultaneously measured bridge acceleration responses.

In Chapter 4, the bridge pavement roughness is estimated from vehicle responses. In addition to vehicle body acceleration and angular velocity, the vehicle body displacement and angle responses are integrated and included in the observation vector due to the requirement of observability. The vehicle-bridge interaction is considered to compensate for the influence from bridge vibration induced by the test vehicle. Particle filter is used to deal with the nonlinearity caused by this vehicle-bridge coupling phenomenon. Numerical examples show the algorithm is robust against sensor noise, vehicle modelling error. The algorithm is also validated by a field measurement.

In Chapter 5, a method for vehicle parameter identification is proposed using the estimated bridge pavement roughness by particle filter. The passing vehicle is represented by a half-car model with unknown parameters, which are included in the state vector for identification purpose. Bridge acceleration responses are used as measurement data included in the observation vector. Numerical examples show that the inclusion of integrated bridge displacement response can increase the converging speed and accuracy toward the target value. Weighted global iteration is also found to be effective when the sensor noise is large. The vehicle parameters in the lower part are shown to be more sensitive to the bridge acceleration responses while those in the upper part are more sensitive to the bridge displacement responses. This result is supported by a sensitivity analysis.

In Chapter 6, moving dynamic load identification is addressed. The vehicle front and rear tire force terms are included in the state vector as well as a parameter indicating the vehicle passing lane. The vehicle moving tire force can be estimated together with the

vehicle passing lane parameter. The ratio of the vehicle wheelbase over the bridge length is found to have an influence on the capacity of distinguishing the front tire force and rear tire force. During experimental validation of this method, some insensitive areas are found at both ends of the bridge and at the middle support, where even large tire forces lead to small bridge responses.

7.2 Future Work

This study can be further improved by addressing the following points.

(1) The method to give vehicle mass and dynamic load information in this study is only suitable for the case where only one vehicle is on the bridge. Studies for multiple vehicle presence on the bridge need to be carried out in future research.

(2) The algorithm of bridge static and dynamic load identification is sensitive to the bridge modal mass. The estimation error is shown to be proportionally related with bridge modal mass errors. The robustness against bridge modal mass value needs to be further increased.

(3) In the vehicle parameter identification section, the bridge pavement roughness is used. However, it will become more beneficial if the process of bridge pavement roughness estimation process can be removed. The use of pavement roughness becomes a source of estimation error because the pavement changes over time and because the path pavement is estimated on may be different from the path of target vehicles. One possible solution is to use the bridge inclination data obtained from multi-channel accelerometers in the moving dynamic load estimation method and evaluate both the static and dynamic component of the force. The bridge inclination data, which provides low-frequency

information, can be included in the state vector to give bridge moving constant load. Combined with bridge acceleration measurement, the new method can give estimation on both static and dynamic moving load.

(4) Axle weight and dynamic load

In the current study, the vehicle weight and dynamic load are identified in the form of the summation of vehicle front and rear axle loads. While the summation of front and rear static and dynamic load is an important factor, sometimes the axle loads are preferred. However, it is difficult to distinguish one axle load from the other by using bridge global vibration. More studies can be conducted by focusing on the local vibration of the bridge to give axle load information.

Appendix A Performance Analysis of Wireless Accelerometers

A.1 Introduction

In this study, various types of sensors are used for the measurement either on the vehicle or on the bridge. The development of the algorithm proposed in each chapter is highly dependent on the performance of the sensors. The accuracy of the sensor measurement at the frequency range of interest need to be investigated in advance. This appendix aims at providing a proof of the reliability of the sensors adopted in this study.

Mainly, there are three types of sensors used in this study. They include (a) smartphone-based sensors, which are used for vehicle vibration measurement, (b) wireless accelerometers, which are developed based on Epson sensors (Epson Corporation, 2018) and are used for bridge vibration measurement and bridge property extraction, and (c) JAE accelerometers, for the synchronization of the vehicle and bridge measurement system.

The performance of the smartphone-based sensors has already been checked by previous research (Zhao, 2017). The JAE accelerometer is used only for the synchronization purpose. Therefore, only the wireless accelerometers are checked in this appendix, which is divided into two parts, the static test and the shake-table test, described in Section A.1 and Section A.2, respectively.

A.2 Static test

The static test was done by putting the wireless sensor on the ground of the basement of the wind tunnel of bridge laboratory in The University of Tokyo, without any input excitation, as shown in Fig. A-1. A CV-375 sensor (Tokyo Sokushin corporation, 2014), which is considered to have a high measurement accuracy and a low noise level, was placed next to the wireless sensors for the purpose of comparison.

(a) Wireless accelerometers in the static test   (b) CV-375 sensor

Fig. A-1. Wireless accelerometers in the static test

The static test was conducted to check the noise level of the sensors when there is no other input excitation. However, even when the condition is well-controlled, ambient vibration still exists due to many reasons, including ground micro-vibration, influence from vehicles in city area, small wind, etc. Although small vibration can still be observed, the amplitudes of this ambient vibration is limited to small values compared to the noise signal of each sensor, as can be seen in the z-axis (vertical) time history of the static test shown in Fig. A-2. Note that the ADXL sensors are installed inside the wireless sensor nodes.

Fig. A-2. Time history of the static test

In Fig. A-2, it is observed that the time history values of the wireless sensor are smaller than those of the CV sensor. This effect is due to the low-pass filter with a cutoff frequency of 10 Hz implemented on the Epson sensor node, making the signal level of the higher frequency range decrease, as observed in Fig. A-3.
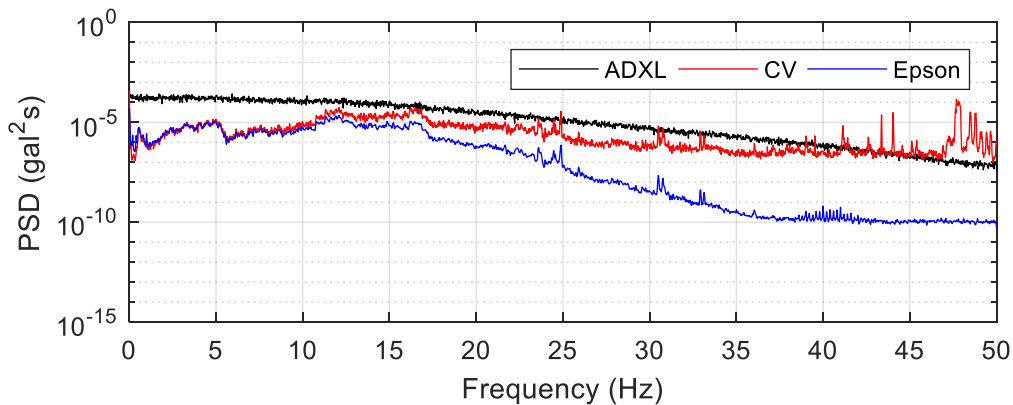
Fig. A-3. PSD in the range of 0 – 50 Hz

The frequency range of 1 – 7 Hz is zoomed in and is shown in Fig. A-4. The reason of choosing this frequency range is because most short-to-medium-span bridges have their natural frequencies in this range. The result shows that the signal in this frequency range

163

of interest is close to that of the CV sensor, indicating that the Epson-based wireless accelerometer has a satisfactory noise level.
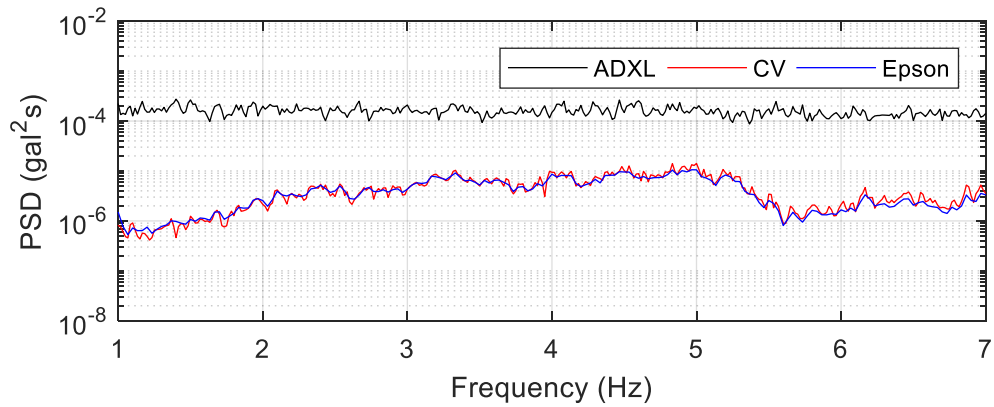
Fig. A-4. PSD in the range of 1 – 7 Hz

To check the performance of the sensors at low frequency range, the PSD in the frequency range of 0.02 – 0.2 Hz is also zoomed in and shown in Fig. A-5. It is observed that the signals of the Epson is higher than that of the CV, indicating the noise level is relatively higher.
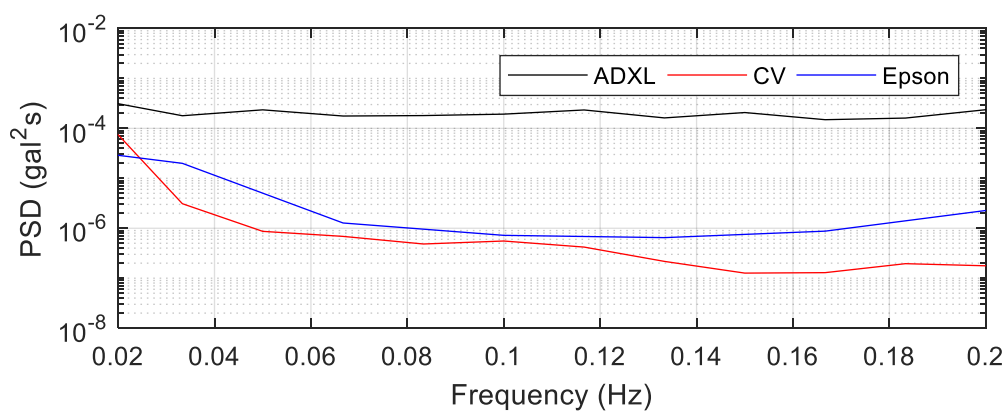
Fig. A-5. PSD in the range of 0.02 – 0.2 Hz

Another type of sensor, known as ADXL accelerometer shown in Fig. A-2 to Fig. A-5, is also compared in this static test. A much larger noise level is observed along the entire frequency axis.

A.3 Shake-table test

To investigate the accuracy of the acceleration signals recorded by the wireless sensors, a shake-table test was conducted. The CV sensor was used again as the reference. The sensor layout of the shake-table tests is shown in Fig. A-6. The smartphones attached on the CV sensor body were tested together with wireless sensors but they are irrelevant with this study.

Fig. A-6. Sensor layout of the shake-table test

The cases for the shake-table test include white-noise random wave excitation and sinusoidal excitation. The details of the cases are listed in Table A-1.

Table A-1. Cases of the shake-table test

Type of Excitation	Description
White-noise random wave	0 – 50 Hz
	1 – 2 Hz
	2 – 5 Hz
	5 – 10 Hz
Sinusoidal wave	5 Hz

For each case listed in Table A-1, the recorded signals are compared in the frequency domain in the range of 1 – 7 Hz, as shown in Fig. A-7.
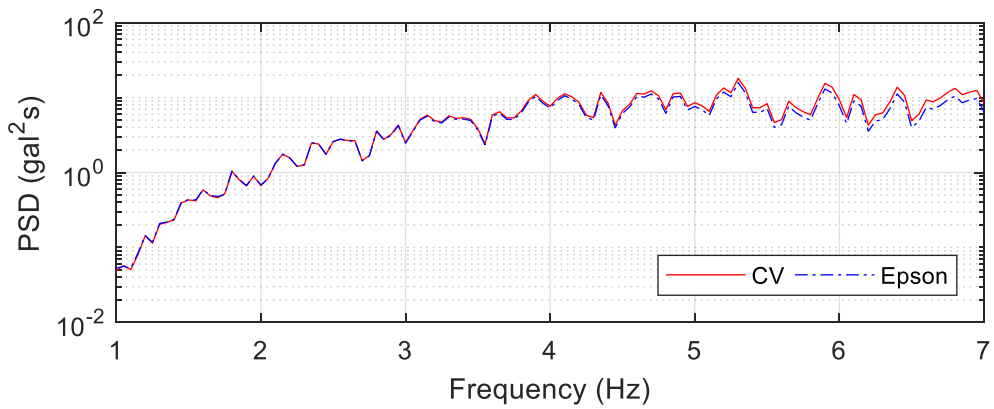
(a) Random 0 – 50 Hz
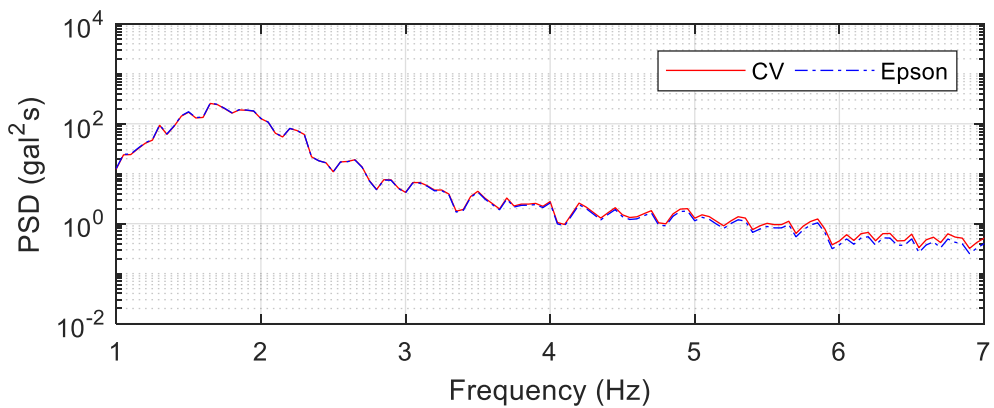
(b) Random 1 – 2 Hz
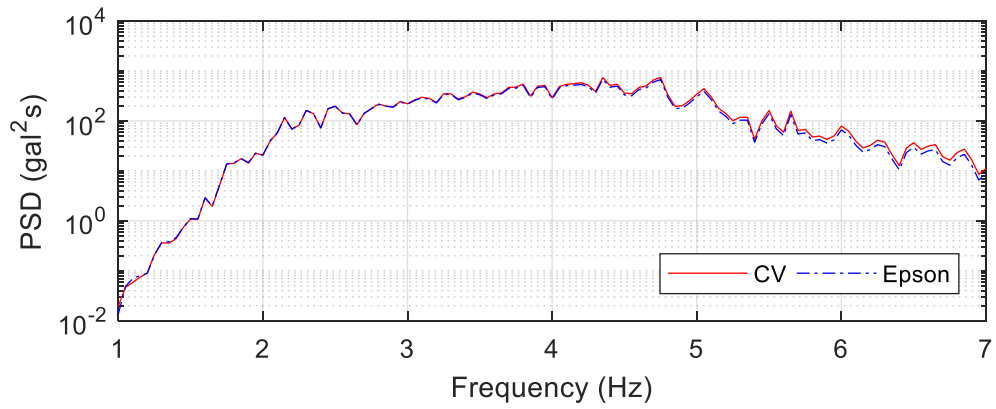
(c) Random 2 – 5 Hz
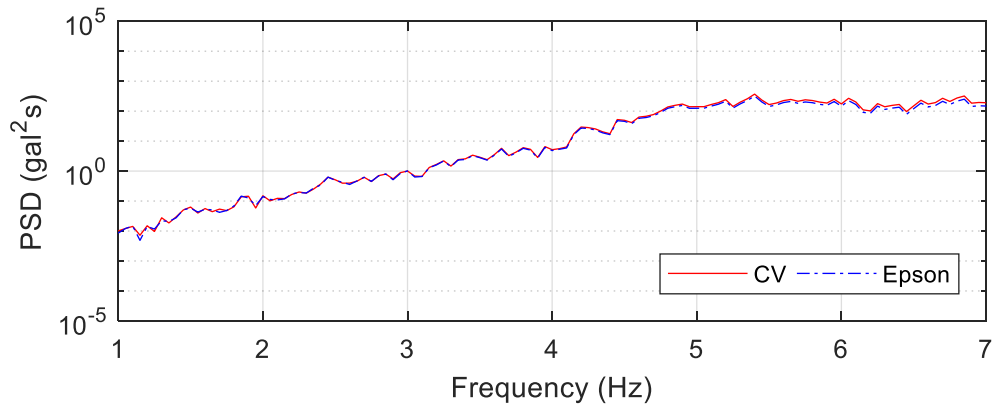
(d) Random 5 – 10 Hz
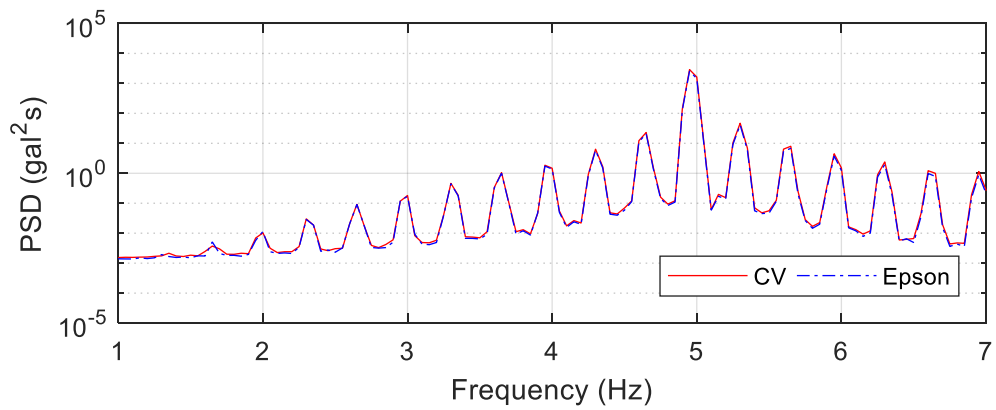
(e) Sine 5 Hz

Fig. A-7. Signal comparison for shake-table test

From the figures above, it is seen that the signals of the wireless accelerometer show good agreement of the signals of the CV sensor, indicating that the wireless sensor node has a good performance in the shake-table test and is proved to be reliable for the measurement conducted in this study. However, it should be noted that the analysis of wireless sensors in this appendix corresponds to z-axis because these sensors are used for measurement of the bridge vertical vibration.

Appendix B Bridge Fundamental Frequency Identification from Estimated Vehicle Excitation

B.1 Introduction

A bridge's natural frequencies are important dynamic properties reflecting the structural condition of the bridge. Numerous studies have been conducted in the field to extract a bridge's natural frequencies from responses of passing vehicles. The bridge frequency peaks are, however, not easily observed, because pavement roughness often influences the spectra of vehicle responses.

As an extension to Chapter 4, a method that extracts the fundamental frequency of a bridge from the responses of an ordinary vehicle with its parameters calibrated in advance is proposed. The method is based on the idea that the vehicle passing across a bridge is excited by two sources, i.e., pavement roughness and bridge vibration. The excitation inputs to the vehicle, i.e., displacement inputs at the front and rear tire locations, are estimated from vehicle responses using a particle filter method. The estimated displacement inputs at the front and rear tires are then subtracted from each other after shifting by a wheel–base distance to eliminate the roughness influence, which commonly appears in both signals. The signal after the subtraction contains only the bridge vibration influence and is used to extract the fundamental frequency of the bridge.

This indirect method of bridge frequency extraction is investigated through numerical simulations. A field measurement was also conducted, and it showed that the bridge's fundamental frequency was successfully extracted with a good accuracy for several driving-speed cases.

B.2 Extraction of bridge vibration components

As stated in Chapter 4, when a two-axle vehicle passing over a bridge, the total input excitation to the vehicle are expressed as the summation of the pavement roughness and the bridge deflection. This relation is described in Eq. (4-1) and is repeated here for the readers' convenience.

$$
\begin{aligned}
h_f(t) &= r_f(t) + y_f(t) \\
h_r(t) &= r_r(t) + y_r(t)
\end{aligned}
\tag{B-1}
$$

where the pavement roughness at the front and rear tires is defined as $r_f(t)$ and $r_r(t)$, respectively and the bridge deflection under each tire is $y_f(t)$ and $y_r(t)$.

Assuming the front tire and rear tire pass on the same path, the excitation input displacement components due to the pavement roughness at the front and rear tires are common if one signal is shifted by the wheel–base distance (Kong et al, 2016, Kong et al, 2017). The excitation input displacement at the rear tire is subtracted from the input displacement at the front tire, and the pavement roughness components are canceled out as

$$
\begin{aligned}
D(t) &= h_f(t) - h_r(t + \tau) \\
&= r_f(t) + y_f(t) - r_r(t + \tau) - y_r(t + \tau) \\
&= y_f(t) - y_r(t + \tau)
\end{aligned}
\tag{B-2}
$$

where τ is the time needed for the vehicle to travel a wheel–base distance and $D(t)$ is the

remaining bridge vibration components, from which the dominant frequency can be extracted through Fourier analysis.

Note that this extracted frequency is the dominant frequency of the vehicle–bridge coupled system. According to (Cantero et al, 2017), when a vehicle is passing across the bridge, the vehicle–bridge coupled frequency is affected. This effect is more severe if the mass of the passing vehicle becomes larger. However, because the vehicle used in this study is an ordinary vehicle, the difference between the dominant frequency and the bridge fundamental frequency is smaller than the difference typically observed in heavy tractor-and-trailer system cases.

B.3 Inadequate speeds

The theoretical foundation of the proposed method is that the subtracted signal $D(t)$ from Eq. (B-2) contains the bridge frequency components. However, this foundation is not always guaranteed. There are two conditions in which the bridge frequency component may disappear. The first condition is that, when τ is a multiple of the vibration period corresponding to the bridge fundamental frequency, the bridge vibration component at this frequency is canceled out through the subtraction in Eq. (B-2). This situation is described as

$$\tau = \frac{d_w}{v} = k \cdot \frac{1}{f_n}, (k = 1, 2, 3 \cdots)$$ (B-3)

where d_w is wheel–base distance, v is vehicle speed, and f_n is the bridge fundamental frequency.

This equation is rewritten as

$$v = \frac{d_w f_n}{k} \tag{B-4}$$

For the given values of f_n and d_w, if the vehicle is driven at the speed in Eq. (B-4), the bridge vibration component at the fundamental frequency is canceled out through the subtraction in Eq. (B-2). Thus, the method proposed in Section B.2 cannot give bridge fundamental frequency estimation. This speed is defined as "inadequate speed."

Another type of inadequate speed is explained below. Because the proposed method is based on the spectrum of bridge vibration, the bridge's fundamental frequency can be estimated only when the bridge vibration, i.e., $y(x,t)$ in Eq. (B-1), is fully excited at the fundamental frequency. However, because the bridge is excited by the front-tire force and the rear-tire force simultaneously, if the frequency component of F_f and F_r at the bridge's fundamental frequency are in opposite phases, this component is minimized in the total input F_b on the bridge. The condition is given below:

$$\tau = \frac{d_w}{v} = \frac{2k-1}{2} \cdot \frac{1}{f_n}, (k = 1, 2, 3 \cdots) \tag{B-5}$$

which leads to

$$v = \frac{2d_w f_n}{2k-1} \tag{B-6}$$

This is the inadequate speed of excitation. Note that this type of inadequate speed also requires that the forces at the front and rear tires, i.e., F_f and F_r, are close to each other. However, from Eq. (2-25), this requires the parameters of the vehicle front part be close to those of the rear part, which is not always the case for normal vehicles (Jazar, 2008).

B.4 Numerical verification

A simple numerical example is conducted to verify the proposed algorithm. In this numerical example, the vehicle model, bridge model, and the bridge pavement roughness used in Section 4.3 is adopted. The implementation of particle filter is also similar with Section 4, while the only difference is that the vehicle-bridge interaction is not considered here. The roughness estimation result from the front tire and the rear tire as well as their subtraction after shifting are shown in Fig. B-1.
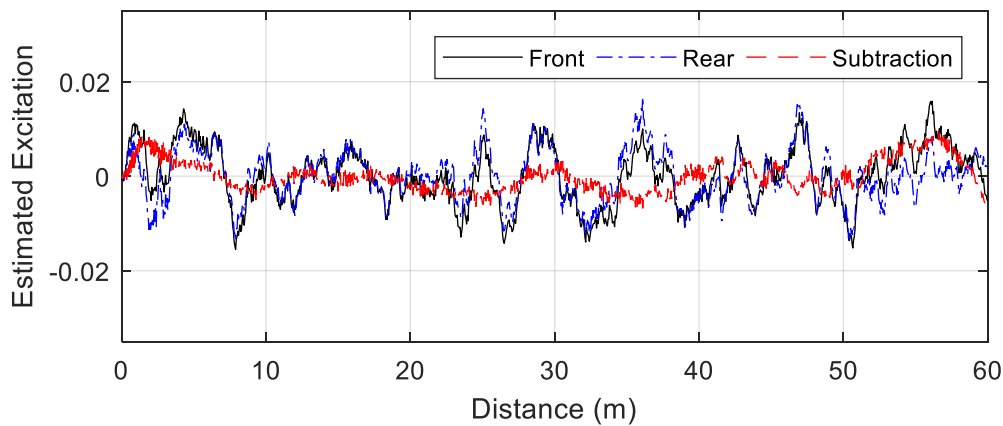
Fig. B-1. The comparison of the estimation results of the front and rear tires

The PSD of the subtracted signal in Fig. B-1 is calculated and shown in Fig. B-2. A clear peak appears at 1.95 Hz, representing the first bridge fundamental frequency with an error of 3.17%, whereas the true value is 1.89 Hz. The PSD of the estimated excitation input at the front tire without the subtraction procedure is also shown for comparison. This PSD is significantly influenced by the components of the pavement roughness, especially in the low-frequency range, making it hard to distinguish the bridge's fundamental frequency. The PSD before subtraction has higher amplitudes at all frequency components due to the roughness input. After subtraction, the main components are

canceled out except for those of bridge vibration, giving much smaller signal amplitudes. Therefore, this PSD is factored by 1/2 to make it comparable in Fig. B-2. Large amplitudes are observed at the low-frequency range below 1 Hz, which can be explained by the limited accuracy of the profile estimation in this frequency range, potentially due to small signal-to-noise ratio and vehicle modeling error.
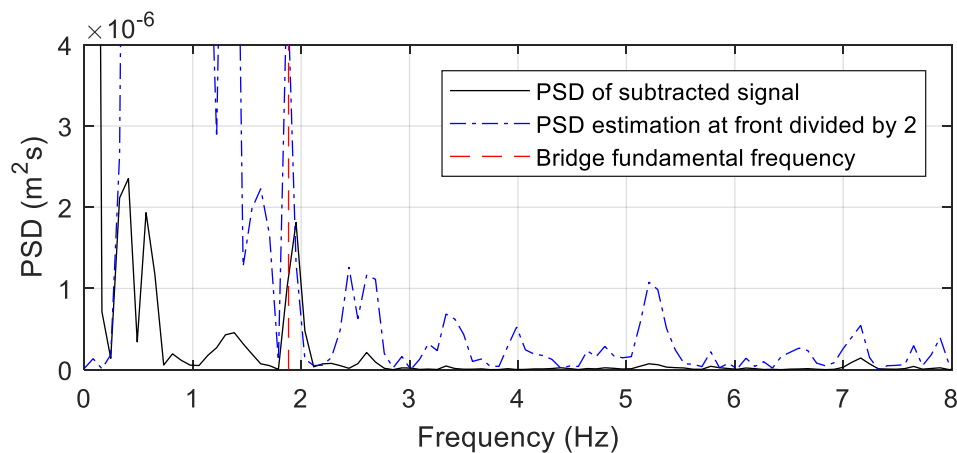
Fig. B-2. Spectrum of the subtracted signal

B.5 Experimental validation

The experimental validation was analyzed using the measurement data in Tsukige Bridge described in Section 4. The sensor-equipped test vehicle was driven to pass over the bridge. Four driving speeds were adopted, including 20, 25, 30, and 35 km/h, to test the speed dependency of the proposed method. The reason for not trying higher-speed cases is that higher speeds give shorter passing time, which leads to low resolution in frequency analysis. For each speed case, six tests were conducted. Although the vehicle was supposed to pass at a constant speed, some fluctuations about the driving speed were observed. The actual speed range is shown in Table B-1. Note that the inadequate speed for the chosen vehicle and bridge was 19.44 km/h, which is close to one of the testing

speeds, i.e., 20 km/h.

Table B-1. Actual speed range of each case (km/h)

Target Speed	20	25	30	35
Actual Range	15.3 – 20.5	21.2 – 23.4	24.8 – 29.8	28.9 – 34.3

The excitation input displacements at the front and rear tires are estimated using the particle filter method. Fig. 13 shows a typical estimation result at a speed of 20 km/h. The front and rear tire estimations coincided well after a constant distance shift. Results of other tests and speed cases were similar to this case. The difference between the front and rear tire estimations was partly explained by the existence of noise, including sensor noise and vehicle modeling error. More importantly, the excitation input displacements at the front and rear tires were different from each other because the bridge vibration components were different for the front and rear tires.
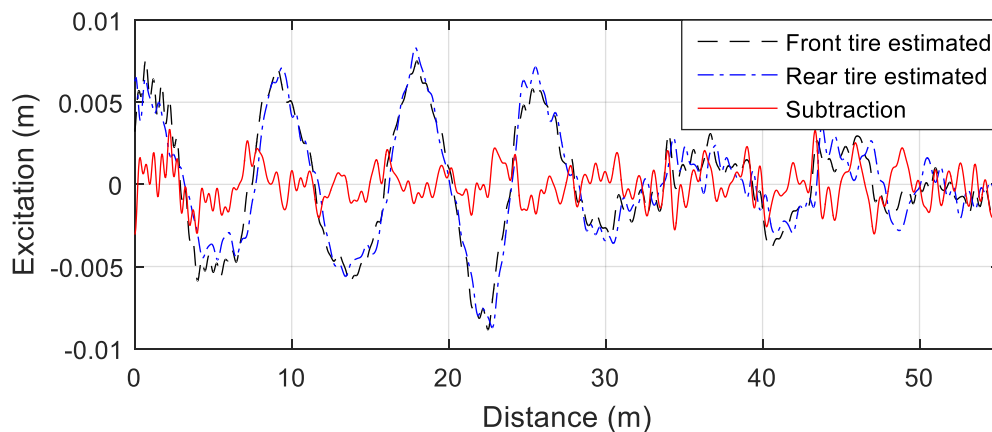
Fig. B-3. Comparison of front and rear tire estimated inputs

The PSD of the subtracted signal in Fig. B-3 is shown in Fig. B-4. Although a peak is

found around the bridge fundamental frequency, the frequency resolution is low due to limited length of the signal, leading to an inaccuracy of the result. Therefore, the estimated results of all tests for one speed case are connected together to form a longer time history. The subtracted input displacements are connected in spatial domain after being converted from time domain using GPS speed data. The PSD of the connected signal is then calculated. The results for all the four speed cases are shown in Fig. B-5 (a) – (d)
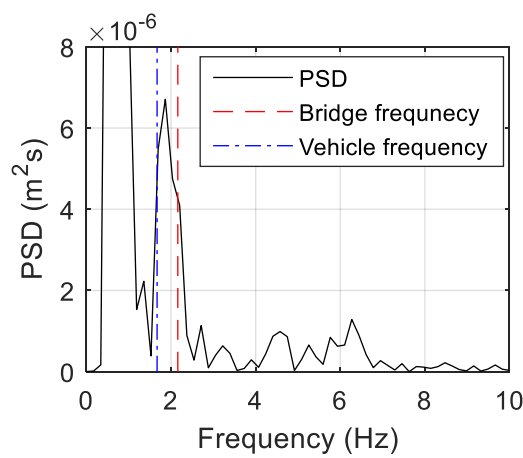
Fig. B-4. PSD of one subtracted signal
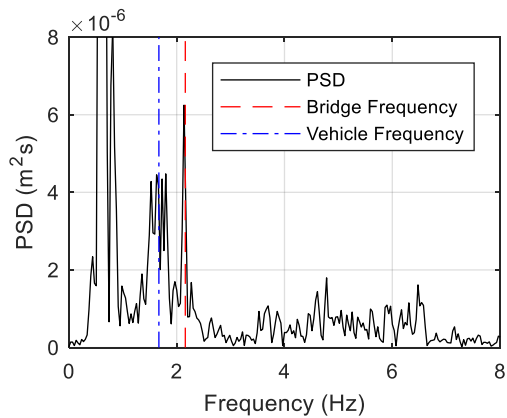
(a) 20 km/h
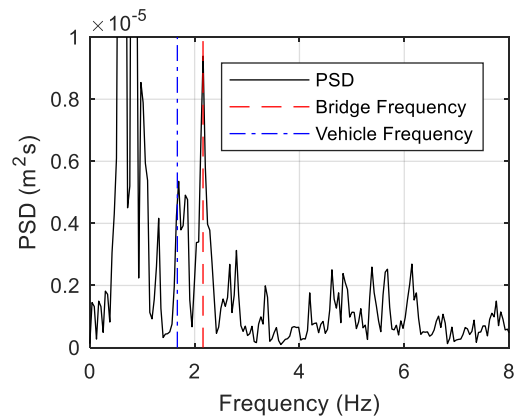
(b) 25 km/h
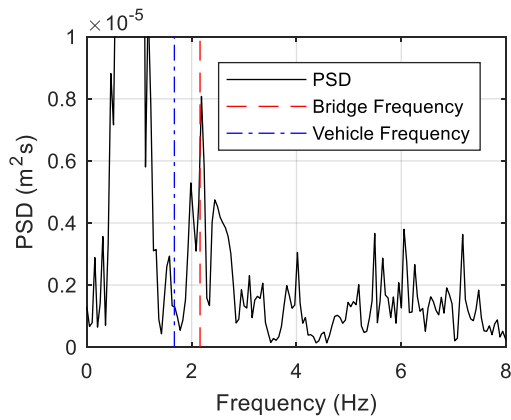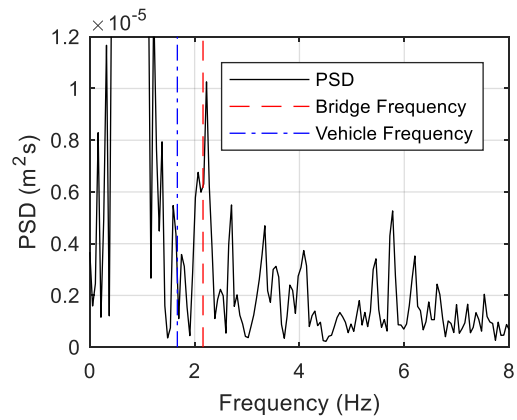
(c) 30 km/h   (d) 35 km/h

Fig. B-5. Bridge fundamental frequency estimation result for all speed cases

As shown in Fig. B-5, peaks around bridge fundamental frequency at 2.16 Hz are clearly observed. The estimation results and errors are listed in Table B-2. Small peaks are also observed around the vehicle frequency, and the PSD amplitudes are higher at the low-frequency range around 1 Hz. This indicates that the influences from the pavement roughness and vehicle responses are still not fully eliminated due to various errors and noises. However, the peak of bridge fundamental frequency is clear and larger than other noise peaks at possible frequency range.

Table B-2. Estimation value and estimation error for all speed cases

	20 km/h	25 km/h	30 km/h	35 km/h
Estimation Value	2.13 Hz	2.17 Hz	2.19 Hz	2.23 Hz
Estimation Error	1.4 %	0.5 %	1.4 %	3.2 %

The results prove that the proposed method is practical for frequency extraction for real bridges. It is worth noting that, even in the inadequate speed case of 20 km/h, a bridge fundamental frequency peak also appears clearly in the spectrum, which is inconsistent with the simulation results in Section 5. This is because, when the vehicle is passing over the bridge, the driving speed fluctuates around 20 km/h, making the speed not always inadequate. Thus, the bridge's fundamental frequency component is not completely canceled out, giving a clear peak in the spectrum.

References

Agostinacchio, M., D. Ciampa, and S. Olita. "The vibrations induced by surface irregularities in road pavements–a Matlab® approach." *European Transport Research Review* 6.3 (2014): 267-275.

Arulampalam, M. Sanjeev, et al. "A tutorial on particle filters for online nonlinear/non-Gaussian Bayesian tracking." *IEEE Transactions on signal processing* 50.2 (2002): 174-188.

Au, F. T. K., R. J. Jiang, and Y. K. Cheung. "Parameter identification of vehicles moving on continuous bridges." *Journal of sound and vibration* 269.1-2 (2004): 91-111.

Bang, Hyochoong, and Young W. Kwon. *The finite element method using MATLAB*. CRC press, 2000.

Biezma, María Victoria, and Frank Schanack. "Collapse of steel bridges." *Journal of Performance of Constructed Facilities* 21.5 (2007): 398-405.

Blejwas, T. E., C. C. Feng, and R. S. Ayre. "Dynamic interaction of moving vehicles and structures." *Journal of Sound and Vibration* 67.4 (1979): 513-521.

Braghin, Francesco, et al. "Measurement of contact forces and patch features by means of accelerometers fixed inside the tire to improve future car active control." *Vehicle System Dynamics* 44.sup1 (2006): 3-13.

Brownjohn, J. M. W., and A. Pavic. "Experimental methods for estimating modal mass in footbridges using human-induced dynamic excitation." *Engineering Structures* 29.11 (2007): 2833-2843.

Brownjohn, James Mark William, et al. "Footbridge system identification using wireless inertial measurement units for force and response measurements." *Journal of Sound and Vibration*384 (2016): 339-355.

Bu, J. Q., S. S. Law, and X. Q. Zhu. "Innovative bridge condition assessment from dynamic response of a passing vehicle." *Journal of engineering mechanics* 132.12 (2006): 1372-1379.

Cantero, Daniel, David Hester, and James Brownjohn. "Evolution of bridge frequencies and modes of vibration during truck passage." *Engineering Structures* 152 (2017): 452-464.

Carpenter, James, Peter Clifford, and Paul Fearnhead. "Improved particle filter for nonlinear problems." *IEE Proceedings-Radar, Sonar and Navigation* 146.1 (1999): 2-7.

Cebon, D. "Theoretical road damage due to dynamic tyre forces of heavy vehicles Part 2: simulated damage caused by a tandem-axle vehicle." *Proceedings of the Institution of Mechanical Engineers, Part C: Journal of Mechanical Engineering Science* 202.2 (1988): 109-117.

Chan, Tommy HT. "A MOM-based algorithm for moving force identification: Part|–Theory and numerical simulation." *Structural Engineering and Mechanics* 29.2 (2008): 135-154.

Chan, Tommy HT, et al. "An interpretive method for moving force identification." *Journal of sound and vibration* 219.3 (1999): 503-524.

Chatzis, Manolis N., Eleni N. Chatzi, and Andrew W. Smyth. "On the observability and identifiability of nonlinear structural and mechanical systems." *Structural Control and Health Monitoring*22.3 (2015): 574-593.

Cheli, F., et al. "Design and testing of an innovative measurement device for tyre–road contact forces." *Mechanical systems and signal processing* 25.6 (2011): 1956-1972.

Chen, Tsung-Chien, and Ming-Hui Lee. "Research on moving force estimation of the bridge structure using the adaptive input estimation method." *Journal of Structural Engineering* 8 (2008): 20-208.

Chen, Qiang, et al. "Inertia force identification of cantilever under moving-mass by inverse method." *Indonesian Journal of Electrical Engineering and Computer Science* 10.8 (2012): 2108-2116.

Chen, Zhao, Zhipeng Xie, and Jian Zhang. "Measurement of Vehicle-Bridge-Interaction force using dynamic tire pressure monitoring." *Mechanical Systems and Signal*

Processing 104 (2018): 370-383.

Chopra, Anil K. "Dynamics of Structures. Theory and Applications to." *Earthquake Engineering* (2017).

Cordeiro, Rafael A., et al. "Tire-ground forces estimation in a 4-wheel vehicle using a delayed interconnected cascade-observer structure." *IFAC-PapersOnLine* 49.15 (2016): 139-144.

COST 323. "Weigh‑in‑Motion of Road Vehicles." *Final report of the COST 323 Action (WIM-LOAD), Laboratoire Central des Ponts et Chaussées, Paris* (2002).

Dakhlallah, Jamil, et al. "Tire-road forces estimation using extended Kalman filter and sideslip angle evaluation." *American Control Conference, 2008*. IEEE, 2008.

Davis, Lawrence. "Handbook of genetic algorithms." (1991).

Dempsey, A. T., B. Jacob, and J. Carracilli. "Orthotropic bridge weigh-in-motion for determining axle and gross vehicle weights." *SECOND EUROPEAN CONFERENCE ON WEIGH-IN-MOTION OF ROAD VEHICLES, HELD LISBON, PORTUGAL 14-16 SEPTEMBER 1998*. 1998.

Deng, Lu, and C. S. Cai. "Identification of parameters of vehicles moving on bridges." *Engineering Structures* 31.10 (2009): 2474-2485.

Doumiati, Moustapha, et al. "Observers for vehicle tyre/road forces estimation: experimental validation." *Vehicle System Dynamics* 48.11 (2010): 1345-1378.

Doumiati, Moustapha, et al. *Vehicle Dynamics Estimation using Kalman Filtering: Experimental Validation*. John Wiley & Sons, 2012.

Epson,   https://www.epson.jp/prod/sensing_system/pdf/m-a351_briefsheet_j_rev20180309.pdf

Fu, Gongkang, and Osman Hag-Elsafi. "Vehicular overloads: Load model, bridge safety, and permit checking." *Journal of Bridge Engineering* 5.1 (2000): 49-57.

Fujino, Yozo, and Dionsius Manly Siringoringo. "Bridge monitoring in Japan: the needs and strategies." *Structure and Infrastructure Engineering* 7.7-8 (2011): 597-611.

Garg, V. K., and R. V. Dukkipati. "Dynamics of Railway Vehicle Systems. Academic Press, New York, 1984."

Gomez, Hugo C., et al. "Testing and long-term monitoring of a curved concrete box girder bridge." *Engineering Structures*33.10 (2011): 2861-2869.

González, Arturo, C. Rowley, and Eugene J. OBrien. "A general solution to the identification of moving vehicle forces on a bridge." *International journal for numerical methods in engineering* 75.3 (2008): 335-354.

Gordon, Neil J., David J. Salmond, and Adrian FM Smith. "Novel approach to nonlinear/non-Gaussian Bayesian state estimation." *IEE Proceedings F (Radar and Signal Processing)*. Vol. 140. No. 2. IET Digital Library, 1993.

Green, M. F., and D. Cebon. "Dynamic interaction between heavy vehicles and highway bridges." *Computers & structures*62.2 (1997): 253-264.

Hamann, Harry, et al. "Tire force estimation for a passenger vehicle with the unscented kalman filter." *Intelligent Vehicles Symposium Proceedings, 2014 IEEE*. IEEE, 2014.

Hermann, Robert, and Arthur Krener. "Nonlinear controllability and observability." *IEEE Transactions on automatic control* 22.5 (1977): 728-740.

Honda Corporation, https://www.honda.co.jp/STEPWGN

Hoshiya, Masaru, and Osamu Maruyama. "Identification of running load and beam system." *Journal of engineering mechanics* 113.6 (1987): 813-824.

ISO, 8608. "Mechanical vibration—Road surface profiles—Reporting of measured data." *ISO 8608: 1995* (1995).

Jacob, Bernard, and Véronique Feypell-de La Beaumelle. "Improving truck safety: Potential of weigh-in-motion technology." *IATSS research* 34.1 (2010): 9-15.

JAE Corporation, https://www.jae.com/en/index.html

Jazar, Reza N. *Vehicle dynamics: theory and application*. Springer, 2017.

Jiang, Kun, et al. "Estimation of vehicle's vertical and lateral tire forces considering road angle and road irregularity." *17th International IEEE Conference on Intelligent Transportation Systems (ITSC 2014)*. IEEE, 2014.

Jiang, R. J., F. T. K. Au, and Y. K. Cheung. "Identification of vehicles moving on continuous bridges with rough surface." *Journal of Sound and Vibration* 274.3-5 (2004): 1045-1063.

Kalman, Rudolph Emil. "A new approach to linear filtering and prediction problems." *Journal of basic Engineering* 82.1 (1960): 35-45.

Kim, Sungkon, et al. "Vehicle signal analysis using artificial neural networks for a bridge weigh-in-motion system." *Sensors*9.10 (2009): 7943-7956.
Suntop Techno Corporation, http://www.suntop.jp/DAM.html

Kong, Xuan, et al. "Using dynamic responses of moving vehicles to extract bridge modal properties of a field bridge." *Journal of Bridge Engineering* 22.6 (2017): 04017018.

Kong, X., C. S. Cai, and B. Kong. "Numerically extracting bridge modal properties from dynamic responses of moving vehicles." *Journal of Engineering Mechanics* 142.6

(2016): 04016025.

Lalthlamuana R. "Identification of vehicle parameters from bridge dynamic response." PhD Thesis, Indian Institute of Technology Guwahati (2015)

Law, S. S., et al. "Vehicle axle loads identification using finite element method." *Engineering Structures* 26.8 (2004): 1143-1153.

Law, S. S., et al. "Vehicle condition surveillance on continuous bridges based on response sensitivity." *Journal of engineering mechanics* 132.1 (2006): 78-86.

Law, S. S., Tommy HT Chan, and Q. H. Zeng. "Moving force identification—a frequency and time domains analysis." *Journal of dynamic systems, measurement, and control* 121.3 (1999): 394-401.

Law, S. S., and Y. L. Fang. "Moving force identification: optimal state estimation approach." *Journal of Sound and Vibration* 239.2 (2001): 233-254.

Law, Siu-Seong, and Xin-Qun Zhu. *Moving Loads–Dynamic Analysis and Identification Techniques: Structures and Infrastructures Book Series*. Vol. 8. CRC Press, 2011.

Lin, C. W., and Y. B. Yang. "Use of a passing vehicle to scan the fundamental bridge frequencies: An experimental verification." *Engineering Structures* 27.13 (2005): 1865-1878.

Liu, K., et al. "A comparison of different solution algorithms for the numerical analysis of vehicle–bridge interaction." *International Journal of Structural Stability and Dynamics* 14.02 (2014): 1350065.

Lu, Z. R., and S. S. Law. "Features of dynamic response sensitivity and its application in damage detection." *Journal of sound and vibration* 303.1-2 (2007): 305-329.

Makihata, N., et al. "Large-scale road surface evaluation using dynamic responses of commercial vehicles." *ICE Virtual Library essential engineering knowledge* (2016).

McGetrick, Patrick J., A. Gonzlez, and Eugene J. OBrien. "Theoretical investigation of the use of a moving vehicle to identify bridge dynamic parameters." *Insight-Non-Destructive Testing and Condition Monitoring* 51.8 (2009): 433-438.

Moses, Fred. "Weigh-in-motion system using instrumented bridges." *Journal of Transportation Engineering* 105.3 (1979).

Nagayama, Tomonori, et al. "Middleware services for structural health monitoring using smart sensors." *Smart Structures and Systems* 5.2 (2009): 119-137.

Nagayama, T., et al. "Bridge natural frequency estimation by extracting the common vibration component from the responses of two vehicles." *Engineering Structures* 150 (2017): 821-829.

Nakano, Shinya, Genta Ueno, and Tomoyuki Higuchi. "Merging particle filter for sequential data assimilation." *Nonlinear Processes in Geophysics* 14.4 (2007): 395-408.

Nguyen, Khoa Viet, and Hai Thanh Tran. "Multi-cracks detection of a beam-like structure based on the on-vehicle vibration signal and wavelet analysis." *Journal of Sound and Vibration* 329.21 (2010): 4455-4465.

Nichireki Corporation,

https://www.nichireki.co.jp/product/consult/consult_list05/consult05_04.html

Nordström, Lars JL. "A dynamic programming algorithm for input estimation on linear time-variant systems." *Computer methods in applied mechanics and engineering* 195.44-47 (2006): 6407-6427.

O'Brien, Eugene J., et al. *Weighing-In-Motion of Axles and Vehicles for Europe (WAVE) WP1. 2: Bridge WIM Systems*. University College Dublin, 2001.

Ojio, T., and K. Yamada. "Bridge weigh-in-motion systems using stringers of plate girder bridges." *Third International Conference on Weigh-in-Motion (ICWIM3) Iowa State University, Ames*. 2002.

Ojio, T., and K. Yamada. "Bridge WIM by reaction force method." *International Conference on Weigh-In-Motion, 4th, 2005, Taipei, Taiwan*. 2005.

Ouyang, Huajiang. "Moving-load dynamic problems: a tutorial (with a brief overview)." *Mechanical Systems and Signal Processing* 25.6 (2011): 2039-2060.

Pan, Chu Dong, and Ling Yu. "Moving force identification based on firefly algorithm." *Advanced Materials Research*. Vol. 919. Trans Tech Publications, 2014.

Peters, R. J. "AXWAY-a system to obtain vehicle axle weights." *Australian Road Research* 12.1 (1984).

Peters, R. J. "CULWAY, an unmanned and undetectable highway speed vehicle weighing system." *Australian Road Research Board Proceedings*. 1986.

Quilligan, Michael. *Bridge weigh-in motion: Development of a 2-D multi-vehicle algorithm*. Diss. Byggvetenskap, 2003.

Rex Corporation, https://www.rex-inc.co.jp/index.html

Reynders, Edwin, et al. "Combined experimental-operational modal testing of footbridges." *Journal of Engineering Mechanics*136.6 (2010): 687-696.

Richardson, Jim, et al. "On the use of bridge weigh-in-motion for overweight truck enforcement." *International Journal of Heavy Vehicle Systems* 21.2 (2014): 83-104.

Sekiya, Hidehiko, et al. "Portable-Weigh Based on Displacement Measurement Using

Mems Accelerometer (Japanese Title: MEMS 加速度センサを用いた変位計測に基づく Portable-Weigh-In-Motion システムの提案)." *Journal of Japan Society of Civil Engineers, Ser. A1 (Structural Engineering & Earthquake Engineering (SE/EE))* 72 (2016): 364-379.

Shim, Taehyun, and Chinar Ghike. "Understanding the limitations of different vehicle models for roll dynamics studies." *Vehicle system dynamics* 45.3 (2007): 191-216.

Sonas Corporation, https://www.sonas.co.jp/

Tokyo Sokki Kenkyujo, http://www.tml.jp/product/automotive_ins/catalog_pdf/SLW-NC_MFT.pdf

Tokyo Sokushin Corporation. "Configuration of CV-375 sensor." http://www.to-soku.co.jp/products/recorder/pdf/cv375.pdf

Toyota Corporation, https://toyota.jp/hiacevan/

Tuononen, Ari. "On-board estimation of dynamic tyre forces from optically measured tyre carcass deflections." *International journal of heavy vehicle systems* 16.3 (2009): 362-378.

Wardhana, Kumalasari, and Fabian C. Hadipriono. "Analysis of recent bridge failures in

the United States." *Journal of performance of constructed facilities* 17.3 (2003): 144-150.

Wu, Shao-qing, and Zhi-yu Shi. "Identification of vehicle axle loads based on FEM-wavelet-Galerkin method." *Journal of Vibration Engineering* 4 (2006): 010.

Xiang, Zhihai, et al. "The tap-scan method for damage detection of bridge structures." *Interaction and multiscale mechanics* 3.2 (2010): 173-191.

Yang, Yeong-Bin, and Bing-Houng Lin. "Vehicle-bridge interaction analysis by dynamic condensation method." *Journal of Structural Engineering* 121.11 (1995): 1636-1643.

Yang, Yeong-Bin, et al. *Vehicle-bridge interaction dynamics: with applications to high-speed railways*. World Scientific, 2004.

Yang, Y. B., and K. C. Chang. "Extracting the bridge frequencies indirectly from a passing vehicle: Parametric study." *Engineering Structures* 31.10 (2009a): 2448-2459.

Yang, Y. B., and K. C. Chang. "Extraction of bridge frequencies from the dynamic response of a passing vehicle enhanced by the EMD technique." *Journal of sound and vibration* 322.4-5 (2009b): 718-739.

Yin, Shih-Hsun, and Chung-Yu Tang. "Identifying cable tension loss and deck damage in a cable-stayed bridge using a moving vehicle." *Journal of Vibration and Acoustics* 133.2 (2011): 021007.

Yu, Ling, and Tommy HT Chan. "Moving force identification based on the frequency–time domain method." *Journal of Sound and Vibration* 261.2 (2003): 329-349.

Yu, Ling, Tommy HT Chan, and Jun-Hua Zhu. "A MOM-based algorithm for moving force identification: Part II-Experiment and comparative studies." *Structural Engineering and Mechanics*29.2 (2008): 155-169.

Yu, Yang, C. S. Cai, and Lu Deng. "State-of-the-art review on bridge weigh-in-motion technology." *Advances in Structural Engineering* 19.9 (2016): 1514-1530.

Zhao Boyu. "Road roughness evaluation based on the identification of vehicle rigid body motion models and inverse analysis of vehicle responses. " PhD Thesis, The University of Tokyo (2017)

Zhao, B., S. Takada, and T. Nagayama. "Development of response-based road profile estimation using multiple observables." *JSCE Annual Meeting at Okayama*. 2015b.

Zhao, Boyu, and Tomonori Nagayama. "IRI Estimation by the frequency domain analysis of vehicle dynamic responses." *Procedia Engineering* 188 (2017): 9-16.

Zhao, Hua, et al. "Field-calibrated influence lines for improved axle weight identification with a bridge weigh-in-motion system." *Structure And Infrastructure Engineering* 11.6 (2015): 721-743.

Zhu, X. Q., and S. S. Law. "Moving forces identification on a multi-span continuous bridge." *Journal of sound and vibration*228.2 (1999): 377-396.

Zhu, X. Q., and S. S. Law. "Orthogonal function in moving loads identification on a multi-span bridge." *Journal of Sound and Vibration* 245.2 (2001): 329-345.

Zhu, X. Q., and Siu-Seong Law. "Recent developments in inverse problems of vehicle–bridge interaction dynamics." *Journal of Civil Structural Health Monitoring* 6.1 (2016): 107-128.

Zhu, X. Q., S. S. Law, and J. Q. Bu. "A state space formulation for moving loads identification." *Journal of vibration and acoustics* 128.4 (2006): 509-520.

Žnidarič, A., et al. "SiWIM bridge weigh-in-motion manual." (2011).

List of Publications Related to PhD Thesis

Journal Papers

[1] Wang, H., Nagayama, T., Zhao, B., Su, D. (2017). Identification of moving vehicle parameters using bridge responses and estimated bridge pavement roughness. **Engineering Structures, 153, 57-70.**

[2] Wang, H., Nagayama, T., Nakasuka, J., Zhao, B., Su, D. (2018). Extraction of bridge fundamental frequency from estimated vehicle excitation through a particle filter approach. **Journal of Sound and Vibration, 428, 44-58.**

[3] Wang, H., Nagayama, T., Su, D. (2018). Estimation of dynamic tire force through the measurement of vehicle body responses with numerical and experimental validation. **Mechanical Systems and Signal Processing. (Under review)**

International Conference papers

[1] Wang, H., Nagayama, T., Su, D. (2016). Vehicle parameter identification through particle filter using bridge responses and estimated profile. **The 6th Asia Pacific Workshop on Structural Health Monitoring, Hobart, Australia.**

[2] Wang, H., Nagayama, T., Su, D. (2017). A bridge weigh-in-motion method by moving force identification using augmented particle filter from measured bridge acceleration and inclination data. **The 13th International Workshop on Advanced Materials and Smart Structures Technology, Tokyo, Japan.**

[3] Wang, H., Nagayama, T., Su, D. (2018). Numerical study on vehicle force estimation from simple measurement on vehicle body responses. **The 7th World Conference on Structural Control and Monitoring, Qingdao, China.**

JSCE Annual Meeting Papers

[1] Wang, H., Nagayama, T., Su, D. (2016). Identification of vehicle parameters from acceleration data by using particle Filter. **The 71th JSCE Annual Meeting, Sendai, Japan.**

[2] Wang, H., Nagayama, T., Su, D. (2017). Experimental validation of vehicle identification from bridge responses by using particle filter. **The 72th JSCE Annual Meeting, Fukuoka, Japan.**

[3] Wang, H., Nagayama, T., Su, D. (2018). The force estimation through measurement of vehicle body acceleration and angular velocity. **The 73th JSCE Annual Meeting, Sapporo, Japan.**

[4] Wang, H., Nagayama, T., Su, D. (2018). Numerical study on vehicle static and dynamic load identification with lane detection from bridge acceleration and inclination data using particle filter method. **The 73th JSCE Annual Meeting, Sapporo, Japan.**